RCA Review

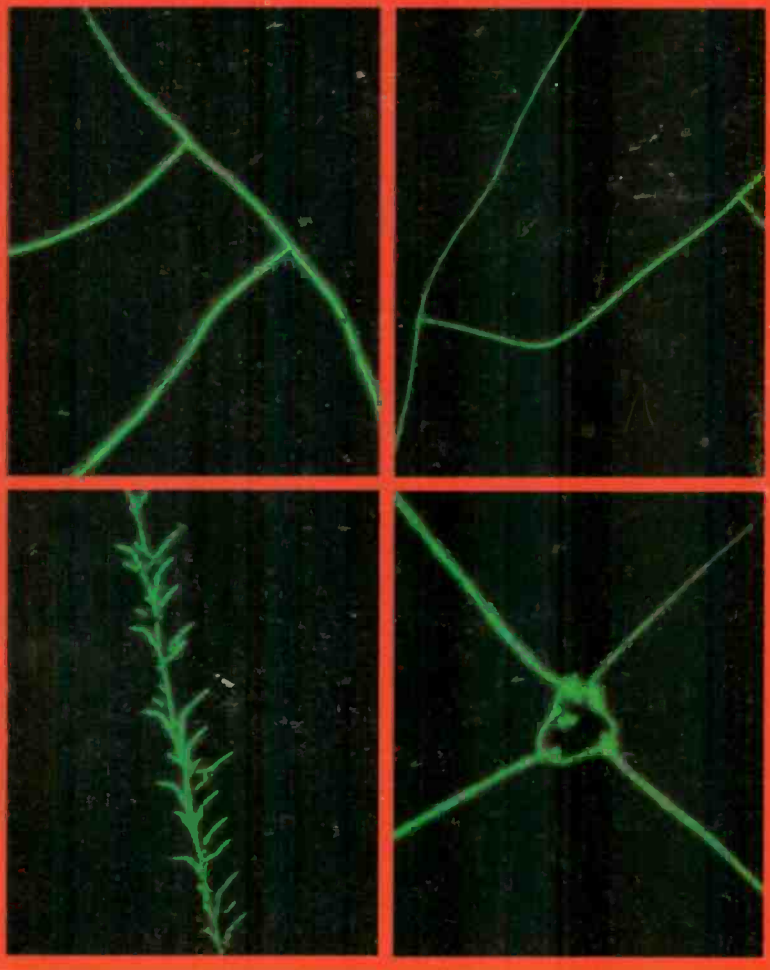

Defect Detection in Microcircuits

June 1982 Volume 43 No. 2

RCARCI 43(2) 275–420 (1982)

Cover

The four illustrations on the cover are taken from the paper by Kern, Comizzoli, and Schnable on methods developed to study corrosion phenomena and defects in dielectrics. These photos show fluorescing tracers (in this case, a green fluorescing solution of fluorescein) used to demarcate cracks in 1-μm thick glass films on aluminum metallization.

RCA Review, published quarterly in March, June, September and December by RCA Research and Engineering, RCA Corporation, Princeton, New Jersey 08540. Entered as second class matter July 3, 1950 under the Act of March 3, 1879., Second-class postage paid at Princeton, New Jersey, and at additional mailing offices. Effective January 1, 1978, subscription rates as follows: United States and Canada: one year $8.00, two years $14.00, three years $18.00; in other countries, one year $8.60, two years $15.20, three years $19.80. Single copies (except for special issues) up to five years old $3.00.

RCA Review

RCA Review (ISSN 0033-6831) is a technical journal published quarterly by RCA Research and Engineering in cooperation with the subsidiaries and divisions of RCA.

Contents

277 **An Optical Communications Link in the 2.0–6.0 GHz Band**
Daniel W. Bechtle and Stefan A. Siegel

310 **Fluorescent Tracers—Powerful Tools for Studying Corrosion Phenomena and Defects in Dielectrics**
Werner Kern, Robert B. Comizzoli, and George L. Schnable

339 **Simplified Analysis of Kinescope Electron Guns**
D. A. de Wolf

363 **Miniature Beryllia Circuits—A New Technology for Microwave Power Amplifiers**
F. N. Sechi, R. Brown, H. Johnson, E. Belohoubek, E. Mykietyn, and M. Oz

375 **Interpreting the Beta Versus Collector Current and Temperature Characteristics of a Transistor**
Robert Amantea

391 **Positive and Negative Tone Near-Contact Printing of Contact Hole Maskings**
Lawrence K. White

412 **Authors**

418 **Patents**

June 1982 Volume 43 Number 2 ISSN 0033-6831

RCA Corporation

Thornton F. Bradshaw Chairman and Chief Executive Officer

Editorial Advisory Board

Chairman, **J. J. Tietjen** RCA Laboratories
G. C. Hennessy RCA Laboratories
H. Kressel RCA Laboratories
J. Kurshan RCA Laboratories
W. J. Merz Laboratories RCA, Ltd.
K. H. Powers RCA Laboratories
R. E. Quinn RCA Laboratories
C. C. Richard International Licensing
A. H. Teger RCA Laboratories
W. M. Webster RCA Laboratories
B. F Williams RCA Laboratories

Editor Ralph F. Ciafone

Associate Editors

D. R. Higgs Missile and Surface Radar
C. Hoyt Consumer Electronics Division
T. E. King RCA Research and Engineering
R. Mausler National Broadcasting Company
M. Rosenthal RCA Americom, Inc.
J. Schoen Solid State Division
M. G. Pietz RCA Advanced Technology Laboratories
W. S. Sepich Commercial Communications Systems Division
J. E. Steoger RCA Service Company
D. Tannenbaum Government Communications Systems

© RCA Corporation 1982. All rights reserved, except that express permission is hereby granted for the use in computer-based and other information-service systems of titles and abstracts of papers published in RCA Review.

An Optical Communications Link in the 2.0–6.0 GHz Band*

Daniel W. Bechtle and Stefan A. Siegel
RCA Laboratories, Princeton, NJ 08540

Abstract—This paper describes the development, test, and evaluation of a fiber-optic communications link with rf modulation over the 2.0- to 6.0-GHz band. For this study, a variety of RCA developmental CDH lasers were operated at 0.82 micrometers with both a 2-meter short link and a 1.1-km long link with single-mode fibers. Techniques are described for optimizing link performance over the wide instantaneous bandwidth. They include impedance matching, reduction of parasitics, and optical alignment of the fiber to the laser.

A model of signal response and noise distribution was developed for the overall link and for both the detector and laser components. The frequency response, noise, group delay, phase shift, and power linearity were studied in detail over the 2.0 to 6.0 GHz band. The study indicates that high performance fiber-optic links can be built to replace conventional waveguide or coaxial lines for many diverse applications, such as microwave communications, coherent rf delay lines, and feed lines for microwave phased arrays.

1. Introduction

Single-mode optical fibers offer many advantages over conventional waveguides or coaxial lines when carrying light modulated at microwave frequencies for applications requiring rf delay and general data transmission. For many applications, optical transmission systems offer superior performance with regard to bandwidth, attenuation, distortion, size, weight, and cost. In the course of developing, charac-

* This program was sponsored in part by WPAFB through contract No. F33615-80-C-1093.

terizing, and evaluating fiber-optic links, we have investigated transmission of signals in the 2.0- to 6.0-GHz band over 1.1 km of fiber.

The investigations show that the link's SNR (signal-to-noise ratio) and distortion are limited not by the fiber but mainly by the noise and distortion of the laser, amplifier distortions, the thermal dissipation of the APD (avalanche photodiode), the frequency responses of the laser and APD, and the effects of optical feedback. Modeling indicates that with high-efficiency optical isolators, links up to 4–6 km can be built with only slightly degraded performances compared to that of the 1.1-km link. In particular, in the 2.0- to 4.0-GHz band, the group delay distortions are well within communications-amplifier standards, and the SNR for an AM heterodyned TV signal would be some 5 to 20 dB lower than the TV-studio standard of 60 dB at midpower.

Impedance-matched microstripline mounts for the diode laser and APD were developed, along with laser/fiber coupling techniques. RCA developmental CDH (constricted double heterojunction) diode lasers[1] operating at 0.83 μm were used. Wideband transmission across the 2.0- to 4.0-GHz band, and narrowband transmission up to 6.0 GHz were investigated with regard to frequency response, noise distribution, group delay, distortion, linearity, coupling efficiency, and optical feedback. Device characteristics were separated where possible.

The 1.1-km link and its separate components and the current performance levels of a 1.1-km link and a 2-m test link are discussed in Sec. 2. The two links differ mainly by the characteristics of their lasers. In Sec. 3, the separate components and their interfaces are presented in more detail. The signal and noise distributions of the link are modeled and the experimental distributions are given in Sec. 4. The experimental distributions are then used in Sec. 5 to estimate the signal and noise for the link with modeled filtering. The phase shifts of the links are discussed in Sec. 6. Conclusions are presented in Sec. 7. Some of the considerations in the construction of a microwave-optical link are reviewed as they occur in the sections. The theoretical frequency responses and phase shifts of the laser and detector are discussed in Appendix 1. The basis for the link modeling is given in Appendix 2.

2. Fiber-Optic Link: Performance and Components

2.1 Baseline Systems

Several CDH diode lasers were used in this study. Shared characteristics are discussed using the generic term "laser," while individual characteristics are discussed using a shortened device number. Specif-

by the inverse transit time (50 MHz), out to 4 GHz where the amplifier noise buried it. The effects became negligible only when the coupling loss was increased to 12 dB. The long link with single-mode fiber showed a broad increase in the noise near the laser resonance, which only became negligible when the coupling loss was increased to 16 dB.

As will be discussed, the thermal limitations of the APD and the domination of the noise spectra by the laser noise permit these high coupling losses without sacrifice of signal-to-noise ratio. Longer fiber runs, or the use of a nonmultiplying PIN diode as a detector, would require lower coupling loss and the use of optical isolation to preserve the signal-to-noise ratio.

3.7 Fiber-Detector Interface

The light from the fiber is focused onto the APD by a relay lens. This allows easy control of the attenuation.

3.8 The Detector

Two types of commercial detectors were used in this study, the PIN photodiode Ford Aerospace L4501* and the avalanche photodiode or APD AEG Telefunken S171P, BPW 28.** The PIN diode uses a low back-bias voltage and produces a current proportional to the incident light power. The current is essentially independent of bias voltage and weakly dependent upon temperature. The APD has internal gain in its avalanching region, where the photoelectrons are accelerated by a high field and knock loose additional electrons by impact ionization. The gain is also linear, but it is highly dependent upon bias voltage and temperature.

In the commercial package, the APD has an absolute maximum thermal dissipation of 100 mW. At the maximum current gain of 200, this corresponds to about 8 μW of optical power. Since the lasers put out about 7 mW, there would be, in a lossless system at full APD gain, an excess of well over 30 dB of optical power and APD gain. In the 1.1-km link, the laser and the fiber were deliberately misaligned to mitigate the optical feedback. The resulting optical-power loss was 15 dB. The 1.1-km fiber added another 4.5 dB. Finally, the APD gain was reduced to about 10 where it was quieter but was still in the high-frequency avalanche region.

* Ford Aerospace, Newport Beach, CA.
** AEG Telefunken Corp. U.S.A.; Somerville, NJ.

The frequency responses of both devices are limited by transit-time effects and internal capacitance as discussed in Appendix 1.

3.9 APD and PIN: Reflection Coefficients

At low frequencies, both the APD and PIN detectors are usually considered to be high impedance current sources with 1- to 3-pF device/package capacitances. However, our reflection coefficient measurements in the 2.0- to 6.0-GHz range indicated that the commercially packaged devices have more complicated behavior, and that broadband matching to the amplifier's 50-Ω impedance would be difficult.

As a consequence, a new impedance-matched detector mount was developed.

3.10 Preamplifier and Filter

A preamplifier and a filter prior to the amplifier were not part of the experimental links but are included conceptually for impedance matching and for shaping of the frequency response of the link. Experimentally, the APD was matched to 50 Ω and directly amplified by a commercial GaAs FET amplifer.*

4. Modeling of the Link Signal and Noise Distributions

This section discusses a computational model of the signal and noise distributions of the fiber-optic link. Experimental parameters from laser #6B at nearly full modulation are used in discussing the effects of the link with various filters on a transmitted single-frequency signal.

4.1 Simplified Signal and Noise Distributions

The effects of the separate link components on the signal are discussed in more detail in Appendix 2. The formalism includes provision for a second harmonic generated by the laser and for an additional laser mode that is out of phase with the main mode due to the optical dispersion of the fiber. In our studies the second harmonic was separately monitored, and the group delay measurements showed little or no effect of optical dispersion or of laser multimoding. For simplicity those terms are dropped in this section. Also, the rf amplifier was dc-blocked, and the signal source was relatively noiseless. Finally, for this section, the integration can be replaced by summation in finite band-

* WJ6510-434, Watkins Johnson Co., Palo Alto, CA.

widths. This gives a simplified power output of the amplifier of

$$\frac{1}{2}K^2 I_A{}^2 G R_a \frac{M^2(f)}{M^2(O)} m^2(f) A(f)$$

$$+ I_A{}^2 \frac{G R_a}{P_o^2} \frac{P_{nl}^2(I_o)}{B_l} \sum_{\tilde{f}} \frac{M^2(\tilde{f})}{M^2(O)} n^2(\tilde{f}; I_o) A(\tilde{f}) \Delta \tilde{f} \qquad [8]$$

$$+ 2qI_A M(O) F_s G R_a \sum_{\tilde{f}} \frac{M^2(\tilde{f})}{M^2(O)} A(\tilde{f}) \Delta \tilde{f}$$

$$+ GkT \sum_{\tilde{f}} F(\tilde{f}) A(\tilde{f}) \Delta \tilde{f}$$

where
- K = depth of rf modulation of laser, using dc power curve
- $I_A = \alpha R M(O) P_o$ = (direct current through detector)
- α = total optical power attenuation between laser and APD
- P_o = optical power out of laser at the operating bias current, I_o
- R = unit gain responsivity of detector
- G = nominal gain of the rf amplifier
- R_a = impedance of amplifier, detector, and laser (taken as a common 50-Ω here)
- $M(f)$ = frequency-dependent current gain of detector, $M(O)$ at dc
- $M(O)$ = direct current gain of detector; 10–200 for APD, depending on bias voltage; unity for PIN
- $m(f)$ = the laser's frequency-dependent modulation index; unity at low frequency
- $A(f)$ = power-attenuation distribution of filter
- P_{nl}^2/B_l = noise power constant for laser in W^2/Hz
- $n(f)$ = laser's optical noise power distribution, normalized to unity at its maximum
- F_s = excess noise factor of detector; unity for PIN, 3–5 for APD, increasing with APD gain[21]
- $\tilde{f}, \Delta\tilde{f}$ = frequency variable and frequency interval for summation
- q = electronic charge
- kT = Boltzmann's constant times absolute temperature of the amplifier
- $F(f)$ = noise factor of amplifier

Summation is taken over all frequencies.

The first term of Eq. [8] is the transmitted signal, and it is proportional to the square of the APD current. It contains form factors from

the laser, APD, and filter-amplifier. The laser-contributed noise (second term) is also proportional to the square of the APD current and has the same form factors as the signal. The APD-contributed noise (third term) is proportional to the APD current and has the APD and filter form factor. The amplifier noise (fourth term) depends only on its own and the filter's form factor. At those frequencies and optical power levels where the laser is the dominant noise source, the SNR is only a weak, monotonically increasing function of APD current.

4.2. Numerical Estimates: Parameters and Distributions

The parameters and distributions are estimated by both direct measurement and by differences in direct measurements.

First the amplifier noise and small-signal gain were measured by the manufacturer in 0.5-GHz intervals. The given measurements were interpolated to 0.1-GHz intervals and used to estimate the noise power of the amplifier,

$$P_3 = kTBGF(f)A(f), \qquad [9]$$

where there was no external filter but $A(f)$ is used to account for slow variations in gain. The summation interval, B, was 0.1 GHz.

Next, the APD noise power distribution was extracted by differences. The APD was connected to the amplifier and a tungsten lamp was used to illuminate the APD enough to draw 200 μA at -130V bias voltage. The tungsten lamp was assumed to be an optical-noise source flat across the band. At each frequency, the narrow-band noise power was first measured without the APD illuminated, giving only the amplifier noise, P_3. The noise power was then measured at the same frequency with the APD illuminated, also giving the APD noise, P_2, as in

$$P_2 + P_3 = 2qI_A M(O)F_s GR_a \frac{M^2(f)}{M^2(O)} A(f)B + P_3. \qquad [10]$$

The difference between the two levels was used to determine their ratio,

$$(P_2 + P_3)/P_3; \qquad [11]$$

with P_3 estimated, P_2 could also be estimated. This method is an approximation to phase-synchronous detection.[22] Due to irregularities in the spectrum analyzer's noise floor, only the ratio of powers could be determined.

The same procedure was used with a laser illuminating the APD at the same optical power level as had been provided by the tungsten

source. The noise power level was then

$$P_1 + P_2 + P_3$$
$$= I_A{}^2 \frac{GR_a}{P_o{}^2} \frac{P_{nl}^2(I_o)}{B_l} \frac{M^2(f)}{M^2(O)} n^2(f)A(f)B + P_2 + P_3, \qquad [12]$$

with a measured level of $P_1 + P_2 + P_3$ times K. The ratio

$$(P_1 + P_2 + P_3)/P_3 \qquad [13]$$

was determined by turning off the laser. The laser excess noise, P_1, was then estimated by the difference between the noise with the laser and the noise with the tungsten bulb illuminating the APD at the same optical power level.

All three terms of the noise power distribution measured above, along with their sum (the total noise), all normalized to 0.1-GHz intervals, are plotted logarithmically in Fig. 4. The laser noise dominates in the 2.5- to 4.0-GHz region, while the APD dominates below 2.5 GHz and the amplifier dominates above 4.0 GHz. As the laser and APD noise were difficult to estimate above 4.5 GHz, those points are not included on the graph. True phase-synchronous detection would be necessary to extract them above 4.5 GHz.

The frequency response of the short link, measured with nearly full

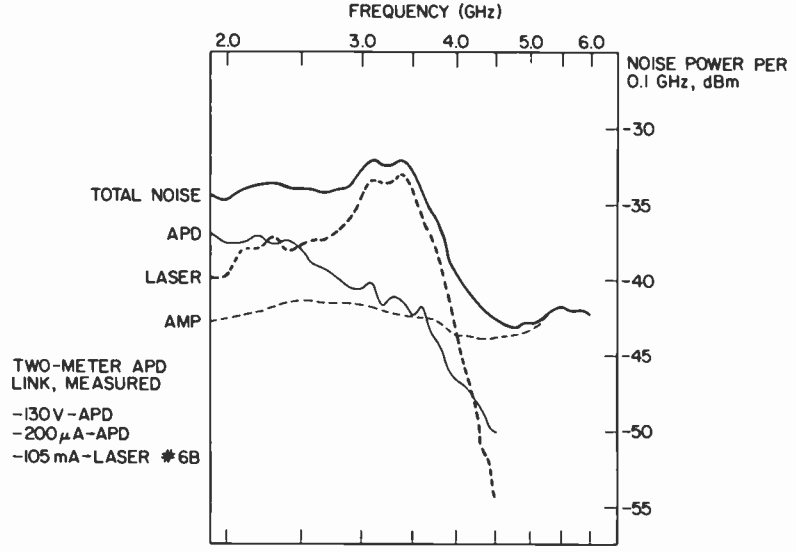

Fig. 4—Noise power distribution of the 2-m link, laser #6B. The noise power per 0.1 GHz is broken into the three major contributions using the formulation in the text.

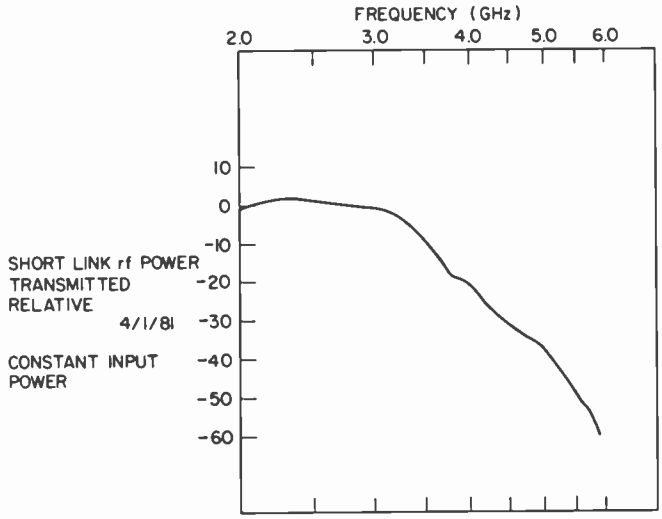

Fig. 5—Frequency response of 2-m link, laser #6B. The laser, in rf series with the matching 47-Ω resistor, was modulated at a constant 14.0 dBm across the band, and the output power of the link was monitored with a spectrum analyzer. The response was normalized to unity across the 2.0- to 3.2-GHz band where it was relatively flat.

modulation depth, $K = 0.91$, is shown in Fig. 5. A spectrum analyzer was used to detect the signal.

4.3 Observations

The signal and noise measurements can then be used to extract the frequency-dependent distributions. Since the APD-noise power distribution is equal to frequency-independent terms times the APD response, $M^2(F)/M^2(O)$, the frequency response is equal to the noise power normalized to 0 dB at low frequencies. This is shown in Fig. 6, where the normalization is approximate due to the low-frequency limitations of the amplifier. With the other parameters known, the product, $M(O)F_s$, is equal to 35. This is in agreement with the specified multiplication, $M(O)$, of 10 at −130 V for the BPW28* APD and an expected excess noise factor[21] of 3–5 for an APD.

With the APD response estimated, the laser signal and noise responses can be estimated. In Appendix 2 the laser-noise distribution, n^2, is arbitrarily defined as unity at its maximum. Under these conditions, the laser-noise distribution, n^2, is as shown in Fig. 7.

The laser signal response is similarly extracted, as shown in Fig. 8.

* AEG Telefunken Corp. U.S.A., Somerville, N.J.

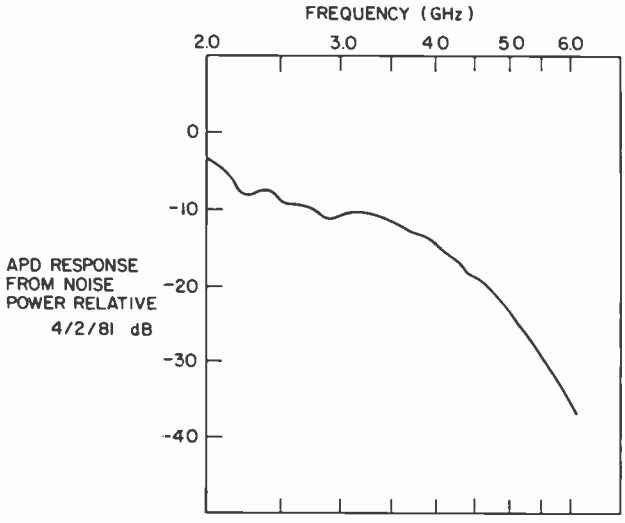

Fig. 6—APD normalized noise power distribution. The frequency response of the APD, $M^2(f)/M^2(O)$, is equal to the noise power distribution normalized to unity at low frequency. The normalization in the graph is approximate due to the 2.0- GHz lower edge of the amplifier.

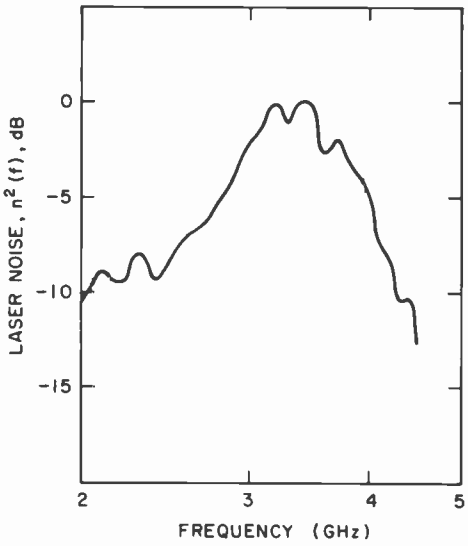

Fig. 7—Laser excess noise distribution, $n^2(f)$, laser #6B. The laser excess noise was extracted from the link's laser noise distribution, P_l of Eq. [12] and the heavy dashed curve of Fig. 4, by dividing P_l by the frequency response of the APD and normalizing the distribution to unity at its maximum.

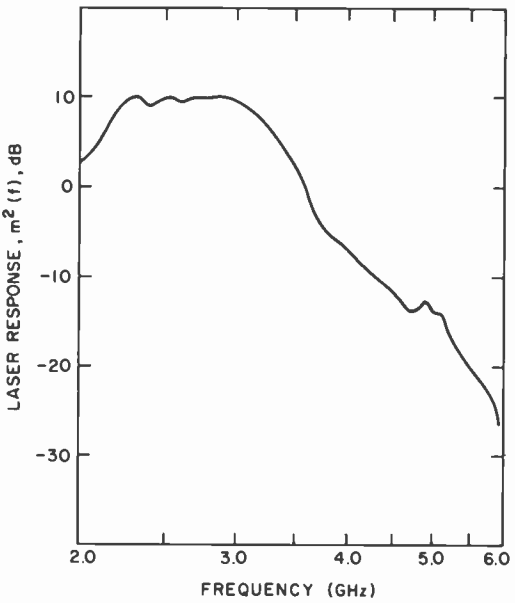

Fig. 8—Laser response, $m^2(f)$, laser #6B. The laser response was extracted from the link's frequency response, first term of Eq. [8], and Fig. 10, by dividing the first term by the frequency response of the APD and normalizing the distribution to unity at low frequency.

Again the normalization is approximate since the amplifier is limited to 2.0 GHz.

There are several important points to note about these distributions. The laser signal response is to be compared with the theoretical response, as shown in Fig. 13 (Appendix 1). The major difference is that the actual response rolls off more quickly than the expected 12 dB/octave. The laser noise has the same resonance followed by a quick roll-off. The APD response rolls off slowly out to about 3.5 GHz, and then rolls off quickly above that. This is similar to the response expected from a model (discussed in Appendix 1) in which the shunt capacitance produces a roll-off asymptotic to 6 dB/octave, followed by a steep roll-off to a cut-off frequency inversely proportional to the characteristic transit time.[21]

The laser-noise measurements can be compared with those of H. Jäckel and T. Paoli.[23,24] Jäckel, working on lasers somewhat similar to ours, found a noise behavior remarkably like that expected for the signal response, m^2. In contrast, Paoli found that an ion-implanted diode laser showed a sharp peak at resonance followed by a plateau about 10-dB lower on the high-frequency side.[24] Available theories predict a monotonic high-frequency roll-off.[25]

Both the signal power and the laser-noise power are proportional to the square of the APD current, so that increasing the APD current will not greatly increase the overall SNR as long as the laser noise dominates. Increasing the APD voltage can increase the APD noise since the excess-noise factor, F_s, increases with voltage. Since the frequency response does not change by much once the APD is biased into the avalanche region, the best operating point is as low in the avalanche region as possible. The excess of light power in the 1.1-km link allowed operation at the relatively low gain of 10 at −130 V for the remounted BPW28 chip. If the link were increased by a few kilometers, then the APD voltage could be increased to allow operation further up in the avalanche region, where the device is noisier. For that reason the performance of the link would be degraded but not proportionally to the increased length.

5. Filter Modeling

The measured signal and noise distributions also allow the effects of various filters to be estimated. In the model, the power attenuation of the filter, $A(f)$, is calculated at 0.1-GHz intervals and multiplied by the signal and noise per 0.1 GHz. The noise is then summed over the band.

The signal and integrated noise of an ideal flat 2.0- to 4.0-GHz bandpass filter were estimated in this manner. They are shown in Fig.

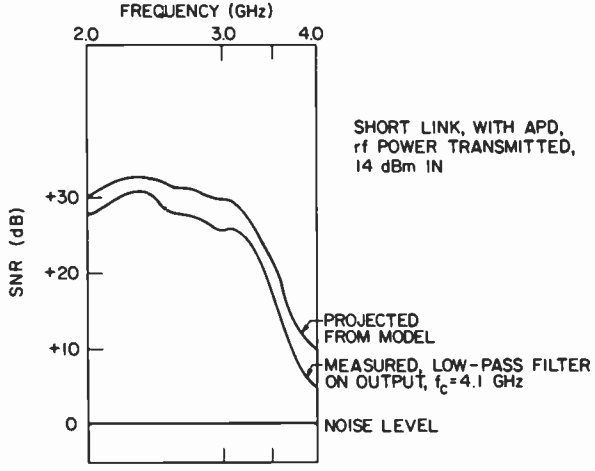

Fig. 9—2-m Link frequency response, 2.0- to 4.0-GHz, power meter. The 2.0-GHz lower edge of the amplifier and a 4.1-GHz low-pass filter were used to simulate a bandpass filter. The signal power was measured across the band with a power meter.

Table 2—Estimated SNRs for 1-km Links Incorporating Ideal Filters (Response Flattened in Passband, Cut Off Outside Passband)

Band (GHz)	Full-Band, Full-Power SNR (dB)	5 MHz Channel, Half-Power SNR	
		Maximum (dB)	Minimum (dB)
2.0–3.0	34	56	52
2.0–3.5	28	56	44
2.0–4.0	21	56	39
2.0–4.5	16	56	33
2.0–5.0	10	56	26
3.7–4.2	20	42	36
4.0–5.0	10	39	26

9 together with the signal and integrated noise measured when a somewhat wider passband was used. The measured SNR is 2–5 dB lower than the modeled SNR.

Other ideal filters can be incorporated into the model to give an idea of link performance. The ideal filters are specifically modeled to flatten the signal response inside a passband and cut off outside the passband. The SNR and absolute signal power for these filters are given in Table 2, along with the half-power SNR for an AM heterodyned TV channel, 5-MHz wide. A typical standard for broadcast-studio-quality half-power SNR is 60 dB.

6. Group Delay and Distortion

Another important aspect of a microwave-optical link is the signal distortion. The group delay is the first derivative of the phase shift of the signal with respect to frequency, and distortion is measured by taking the higher-order derivatives. The second-order derivative of phase is the linear group delay.

The small-signal phase shifts were measured by means of a phase-locked automatic network analyzer based on a stable synthesizer.

First, the amplifier's group delay was measured, as shown in Fig. 10. The group delay measured with a less accurate, commercial time-delay indicator is also shown. The group delay showed a smooth drop of about 1.5 ns between 2.0 and 2.8 GHz before leveling off. The linear group delay was under 0.0035 ns/MHz.

The group delay of the 2-m link, with laser #6B, was measured next. It had a linear group delay under 0.0070 ns/MHz across the 2.0- to 4.0-GHz band. When the amplifier group delay was subtracted, the remaining laser/fiber/APD group delay, as shown in Fig. 11, produced

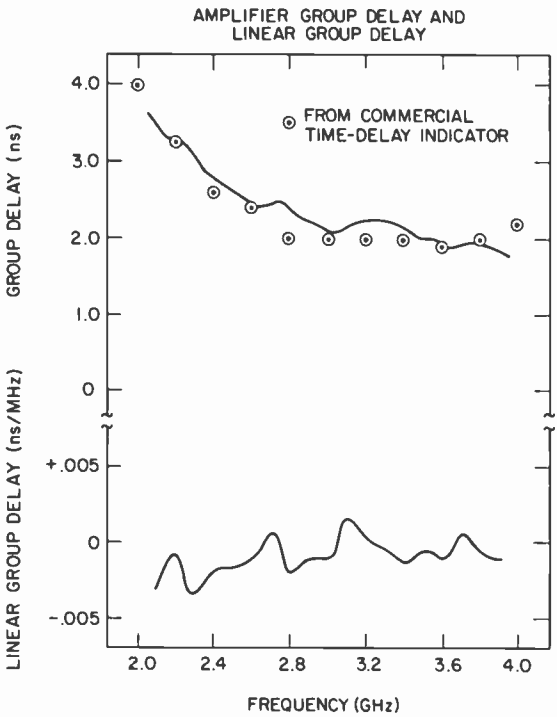

Fig. 10—Amplifier group delay and linear group delay. The group delay was measured using a network analyzer and taking the first derivative of phase in 50-MHz intervals.

a gradual curve, peaking near the laser resonance. This was in keeping with the broad resonance peak in the frequency response, as was shown in Fig. 8.

The group delay of the 1.1-km link using laser #66 was measured next, as shown in Fig. 12. With the delay of the amplifier subtracted, the remaining laser/fiber/APD group delay showed a slow rise of about 0.2 ns/GHz, with the greatest distortion occurring near the laser resonance at 4.0 GHz. There appears to be little or no distortion due to the fiber's bandwidth or to any multimoding of the laser. The group delay of laser #66 appeared oscillatory in contrast to the smoothly varying group of laser #6B in the short link. The 1.1-km link, laser #66, showed a linear group delay under 0.0035 ns/MHz out to 3.9 GHz with a maximum of 0.011 ns/MHz at 4.0 GHz. These measurements can be compared to a typical acceptance level for distortion in communications amplifiers of 0.0100 ns/MHz.

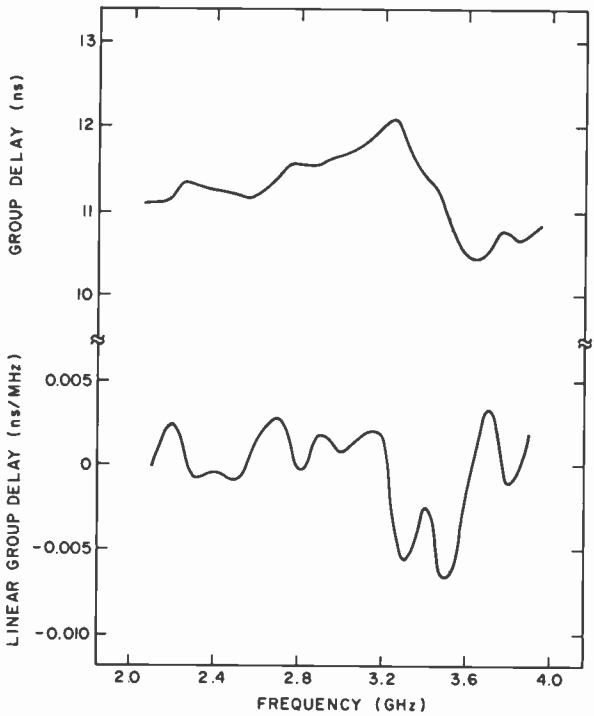

Fig. 11—Laser/fiber/APD group delay and linear group delay, laser #6B. The small-signal group delay was measured using a network analyzer and the amplifier group delay was subtracted. The remaining group delay is characteristic of the laser and APD alone and peaks near the laser resonance.

7. Conclusions

The components and interfaces of a fiber-optic link operating in the 2.0- to 6.0-GHz band were studied individually, and a complete link was developed. The work shows that with currently available components, high-performance broadband microwave links can be built. Such links could replace conventional waveguide or coaxial lines in many applications, such as rf delay lines and phased arrays, and could also be used in diverse applications previously not feasible. Among the areas to explore for greater link length/delay and bandwidth are higher-frequency/power lasers, one candidate being RCA's recent LOC (large optical cavity) laser; low-feedback, high-efficiency laser/fiber coupling; higher-frequency detection obtained with developmental devices; configuration of operational system; and operation in the lower-

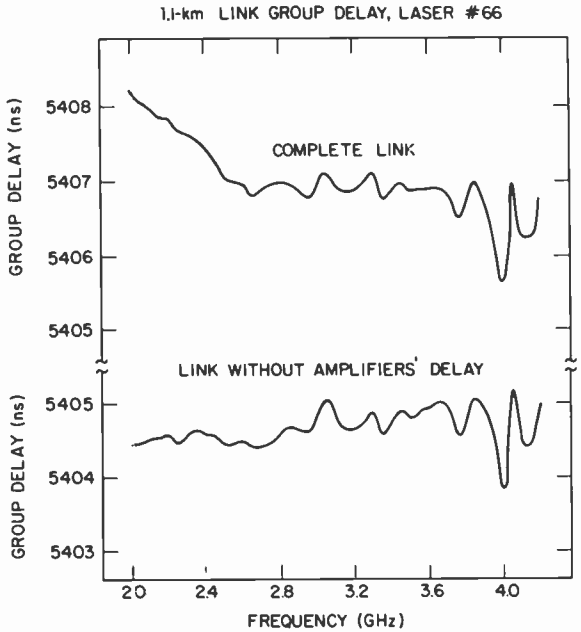

Fig. 12—Complete 1.1-km link group delay, laser #66. The group delay of the 1.1-km link with and without the amplifier group delay is shown. The delay with laser #66 oscillates near the laser resonance at 4.0 GHz instead of peaking like the 2-m link with laser #6B. The linear group delay, not shown, had a maximum of 0.011 ns/MHz at 4.0 GHz.

loss, dispersionless, 1.3-μm-wavelength region made possible by the use of developmental devices.

Appendix 1—Laser and APD Frequency Responses and Phase Distortions

The laser's frequency response is governed mainly by the rate equations for the photon and electron-hole densities.[2,25–27] The equations of state in the linear approximation are coupled first-order differential equations:

$$\frac{dn_1}{dt} = \frac{I_1}{eV} - \frac{n_1}{\tau_s} - Gn_1S_1 \qquad [A\text{-}1]$$

$$\frac{dS_1}{dt} = Gn_1S_1 - \frac{S_1}{\tau_p} \qquad [A\text{-}2]$$

where n_1 = electron density
S_1 = photon density
I_1 = electric current
e = electronic charge
V = volume of active region
τ_s = electron-hole recombination (~1 ns)
τ_p = photon lifetime in active region (~1 ps)
G = a constant

and the numerical values for τ_s and τ_p are rough estimates based on the laser parameters. A standard analysis for small signals, where $S_1 \rightarrow S_o + S$, $I_1 \rightarrow I_o + I$, $n_1 \rightarrow n_o + n$ and where S_o, I_o, n_o are steady state and S, I, and n are small modulations, eventually yields

$$I = \frac{I_{th}}{S_o}\left[\left(\tau_p \tau_s \frac{d^2S}{dt^2}\right) + \left(\frac{I_o}{I_{th}}\tau_p \frac{dS}{dt}\right) + \left(\frac{I_o - I_{th}}{I_{th}}\right)S\right], \qquad \text{[A-3]}$$

the differential equation for a damped, driven, harmonic oscillator. At a modulating frequency, f, the differential current, I, equal to $I'\sin 2\pi ft$, drives the differential photon density, S. The light power out is proportional to S^2/I^2:

$$P_{rf} \propto m^2 = \frac{1}{(1 - f^2/f_o^2)^2 + f^2 t_2^2} \qquad \text{[A-4]}$$

with

$$f_o^2 = \frac{1}{4\pi^2 \tau_p \tau_s}\left(\frac{I_o - I_{th}}{I_o}\right) \qquad \text{[A-5]}$$

and a damping term, t_2, equals $2\pi\ \tau_p \left(\frac{I_o}{I_o - I_{th}}\right)$

The effective modulation depth, m, is unitary at low frequencies and peaks near f_o. This theoretical response is shown in Fig. 13 for $f_o = 3.1$ GHz. In the figure, the laser bias current, I_o, is taken as 1.5 times the threshold current, and two damping terms are used. One term uses the estimate of a 1.0-ps photon lifetime in the active region based on the active region dimensions and facet reflectivity and yields a resonance maximum of 28 dB. The second damping term was adjusted to give a resonance maximum of 10 dB, more in keeping with experimental measurements of laser #6B biased at 1.5 times threshold current where the resonance is at 3.1 GHz. It assumes the damping is due to other mechanisms.

With the rough values for τ_p and τ_s, the bias current, I_o, varies from 1.1 to 1.5 times the threshold current; the resonant frequency then will vary from 1.6 to 3.6 GHz. The estimates of f_o are in rough agreement

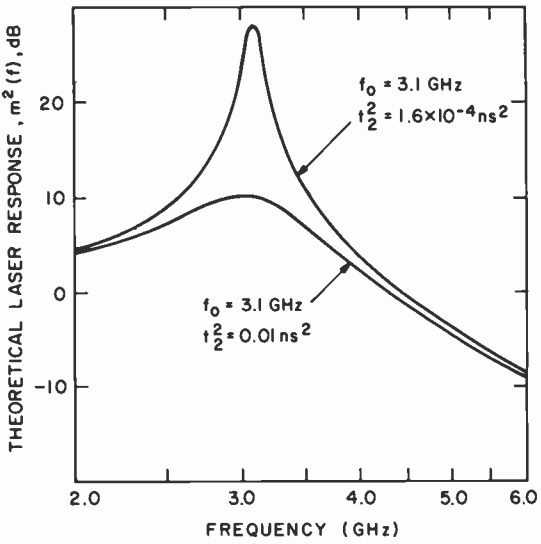

Fig. 13—Small signal frequency response of laser, $m^2(f)$, theoretical. Two curves with different damping are shown. The more heavily damped, broader curve is to be compared to the experimental large-signal response, as shown in Fig. 8, which shows a broader maximum and faster roll-off than the theoretical response.

with the diode lasers studied here. However, as Fig. 8 in the main text shows, the damping is usually much heavier, and the high-frequency roll-off is usually greater than the 12 dB/octave indicated by Eq. (A-4). This was seen in Sec. 4 of the main text.

The solution to the differential equation for a driven damped-harmonic oscillator also yields a phase angle between the driver and the oscillator:

$$\phi = \cos^{-1} \frac{ft_2}{\sqrt{(1 - f^2/f_o^2)^2 + f^2 t_2^2}},$$

with [A-6]

$$t_d = \frac{d\phi}{dt} = \frac{t_2(1 + f^2/f_o^2)}{(1 - f^2/f_o^2)^2 + f^2 t_2^2}.$$

The first derivative of the phase is the delay time, t_d, and it is plotted in Fig. 14 using the same two damping terms as used for the frequency repsonse in Fig. 13.

Diode lasers have a rather complicated noise behavior since they are threshold devices. The diversity of laser structures is reflected in the diversity of theories[22,25,38] and measurements[22,24] of their noise properties. Our own measurements, consistent with the reported mea-

surements, show that the laser noise is maximal at the laser resonance frequency and that it can dominate the other noise sources over a broad band, as was shown in Sec. 5.

The light is absorbed in the "intrinsic region" of the diode, and the electrons and holes migrate under the influence of the applied electric field. In an APD the holes migrate from the high-field region back through the intrinsic region to be recollected. In silicon, the hole mobility is lower than the electron mobility so that the holes' transit time is longer than the electron's. The intrinsic region can be made thinner to shorten the transit time, but at the expense of decreasing the quantum efficiency.

If the APD is impedance-matched to the amplifier, then the square of the current gain or multiplication is proportional to the rf output power. Following analysis by P. P. Webb et al.[21], and assuming that the APD is run at low multiplication and that the electron transit time is much less than that of the holes, the normalized power response of

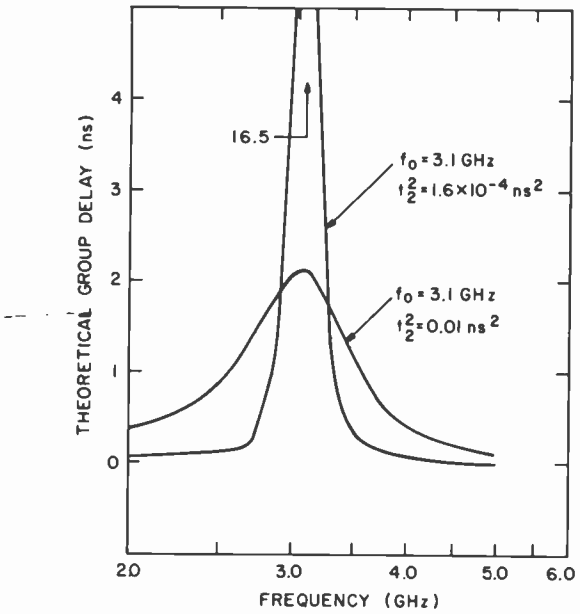

Fig. 14—Group delay of laser, theoretical. Two curves with different damping are shown. The more heavily damped, broader curve is to be compared to the 2-*m* link's group delay after the amplifier's delay is subtracted, as shown in Fig. 11. The group delay of the APD could not be extracted to allow a direct comparison but it is expected to be only slowly varying across the 2.0- to 4.0-GHz band.

the APD is approximately

$$\frac{M^2(f)}{M^2(O)} = \frac{1}{1 + 4\pi^2 f^2 R^2 C^2} \left(\frac{\sin^2 \pi f \tau_h}{\pi^2 f^2 \tau_h{}^2} \right). \qquad [A\text{-}7]$$

Note that this theoretical response cuts off completely at $f_c = 1/\tau_h$ while reverting to the usual shunt capacitance fall-off at lower frequencies. As noted below, the experimental response of the APD falls off more quickly than the 6 dB/octave of the shunt capacitance. It does not cut off completely since the hole transit time is really the weighted average of a distribution.

The simplified response also has a phase angle and relative time delay associated with it whose form depends on the RC time constant. The hole's transit time acts to spread the signal, but the average delay time stays constant with respect to frequency. If the curve of Fig. 6 is fitted to Eq. [A-7] with $RC << \tau_h$, the response appears to be 6 dB down at 2.0 GHz. The response would already be lagging the light modulation by 70° at 2.0 GHz, so that the phase angle would slowly increase to nearly 90° until the transit-time effects took over at about 3.5 to 4.0 GHz. The APD would thus be expected to have essentially constant delay above 2.0 GHz.

Appendix 2—Modeling Formalism

In this Appendix, a formal approach is given for some of the effects that the various components of the link have on the transmitted signal. A schematic of the modeled link was shown in Fig. 2. The formalism provides for the laser having one additional mode separated in wavelength from the main mode but modulated in phase. The fiber is dispersive at 0.85 μm so that the modulation of the additional laser mode is out of phase with that of the main mode after traversing the fiber. The laser is considered nonlinear, and the formalism provides for the first harmonic. The other components are considered relatively linear. The signal source, laser APD, and amplifier all contribute noise.

A2.1 Signal Response and Noise at the Laser

The laser is forward-biased into the linear region to a current, I_o, where the main mode has optical power P_o and the additional mode has power P_o'. A single-frequency signal, with frequency f, modulates the impedance-matched laser about I_o and hence about P_o. The depth of modulation, K, is limited to about 0.8 to 0.9 by the nonlinearities the near the threshold current. Some of the rf signal is converted into the first harmonic. This has optical powers $P_2(f; K)$ and $P_2'(f; K)$ in

the two modes. The input signal current is taken to be

$$I_0\delta(\tilde{f}) + I_1\sin(2\pi ft)\delta(f-\tilde{f}) + \frac{I_{n1}(\tilde{f})}{\sqrt{B_1}}, \qquad \text{[B-1]}$$

where $\tilde{f}$ = the frequency variable
f = the modulation frequency
$\delta(\tilde{f})$ = the Dirac delta function
I_1 = the modulation current
$I_{n1}(\tilde{f})$ = the source noise current distribution
B_1 = a normalizing bandwidth

The optical power out is then

$$\begin{aligned} &P_o\delta(\tilde{f}) + m(\tilde{f})KP_o\sin(2\pi\tilde{f}t)\delta(\tilde{f}-f) \\ &\quad + m(\tilde{f})KP_o'\sin(2\pi\tilde{f}t)\delta(\tilde{f}-f) \\ &\quad + P_2(\tilde{f};K)\sin(2\pi\tilde{f}t)\delta(\tilde{f}-2f) \\ &\quad + P_2'(\tilde{f};k)\sin(2\pi\tilde{f}t)\delta(\tilde{f}-2f) \\ &\quad + m(\tilde{f})K\frac{P_{n1}(\tilde{f})}{\sqrt{B_1}} + \frac{P_{nl}(I_o)}{\sqrt{B_l}}n(\tilde{f};I) \end{aligned} \qquad \text{[B-2]}$$

where $m(f)$ = the laser's frequency dependent modulation index
$P_{n1}(f)$ = the source's noise current distribution times the slope of the laser's power-current curve in the linear region, and $P_{n1}/P_o = I_{n1}/I_1$
$P_{nl}(I_o)$ = the magnitude of the laser's optical noise power
B_l = a normalizing bandwidth
$n(f)$ = the laser's optical-noise power index, normalized to unity at its maximum

Current and optical power distributions and delta functions are used since the power will be integrated over the band and the rf signal is considered single frequency. The noise is normalized by a bandwidth to keep the units of the distributions as amperes or watts. The distributions are factored into magnitudes and frequency-dependent form factors. The modulation index is a function that peaks at the laser's resonant frequency and is unity at low frequencies. The depth of modulation, K, is determined from the peak-to-peak current through the laser, while the modulation index is a measure of the resonant response of the laser. A similar resonance occurs in the laser's optical-noise index, $n(f)$, which also peaks at the laser's resonance, f_o. For convenience, the form factor $n(f)$ is normalized to unity at f_o. Note that the optical powers and distributions are implicit functions of the bias current.

A2.2 Signal Response and Noise at the Photodiode

The light is coupled into the fiber and is refocused onto the photodiode. The optical power is attenuated by the coupling loss, the loss in the fiber, and coupling loss into the detector. For simplicity, the total loss, α, is considered equal for the main mode and the additional mode of the laser. The additional mode is now out of phase by an angle, θ, which is the product of the characteristic optical dispersion of the fiber, the wavelength separation of the modes, and the modulation frequency. A typical angle is 90° for 1 km of fiber at 0.82 μm, 10-Å separation, and 5.0-GHz modulation. If the signal were broadband, then the bandwidth of the fiber could also affect the relative phase of the signal components. This dispersion in the modulation frequency, separate from the optical dispersion, is a limiting factor in multimode fibers. Our measurements of the group delay in Sec. 6 show little or no dispersion of this kind in the 1.1-km, single-mode fiber.

The photodiode has a unit gain responsitivity, R, and current gain, $M(f)$. For a PIN diode $M(O)$ is 1; while for an APD, $M(O)$ ranges from about 10 to 200 in the avalanching region, depending sharply on bias voltage and temperature. The usual, confusing notation uses M for the APD current gain, and m for the laser's modulation index. The current out of the detector is then

$$\begin{aligned}
&\alpha RM(\tilde{f})P_o\delta(\tilde{f}) + \alpha RM(\tilde{f})m(\tilde{f})K[P_o \sin(2\pi\tilde{f}t) \\
&+ P_o' \sin(2\pi\tilde{f}t + \theta)]\delta(\tilde{f} - f) \\
&+ \alpha RM(\tilde{f})[P_2(\tilde{f}; k)\sin(2\pi\tilde{f}t) + P_2'(\tilde{f}; k) \\
&\cdot \sin(2\pi\tilde{f}t + \theta)]\delta(\tilde{f} - 2f) \\
&+ \alpha RM(\tilde{f})\left[m(\tilde{f})K\frac{P_{n1}(\tilde{f})}{\sqrt{B_1}} + \frac{P_{nl}(I_o)}{\sqrt{B_l}} n(\tilde{f}; I_o)\right] \\
&+ [2q\alpha P_o RF_s]^{1/2}M(\tilde{f})
\end{aligned} \qquad \text{[B-3]}$$

where q is the electronic charge and F_s is the excess noise factor (1 for a PIN; 3–5 for an APD, increasing with gain[21]).

The last term is the noise current distribution for an APD when the dark noise can be neglected.[21]

A2.3 Signal Response and Noise at Amplifier

The detector, preamplifier, filter, and amplifier are now taken as impedance-matched to a common impedance, R_a. The amplifier gain is G, and variations in the gain and impedance are lumped into the

filter's power response, $A(f)$. The power out of the amplifier is then shown as

$$\begin{aligned}
&\frac{1}{2}\alpha^2R^2M^2(O)P_o^2GR_aA(O)\\
&+\frac{1}{2}\alpha^2R^2M^2(f)m^2(f)K^2GR_aA(f)[P_o^2+P_o'^2+2P_oP_o'\cos\theta]\\
&+\frac{1}{2}\alpha^2R^2M^2(f)GR_aA(f)[P_2^2(f;k)+P_2'^2(f;k)\\
&+2P_2(f;k)P_2'(f;k)\cos\theta]\\
&+\alpha^2R^2K^2GR_a\int_{\tilde{f}}M^2(\tilde{f})m^2(\tilde{f})\frac{P_{nl}^2}{B_1}(\tilde{f})A(\tilde{f})\,df\\
&+\alpha^2R^2\frac{P_{nl}^2(I_o)}{B_l}GR_a\int_{\tilde{f}}M^2(\tilde{f})n^2(\tilde{f};I_o)A(\tilde{f})\,d\tilde{f}\\
&+2q\alpha P_oRF_sGR_a\int_{\tilde{f}}M^2(\tilde{f})A(\tilde{f})\,d\tilde{f}\\
&+GkT\int_{\tilde{f}}F(\tilde{f})A(\tilde{f})\,d\tilde{f}
\end{aligned}\qquad\text{[B-4]}$$

where k = Boltzmann's constant
T = absolute temperature
$F(f)$ = noise factor of the amplifier

Integration is taken over all $\tilde{f}$, and the noise sources and signal are assumed not to correlate. The delta functions fix the frequency of the signal components, and the filter determines the band of operation. The last term is the normal noise power out of the amplifier. The attenuation of the filter is assumed to be much less than the gain of the preamplifier so that it doesn't affect the overall noise figure.

The formalism was developed to provide for an additional mode as well as the first harmonic of the laser and to separate the noise sources. It can be made more tractable by replacing the integration with summation and making other simplifications.

The rf amplifier is dc-blocked so the first term vanishes. Note that the dc current is

$$I_A=\alpha RM(O)P_o \qquad\text{[B-5]}$$

and can be monitored separately.

The laser's additional mode would cause distortion in the group delay and power frequency response if the fiber were long enough and the additional mode were strong enough. Our group delay measure-

ments (Sec. 6) indicate little or no such distortion. The second harmonic can be separately monitored. The source can be taken as relatively noiseless. Then the simplified output power is as given in Eq. [8] of the main text.

References:

[1] D. Botez, "Constricted Double-Heterojunction GaAlAs Diode Lasers: Structures and Electro-Optical Characteristics," *IEEE J. Quantum Electron.*, **QE-17**(12), p. 2290 (1981).

[2] H. Kressel and J. K. Butler, *Semiconductor Lasers and Heterojunction LED's*, Academic Press, New York, (1977).

[3] W. Filensky et al., "The GaAs MESFET as a Pulse Regenerator, Amplifier, and Laser Modulator in the Gbit/s Ranges," *IEEE J. Solid-State Cir.*, **SC-12**(3), p. 276 (1977).

[4] J. Midwinter, *Optical Fibers for Transmission*, J. Wiley & Sons, New York (1979).

[5] T. Miya et al., "Ultimate Low-Loss, Single-Mode Fiber at 1.55 μm," *Electron. Lett.*, **15**(4), p. 106 (1979).

[6] Y. Murakami and H. Tsuchiya, "Bending Losses of Coated Single-Mode Optical Fibers," *IEEE J. Quantum Electron.*, **QE-14**(7), p. 495 (1978).

[7] S. Siegel to be published.

[8] I. Ladany et al., "Ultra High-Speed Modulation Studies of Injection Lasers," Final Report, Contract No. N00173-77-0136, June 1978, Optical Techniques Branch, Naval Research Laboratory, Wash. DC.

[9] D. Marcuse, *Bell Sys. Tech. J.*, **56**, p. 703 (1977).

[10] R. Lang and K. Kobayashi, "External Optical Feedback Effects on Semiconductor Injection Laser Properties," *IEEE J. Quantum. Electron.*, **QE-16**(3), p. 347 (1980).

[11] D. Kato, "Suppression of Light Feedback from an Optical Fiber into a Diode Lasers," *Opt. Commun.*, **26**(3), p. 335 (1978).

[12] A. Dandridge and R. O. Miles, "Spectral Characteristics of Semiconductor Laser Diodes Coupled to Optical Fibers," *Electron. Lett.*, **17**(7), p. 273 (1981).

[13] L. A. Glasser, "A Linearized Theory for the Diode Laser in an External Cavity," *IEEE J. Quantum Electron.*, **QE-16**(5), p. 525 (1980).

[14] O. Nilsson et al., "Oscillation Frequency, Linewidth Reduction, and Frequency Modulation Characteristics for a Diode Laser with External Grating Feedback," to be published in *Electron. Lett.*

[15] E. P. Ippen et al., "Picosecond Pulse Generation by Passive Mode-locking of Diode Lasers," *Appl. Phys. Lett.*, **37**(3), p. 267 (1980).

[16] P. T. Ho, "Coherent Pulse Generation with a GaAlAs Laser by Active Modelocking," *Electron. Lett.*, **15**(17), p. 526 (1979).

[17] Y. C. Chen, "Noise Characteristics of Semiconductor Laser Diodes Coupled to Short Optical Fibers," *Appl. Phys. Lett.*, **37**(7), p. 587 (1980).

[18] H. Kuwahara, "Optical Isolator for Semiconductor Lasers," *Appl. Opt.*, **19**(2), p. 319 (1980).

[19] E. Brinkmeyer, "Backscattering in Single-Mode Fibers," *Electron. Lett.*, **16**(9), p. 329 (1980).

[20] T. Matsumoto and K. Sato, "Polarization-Independent Optical Circulator: An Experiment," *Appl. Opt.*, **19**(1), p. 108 (1980).

[21] P. P. Webb et al., "Properties of Avalanche Photodiodes," *RCA Rev.*, **35**, p. 234 (1974).

[22] T. Paoli, "Noise Characteristics of Stripe Geometry Double-Hetero structure Junction Lasers Operating Continuously-I. Intensity Noise at Room Temperature," *IEEE J. Quantum Electron.*, **QE-11**(6), p. 276 (1975).

[23] H. Jäckel, "High-Frequency Radiation Intensity Noise Spectrum of C. W. C. H. GaAlAs-Diode Lasers," *Electron. Lett.*, **12**(11), p. 289 (1976).

[24] T. Paoli, "Intrinsic Fluctuations in the Output Intensity of Double-Heterostructure Junction Lasers Operating Continuously at 300 K," *Appl. Phys. Lett.*, **24**(4), p. 187 (1974).

[25] H. Haug, "Quantum-Mechanical Rate Equations for Semiconductor Lasers," *Phys. Rev.*, **184**(2), p. 338 (1969).

[26] P. M. Boers and M. T. Vlaardingerbroek, "Dynamic Behavior of Semiconductor Lasers," *Electron. Lett.*, **11**(10), p. 206 (1975).
[27] H. W. Yen and M. K. Barnoski, "Optical Microwave Interactions in Semiconductor Devices," Final Report, Contract N00173-77-C-0156, 1978, Naval Research Laboratory, Washington, DC.
[28] T. Ito et al., "Intensity Fluctuation in Each Longitudinal Mode of a Multimode AlGaAs Laser," *IEEE J. Quantum Electron.*, **QE-13**(8), p. 574 (1977).

Fluorescent Tracers—Powerful Tools for Studying Corrosion Phenomena and Defects in Dielectrics*

Werner Kern, Robert B. Comizzoli, and George L. Schnable**
RCA Laboratories, Princeton, NJ 08540

Abstract—Several methods are described for studying corrosion phenomena in microelectronic devices and for detecting structural defects in insulator coatings and dielectric films. These methods are based on the use of ultraviolet fluorescing materials to demarcate or decorate the sites of interest for microscopic observation.

Electrolytic corrosion sites are rendered visible by pH-sensitive fluorescing dyes under applied bias. Relatively large cracks and pinholes in insulator coatings on conductive substrates can be decorated with electrically-charged phosphor particles by either electrophoretic or electrostatic techniques. Structural micro-defects in dielectric films on any substrate are best demarcated with intensely UV-fluorescing organic tracer compounds in optimal solutions employing novel techniques that are sensitive, fast, and simple to carry out. Furthermore, the method can be extended to other types of films or bulk materials with depressed defect sites.

1. Introduction

Corrosion phenomena of metal films and the effects of structural defects in dielectric layers and insulator coatings play important roles in semiconductor device processing and reliability.[1–8] Corrosion is

* A condensed version of this paper has been published as two separate articles in *Industrial Research and Development* magazine (see references [26] and [27]).

** Present Address: Bell Laboratories, Murray Hill, N. J. 07974. The work reported here was performed at RCA Laboratories.

frequently one of the consequences of defects in the insulator coatings that protect the underlying metal structures. The detection and study of such defects are important for understanding and preventing corrosion and other reliability problems in microelectronic devices.†

In our work, we have taken advantage of fluorescing chemicals as tracers because of their sensitivity in microscopic examination, in addition to other desirable properties that serve our purposes. Inorganic phosphor powders, fluorescing organic compounds such as dyes, and organic phosphors have been employed. Ultraviolet radiation sources were used to induce fluorescence, resulting in intense yellow, green, blue, or red emission that can be observed under an optical microscope with appropriate filters, rendering the decorated or demarcated sites readily visible.

Several novel techniques developed at RCA are described and illustrated in this paper. Although developed primarily for semiconductor devices, the methods are applicable to other similar applications. References [1] to [27] identify relevant papers on corrosion, defect detection, and fluorescence methodology.

2. Study of Corrosion Phenomena with Fluorescent Indicators

The study of corrosion of small metal structures, such as integrated circuit (IC) interconnections, is complicated because such structures are analyzed after corrosion has taken place and the metal electrode has been totally or partially destroyed. Also, the corrosion product normally causes disruption of the overlying dielectric. The ability to detect those regions of an IC that are prone to corrosion enables analysis before and during the corrosion processes, and promises further advances in understanding and preventing corrosion. The use of pH-sensitive fluorescing dyes permits the failure analyst or corrosion scientist to preselect and study these regions. For example, elemental analysis before corrosion could reveal the presence of deleterious contaminants.

Corrosion, which leads to chip failure, can rapidly occur when a moisture film, ionic contamination, and potential difference exist between two metallization stripes.[5] Most modern ICs employ a highly insulating passivation layer over the metal, and currents large enough

† For papers dealing with failure analysis in microelectronics consult the IEEE proceedings of the *Annual Reliability Physics Symposia* and the annual IEEE symposia proceedings on *Advanced Techniques in Failure Analysis*.

to cause corrosion flow only if there are holes or cracks in the passivation layer (Fig. 1). The worst case for corrosion is a low-power, high-voltage chip in a plastic package with a poor passivation layer and operating in a humid environment. Corrosion is a serious failure mechanism and is quite obvious to the customer's failure analysts.

All known metals used for device interconnects can corrode under certain conditions. In particular, aluminum will corrode to form open circuits by conversion to hydroxides, and gold ions from corrosion sites may form shorts by dendrite growth. For aluminum, the pH of the moisture film is the governing factor, and corrosion occurs for pH values below 4 and above about 8. At the aluminum cathode, pH is increased since H^+ is consumed by the electrolytic action.[5]

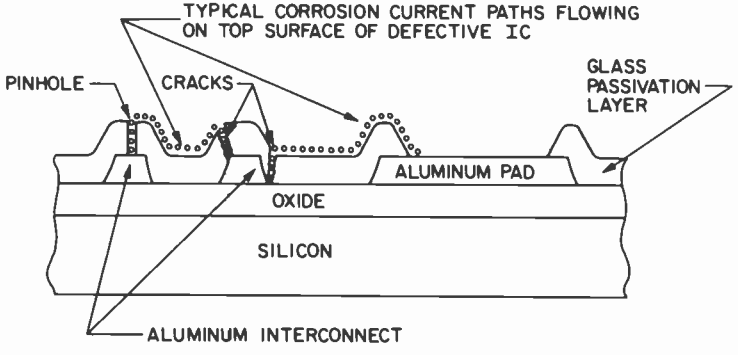

Fig. 1—Schematic cross section of a defective integrated circuit showing surface paths of corrosion current.

This pH dependence of corrosion has been used to detect those regions on an IC where corrosion can occur.[6–8,24,25] The technique uses dyes whose fluorescence under UV illumination is pH-dependent. The experimental arrangement is not complex and is shown in Fig. 2. A fixturing arrangement holds the chip, wafer, or delidded packaged device and also provides electrical bias connections. Intense long-wave UV illumination is directed onto the surface of the dye-coated sample from a lamp in close proximity. Bias is applied while the dye fluorescence is observed with an optical microscope. In some cases, it has been useful to employ a humidity-controllable probe station to adjust surface conduction. This furnishes sufficient surface moisture to provide the corrosion-inducing electrolyte.

Three dyes reveal corrosion sites or potential corrosion sites: sodium fluorescein, β-methylumbelliferone, and β-naphthol. The dyes are

dissolved in ethanol (1 to 2 × 10^{-4}M). Glycerol (1% by volume) is added to prevent rapid drying and a surfactant may be used to insure even distribution over the device. On silicon wafers, the solution can be easily applied by spinning. On single chips or delidded devices it is applied with a dropper or hypodermic syringe.

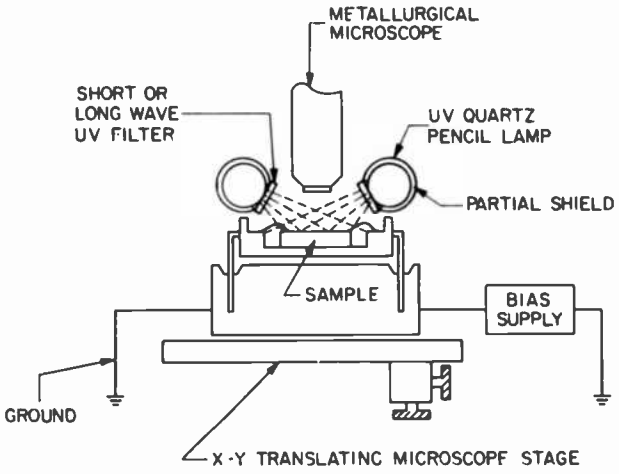

Fig. 2—Experimental arrangement for examining corrosion phenomena with pH-sensitive fluorescent dyes. A UV filter (not shown for clarity) should be used for safe viewing of the microscopic image.

With β-methylumbelliferone and β-naphthol, when a dc bias is applied to aluminum metallization under UV illumination, intense localized fluorescence can occur at one or more sites on the device. The fluorescence gradually spreads out, in an approximate circular area to cover a region several mils in diameter. After a time, a stable size is attained. If the bias is removed, the fluorescence gradually decays in area and in intensity over a period of minutes. During bias application, bubbles may also be observed at the fluorescent site, indicating that electrolysis is occurring. Voltage of 10 to 20 V is sufficient to activate the fluorescence.[7]

The presence of bubbles, which are presumably hydrogen, indicates a cathodic corrosion site. The bright fluorescence of these pH-sensitive dyes suggests that the cathode corrosion sites detected are regions of increased pH. It is known that aluminum-water corrosion reactions are favored in high pH.[5] The time dependence of the growth and decay in the fluorescing area is related to the rate of change of pH and to

electrolyte concentrations. Detailed studies of these time-dependent factors promise greater understanding of corrosion kinetics.

Gold-metallized devices exhibit a quenching of fluorescein dye fluorescence when bias is applied. The quenching occurs at regions where the anodically-biased gold is not passivated and is in contact with the dye layer. The quenching thus detects defect areas in the dielectric over the metal.[8]

These methods offer the possibility for more detailed study of the specific corrosion sites on an IC. The sites can be easily identified before much corrosion has occurred, and the tell-tale dye removed for closer examination of the defective area.

3. Detection of Defects in Insulators by Electrophoretic and Electrostatic Decoration with Phosphors

3.1 Types of Defects

The detection of localized structural defects in layers of insulating and dielectric materials is another important area in semiconductor microelectronics technology.[1,2] For example, silicon integrated circuits require a passivation layer as overcoat to afford scratch resistance of the interconnect metallization during processing and to prevent alkali ions and other impurities from contaminating the packaged device. Chemically vapor-deposited films of phosphosilicate glass or silicon nitride are generally used as the passivation overcoat. In some cases, however, such layers may have cracks, pinholes, or inadequate coverage of the edges of delineated lines of conductors or of thin-film resistors. These defects can result in device failure as a result of corrosion or of oxidation of thin-film resistors, leading to serious reliability problems; they must therefore be controlled and minimized. Conventional test methods to evaluate the quality of glass layers on semiconductor devices are generally inconvenient or destructive.

We have recently developed nondestructive detection techniques based on electrophoretic or electrostatic deposition of phosphor particles, resulting in readily visible fluorescing decoration of such defects. One technique is based on the use of a conventional electrophoretic cell; the second technique employs high-voltage charging of the sample and subsequent deposition of the phosphor from a suspension.[2–4]

3.2 Decoration by Electrophoretic Cell Method

Localized structural defects in an insulator coating on a conductive substrate can be detected by electrophoretic decoration with fluores-

cing phosphor particles. The method is akin to electroplating, except that electrically charged particles rather than metal ions are involved. The charged particles are suspended in a carrier liquid and migrate in an electric field towards the electrode of opposite polarity. A schematic of an electrophoretic cell and the essential deposition process are shown in Fig. 3.

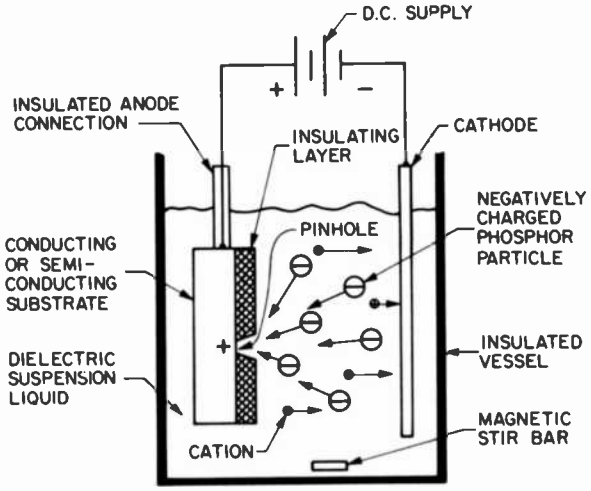

Fig. 3—Schematic illustrating electrophoresis cell method for decorating insulator defects with negatively-charged phosphor particles.

Each suspended charged particle is surrounded by an electric double layer. Application of an electric field affects the particle and the inner portion of the double layer, causing the particle to move in one direction, while the oppositely charged outer surface of the double layer moves in the opposite direction. The existing shear surface separates the double layer. The charges in the double layer give rise to an electrical potential whose value at the shear surface is known as the zeta potential; among other effects it influences the dispersion stability and the electrophoretic particle mobility. Small particles (less than 1 μm) are preferable because of the large surface-to-volume ratio which yields an abundance of short-range surface charges, thus facilitating the decorating process. Nonpolar organic insulating liquids, with surfactant or charging agent additives to achieve high zeta potentials, are preferred over polar liquids as the suspending agent. Adhesion of the particles to the surface is thereby improved, since the particle-holding image charge on the sample surface is retained. Another

advantage of insulating suspension liquids is the capability of nondestructive decoration of partial pinholes, regions where the insulator film is thinner (say tens of angstroms thick) than in the surrounding area. The particles deposit on the insulator, charging it as a capacitor up to the applied potential. The area density of particles on the surface will be inversely proportional to the insulator thicknesses, resulting in a greater particle density on thinner areas than on the surrounding thicker area.

The electrophoresis vessel can be a container of glass or plastic, or of stainless steel, in which case it takes the place of the cathode. One of the best particle materials for fluorescence decoration, out of many investigated, is small particle size manganese-activated zinc silicate (Zn_2SiO_4 : Mn) lamp phosphor, which fluoresces intensely bright green-yellow in short-wave ultraviolet light. Other useful phosphors are terbium-activated cerium-terbium-magnesium aluminate, fluorescing light-yellow in short-wave UV; and europium-activated yttrium vanadate, fluorescing bright red. Copper-aluminum-activated zinc-cadmium sulfide fluoresces lemon-yellow in long-wave UV radiation. The most frequently used suspending liquid in our work is trichlorotrifluoroethane ($C_2Cl_3F_3$, Freon TF® from DuPont), with petroleum barium sulfonate or OLOA 1200 (Chevron) as additives to provide negative net electrical charge on the decorating particles in the liquid vehicle. Typical mixtures we have used successfully consist of 0.25 wt/vol% of the phosphor in $C_2Cl_3F_3$ containing 0.0025% of OLOA 1200 charging agent.

The sample is immersed in the suspension at a spacing of 1.2 to 1.7 cm from the opposite electrode. A constant voltage of 10 to 500 V is applied for 30 sec to 10 min. The voltage and deposition time used depend on the particle mobility, density, and concentration in the liquid, and on the degree of decoration to be attained. A potential of 25 V for 5 min generally is preferred to minimize background decoration due to capacitative charging of the insulator, even though some smaller pinholes may be missed at low voltage. The sample is finally removed from the suspension while the voltage is still applied. After air drying, the sample is examined under the fluorescence microscope in filtered UV radiation. The method is particularly useful for examining relatively large defects, such as cracks and pinholes greater than 1 μm. The size of the phosphor particles impairs the decoration of smaller-sized defects. Photomicrographs of silicon device samples decorated with selected phosphors by this process are shown as examples in Plates 1–5.

3.3 Decoration by Electrostatic Charging

In this method, the dry sample surface is electrostatically charged with ions from an atmospheric-pressure glow discharge (corona), followed by immersion of the sample in the suspension of charged particles. Depending on the relative signs of the charged particles and the deposited surface ions, the particles are attracted to either the local defect sites, as shown schematically in Fig. 4, or to the charged insulating surfaces (resulting in reverse decoration). The latter leaves the defects sites and other conducting areas (such as metallization bonding pads and grid lines in integrated circuits) undecorated. Electrostatic and adsorption forces hold the particles in place for examination.

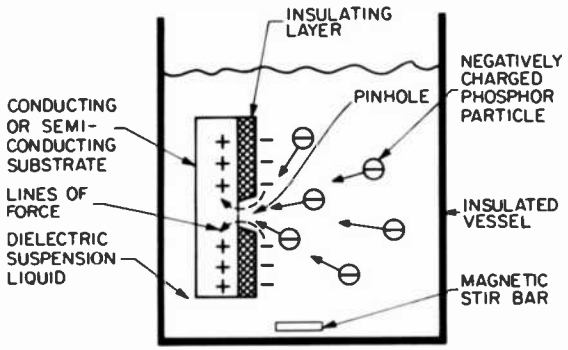

Fig. 4—Schematic illustrating electrostatic method for decorating insulator defects. The negative charge on the insulator surface is created by a corona discharge prior to immersion of the sample in the phosphor suspension. The fringing field repels negatively-charged particles from the negatively-charged surface, causing them to migrate toward the exposed conducting regions. The positively-charged ions have been omitted for clarity.

The source of ions deposited on the sample in the corona charging process is a plane array of nickel alloy wires. This grid consists of seven parallel wires 1.8 cm apart, held in an acrylic frame in a horizontal plane. The wires are commonly connected to an rf-type high-voltage dc power supply capable of ±10,000 V and 6 mA. A grounded plate 3 cm above the wires provides greater current uniformity and protects the wires from mechanical damage. The sample is placed on a grounded plate 2 cm below the wire array. The process is carried out at room temperature with relative humidity below 30% in a glove box in flowing nitrogen. When the corona voltage is set just below sparking voltage,

the oxide surface voltage reaches a steady-state value within 5 sec; for lower voltages, the time to steady state is greater.

In the actual decoration process, the surface voltage reaches steady state in about 10 sec. The magnitude of the oxide surface voltage at steady state depends mainly on the lateral geometry, rather than the thickness of the insulator pattern on the conductive substrate. Charging of a surface containing closely spaced insulator and conductor regions is limited mainly by the conducting areas. As the ions collect on the insulator, they generate an electric field in the gas ambient which causes subsequently approaching ions to move toward the ground potential regions before arriving at the wafer surface. Thus, the insulator surface voltage is not determined by the insulator breakdown potential, except for very thin or very large areas. A more detailed description of the corona charging process, the variables affecting the charging mechanism, and the apparatus used was published in previous papers.[2-4]

In the direct decoration of defects by corona charging, the sign of the corona discharge is chosen to be the same as that of the suspended particles (usually negative). Upon immersion of the sample, the particles are repelled from the charged insulator surfaces and directed towards the conducting, uncharged regions such as cracks, pinholes, and exposed semiconductor or metal surfaces. The sample, dried at 200°C, is charged negatively for 18 sec at −7000 V dc at a sample-to-wire spacing of 2 cm. After a 10-sec delay, the sample is immersed for 10 sec in the phosphor suspension described in the electrophoretic cell method. These conditions are optimal in producing a clean deposit with minimum scatter, as shown in the typical photomicrographs of Plate 6 featuring induced cracks in a 1-μm thick glass layer over an aluminum-metallized capacitor of an integrated circuit. Correlation of phosphor decoration with selective chemical metal etching is very good. Defects like microcracks and pinholes invisible by optical microscopic examination can be readily detected by this sensitive and nondestructive method. Furthermore, the high impedance of the corona source prevents dielectric damage to devices, and the decorating particles can be readily removed from the sample after examination by a mild ultrasonic rinsing treatment.

In the reverse decoration of defects by corona charging, the corona voltage polarity is selected opposite that of the decorating particles so that deposition occurs on the insulator surfaces only. A relatively large margin or halo of nondecoration around each defect forms due to ion deflection and surface current effects. Decoration with phosphor particles is readily possible by this method, but superior sensitivity and contrast result by use of carbon black suspensions.[4] This technique is not discussed here, since it does not involve fluorescence.

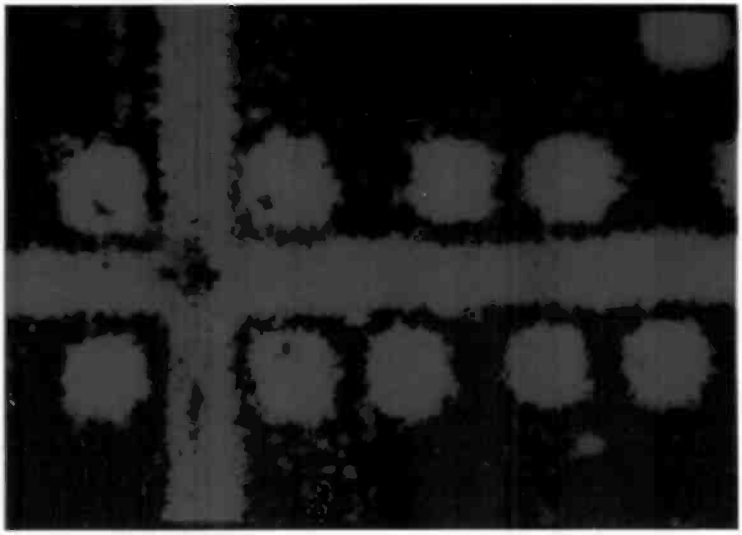

Plate 1—Red fluorescing YVO_4:Eu phosphor electrophoretically deposited on conductive areas of an IC. Width of gridline is 100 μm. (Leitz, UV; Ektachrome 160 ER-135.)

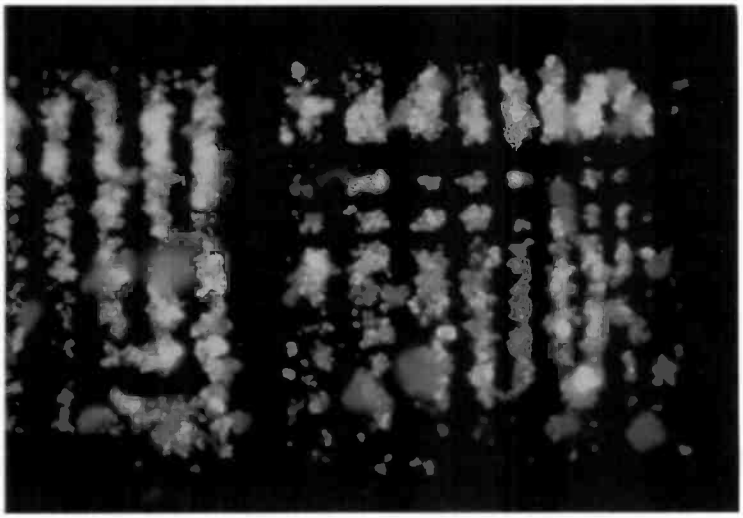

Plate 2—Mixture of red and yellow fluorescing phosphor particles electrophoretically deposited on a conductive silicon test pattern. Particles tend to become dislodged due to poor adhesion. Length of lines is 130 μm. (Leitz, UV; Ektachrome 160 ER-135).

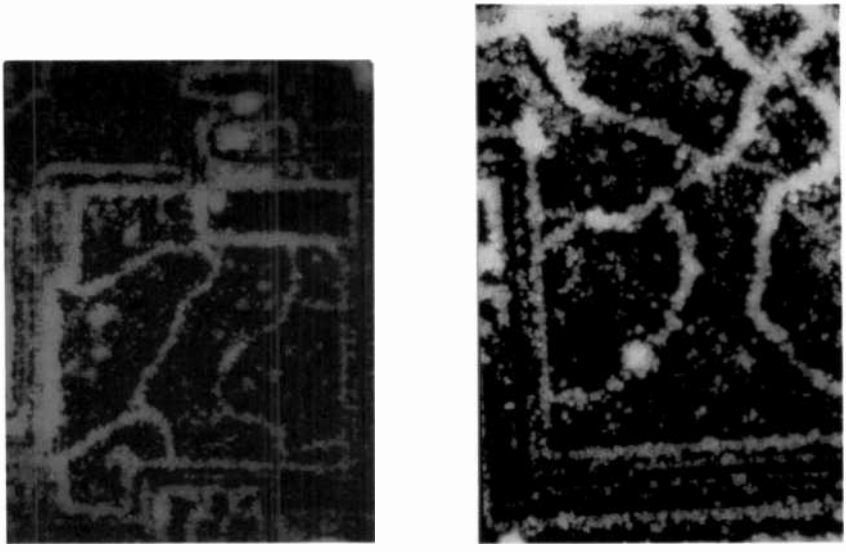

Plate 3—Cracks in a glass layer over an aluminum-metallized IC capacitor, electrophoretically decorated with yellow-green fluorescing $2ZnO \cdot SiO_2$:Mn phosphor. Length of capacitor metal area shown is 430 μm. (Leitz, UV; Ektachrome 160 ER-135).

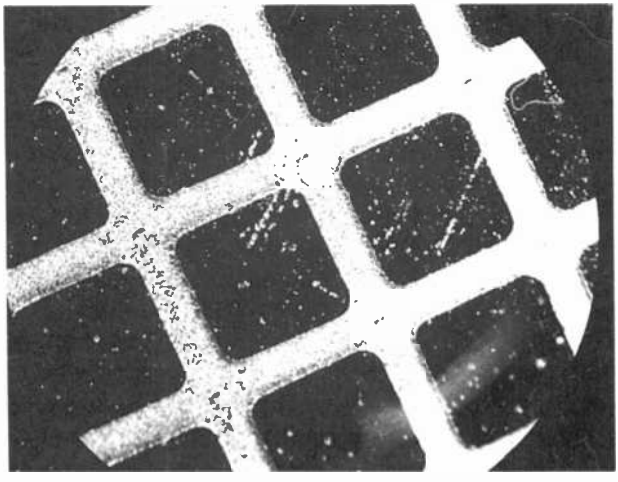

Plate 4—Electrophoretically deposited Zn,CdS : CuAl phosphor decorating pinholes in a thick oxide layer on silicon mesas. Heavily coated channels are conductive silicon regions. (Reichert, UV; 11×; Polaroid Type 57 high-speed black/white.) High-sensitivity black and white film was used here to reduce exposure time required. At low magnifications, as here, fluorescence intensity is frequently insufficient for good contrast in color photography.

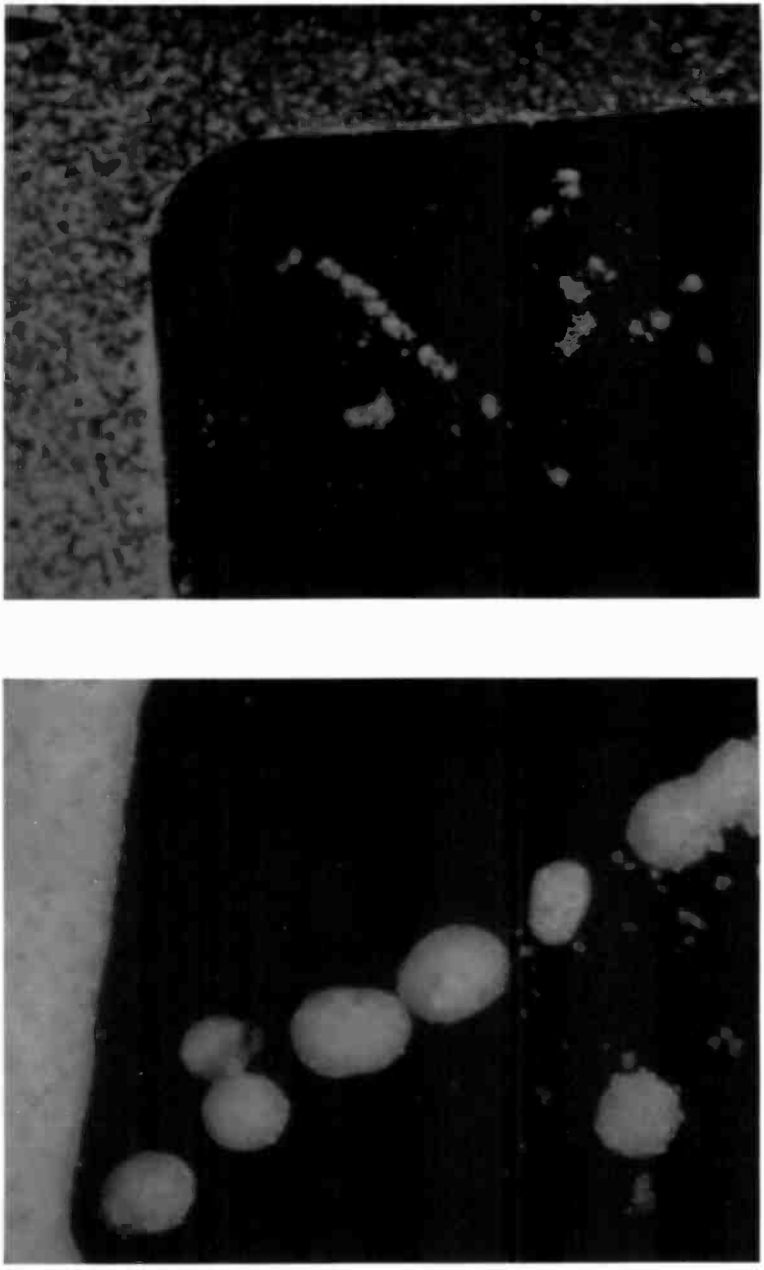

Plate 5—Enlarged areas of Plate 4. Each circular decoration spot indicates the presence of a pinhole in the insulator layer over silicon. Top photomicrograph: 63×, Bottom: 235×. (Nikon, UV; Polaroid Type 59 Polacolor ER).

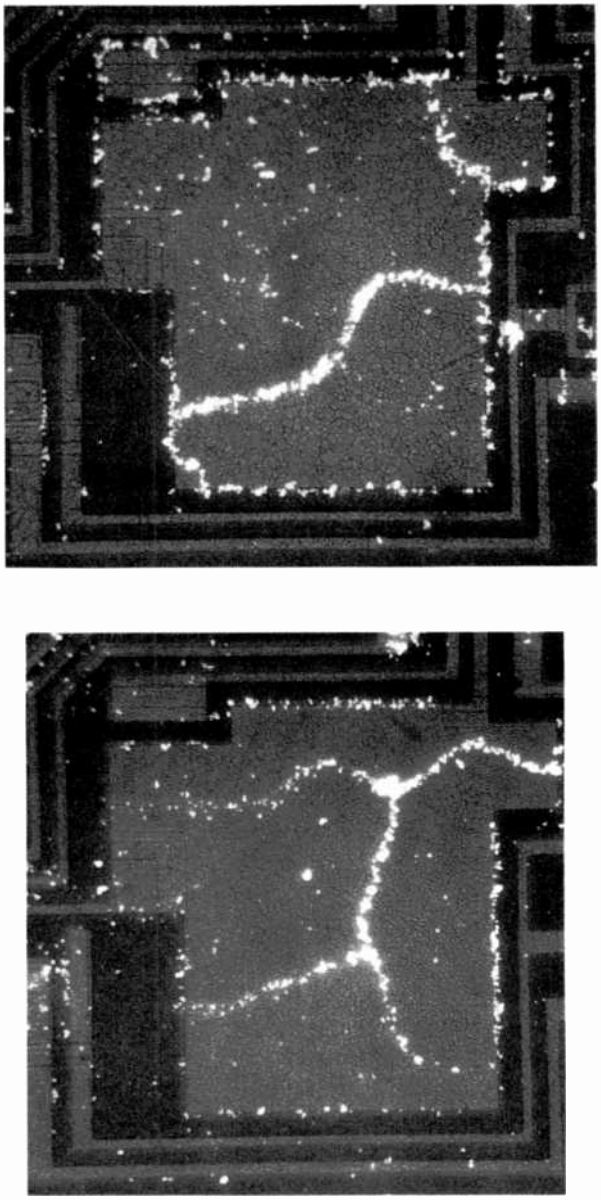

Plate 6—Electrostatically deposited green fluorescing $2ZnO \cdot SiO_2$: Mn phosphor decorating induced cracks in typical glassed aluminum-metallized IC capacitors. Black and white photos were taken for greater contrast (see caption to Plate 4). Corona charging voltage was 7000 V dc. (Reichert, UV; 128×; Polaroid Type 57 high-speed black/white.)

4. Fluorescent Tracer Techniques for Detecting Insulator Defects

The electrophoretic decoration methods described are very effective for detecting relatively large defects. However, we have recently conducted further studies to devise techniques that are both more sensitive for detecting microdefects and simpler to carry out in the laboratory. These techniques are based on selectively marking the defects with a fluorescent organic compound for examination under the fluorescence microscope. Cracks and pinholes, the usual types of structural defects in insulator coatings, form in effect microcavities with a depth up to the thickness of the layer—typically several thousand angstroms to several micrometers. Applying a fluorescing tracer solution to the sample and allowing the solution to penetrate and fill the defect cavities, followed by removal of the excess solution from the surface, can result in sharp demarcation of the defects. However, the fluorescing tracer, the solution composition, and the technique of application all must be optimized for best results.

Numerous UV-fluorescing organic chemicals,[9-11] especially dyes[20] and a few organic phosphors,[12] are available as potential candidates for our purpose. We selected several materials based on fluorescence color and intensity, solubility, chemical stability, and successful results in defect detection tests. An additional desirable requirement is intense fluorescence in solution only, but minimal fluorescence in the dry state, so that maximum contrast can be attained of the tracer solution in the defect cavities and the dried surface background. The fluorescent chemicals we have found most satisfactory are listed in Table I, together with the optimized solution systems and resulting fluorescence colors in the defect sample sites.

The simplest material to use is an organic phosphor[12] dissolved in chloroform at a concentration range of 0.02 to 0.05 wt/vol% in which the samples are dipped. This organic phosphor fluoresces very intensely green-yellow over a wide range of exciting wavelengths, but especially in the ultraviolet region and after evaporation of the solvent. Planar samples without relief structures are particularly well suited for testing with this tracer; following withdrawal from the solution and evaporation of the chloroform, the phosphor deposit on the sample surfaces can be readily removed by wiping with a dry cotton swab, leaving the fluorescing cracks and pinholes sharply contrasted against the dark background, as shown in the photomicrographs of Plates 7 and 8. We found that addition of 20 vol/vol% dimethyl sulfoxide to the chloroform solution causes this phosphor to crystallize preferentially along surface defects and pattern edges, which act as nucleation sites.

Table 1—Fluorescent Tracer Preparation for Defect Detection

Fluorescing Tracer Compound	Concentration (wt/vol%)	Solution System, Additives (vol/vol%)	Fluorescence Color in Sample Defects	Comments
Green Organic Phosphor GE 117-15-3-0P4	0.02–0.05	100 Chloroform	Intense Green-Yellow (dry)	Wipe surface after drying, simplest
	0.02–0.05	80 Chloroform 20 Dimethylsulfoxide	Intense Green-Yellow (dry)	For crystallizing in defects
Fluorescein Sodium Derivative	0.010	50 Ethanol 49 Water 0.20 Glycerol 0.050 FC-93 Surfactant (3M Co.) 0.15–0.75 KOH Solution (10%), to pH 9	Intense Green (in Solution)	Excellent for most applications
	0.010	50 Dimethylsulfoxide 40 Ethanol 9 Water 0.10 FC-93 Surfactant (3M Co.) 0.15–0.75 KOH Solution (10%) to pH 9	Intense Green (in Solution)	Superior penetration. Effective for fine cracks.
Esculin Monohydrate	0.020	50 Ethanol 49 Water 0.40 Glycerol 0.10 FC-93 Surfactant (3M Co.) 0.20–0.80 KOH Solution (10%) to pH 9	Bright Whitish-Blue (in Solution)	Excellent where blue fluorescence is preferred

	0.020	50 40 9 0.20 0.20–0.80 KOH Solution (10%) to pH 9	Dimethylsulfoxide Ethanol Water FC-93 Surfactant (3M Co.)	Strong Green-Yellow or Blue (in Solution)	Excellent and intense fluorescence. One of the best preparations for all purposes
β-Methylumbelliferone (7-hydroxy-4-methylcoumarin)	0.020	50 40 9 0.20 0.25–0.75 KOH Solution (10%) to pH 9	Dimethylsulfoxide Ethanol Water FC-93 Surfactant (3M Co.)	Bright Blue (in Solution)	Good for deep defects and etched channels
5-(p-dimethylaminobenzylidene)rhodanine	0.020	50 40 9.80 0.20	Dimethylsulfoxide Ethanol Water FC-93 Surfactant (3M Co)	Green to Blue (in Solution)	Relatively weak fluorescence. Useful for certain special applications with etched channels.

Note: When potassium hydroxide is added, the solution pH should be approximately 9, as measured by indicator tint paper. The pH should be checked and adjusted at least twice a day when the solutions are being used. Shelf life of the mixed solutions is limited; they are best prepared freshly from separately kept stock solutions.

The defects are enlarged manyfold by this decoration; this increases the detection sensitivity substantially, as seen in Plate 9.

Commercial preparations of fluorescent agents in oily penetrant liquids are used in industry for leak checking microelectronic packages and for crack testing bulk materials, such as cast iron objects.[13,22,23] However, these preparations are not well suited for microscopic-scale applications.

For other than planar samples we have selected organic tracers that fluoresce only in solution, not in the solid state. Properly formulated solutions remain liquid in the defect depressions, and hence fluoresce with good contrast against the dry and dark sample surface. Drying of a water-alcohol based solution in the defect sites can be prevented by the addition of glycerol, a hygroscopic and nonvolatile liquid. An adequate but minimal amount of glycerol must be incorporated to facilitate solution draining from the sample surface. The concentration must be controlled to achieve optimal effectiveness. Addition of a surfactant that does not impair the fluorescence enhances penetration into defect recesses, such as fine microcracks, and promotes subsequent draining of the excess solution. We have optimized a preparation containing 0.006 to 0.012 wt/vol% fluorescein sodium derivative, which fluoresces intensely green in alkaline solution under blue-violet light (Table 1). Several examples of samples tested with fluorescein solution are shown in Plates 10–13.

Bright whitish-blue fluorescing esculin monohydrate may be used for samples where a blue fluorescence is desirable. The alkaline alcoholic solution systems defined in Table 1 have given good results. Demarcated pinholes in an etched glass layer are shown in Plate 14.

We have developed a novel solution system for applications to samples with deep defects and thick coatings (such as glass enamels), and for use with channel-etched samples (described below). This system is based on dimethyl sulfoxide, a liquid with very low volatility, low viscosity, strong solvent capabilities, and good miscibility characteristics with water and organic solvents. Ethanol and surfactant are incorporated to enhance wetting and penetration; water is added to allow optimization of the pH (usually in the range of 9–10) at the time of application. Fluorescent tracer solution remains in the deep defects for a long time, while the surface dries clean without the usual sticky residues that tend to be left from solutions containing nonvolatile and viscous glycerol. Excellent results have also been obtained with esculin monohydrate in this solvent system, making this one of the best of these tracer solutions. Good results have also been achieved with bright blue fluorescing β-methylumbelliferone at concentrations of 0.01 to 0.03 wt/vol% as noted in Table 1 and exemplified in the photomicrographs of Plate 15.

Another tracer compound we have used successfully, especially with the dimethylsulfoxide-based solution system, is 5-(p-dimethylaminobenzylidene)rhodanine; its solutions in defect sites fluoresce yellow-green, which may change to whitish-blue. Examples of photomicrographs are shown in Plates 16 and 17.

Other positive compounds we tested include yellow to green fluorescing acridine orange, yellow fluorescing eosine-Y, and blue fluorescing H_2SO_4-containing solutions of quinine monohydrate. However, the first compound is a cancer-suspect agent, the second tends to crystallize, and the third fades rapidly and irreversibly in ultraviolet light. Several other compounds do not fluoresce with sufficient intensity, or have other shortcomings.

The procedure for demarcating defects by any of the solutions is fast and simple. The dry sample is submerged in the working solution for 5 to 10 minutes. The excess solution is then removed from the surface by draining edgewise on lint-free filter paper (e.g., Whatman No. 52). Examination under the fluorescence microscope is preferably done as soon as the sample surface is semi-dry. Alternatively, a thin microscope cover glass can be pressed onto the drained sample. This procedure causes the sample surface to dry slowly from the edges, allowing the defects to remain filled with solution for a prolonged period of time. Microscopic observation of the sample surface through the fluorescing liquid can also give interesting effects with some types of structures. Samples should be stored in a humidity chamber (at about 85% relative humidity) to avoid drying, except for samples tested with the organophosphor.

An interesting novel technique for increasing the defect detection limit is to selectively etch the substrate in the exposed insulator defect area to some depth to produce a channel underneath the insulator coating. Exposure of the rinsed and dried sample to the fluorescing tracer solutions fills these voids, thereby vastly increasing the detectability, as seen in the photographs of glass films over aluminum-metallized devices (Plates 12, 16 and 17). The visibility of a crack 1000 Å wide in the insulator can be increased by a factor of 10, for example, to a width of 1.0 μm, by selective isotropic etching 4500-Å deep into the substrate. Pinholes result in correspondingly enlarged circular spots.

The microscope used for examining all samples was an Optiphot (Nikon Model XF-EF) with the Episcopic-Fluorescence (EF) attachment, which incorporates an Osram HBO 50W high-pressure mercury-vapor lamp as the radiation source.[14] Light from the source is directed through an excitation filter, which passes radiation below a specified wavelength through the objective to the sample.[15, 16] The light from the sample consists of reflected source light and emitted fluorescence

light, but most of the excitation light is diverted by a dichroic mirror in the excitation filter holder. The violet excitation filter (405 nm) with the 470 nm viewing filter was used in most cases, since it produced more intense fluorescence than the ultraviolet excitation filter.* Color photomicrographs (Plates 18 and 19) were taken at magnification of up to 535X with Polaroid cassette Land film, types 58 (Polacolor 2) and 59 (Polacolor ER).

Samples with less intense fluorescence were photographed through a Leitz Orthoplan research microscope using a Ploemopak multi-wavelength fluorescence illuminator with an ultra-high-pressure mercury lamp as the radiation source.[17] Automatic color photomicrography was carried out with a Leitz Vario Orthomat system[17] using high-speed 35 mm Kodak Ektachrome 160 ER-135 reversal film, which resulted in greatly enhanced sensitivity.

Excellent results have been achieved by these simple but effective techniques which allow testing of entire device wafers or other substrates, since no bias needs to be applied.

5. Conclusions

We have shown that certain pH-sensitive UV-fluorescent indicator dyes are a very effective and convenient tool for studying corrosion phenomena in semiconductor devices. Changes in the pH can be readily monitored under dynamic conditions and be made visible for microscopic inspection.

Structural defects in insulator coatings on semiconductive or conductive substrates can be decorated for microscopic examination by electrophoretic or electrostatic deposition of negatively-charged UV phosphor particles suspended in dielectric liquid media. However, the rather large size of the particles required for optimal fluorescence restricts decoration to relatively large defects, limiting the scope of this interesting process to selected applications.

Microdefects, such as fine cracks, pinholes, cavities, and depressions in dielectric films are best demarcated with intensely UV fluorescing organic tracer compounds dissolved in optimized solvent systems. This novel method is fast, simple, effective, and independent of the electrical conductivity of the substrate. Several especially suitable organic compounds, including an organic phosphor, have been identified for this purpose. The exact compositions of optimized tracer solutions have been presented.

* (365 nm); it was used with the 470 μm filter for work with the organic phosphor.

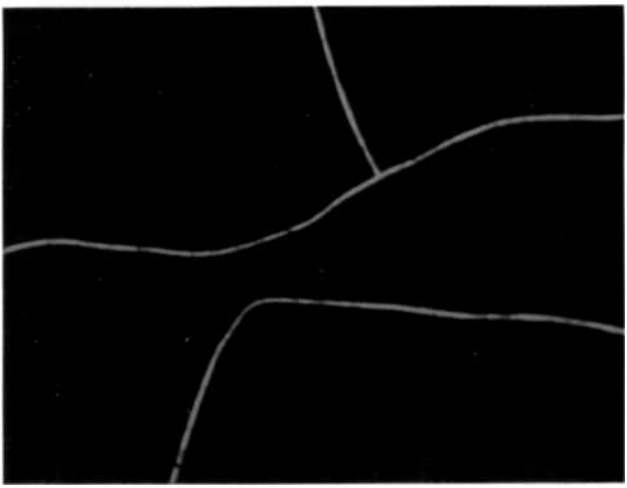

Plate 7—Cracks in a 1-μm thick glass layer on aluminum, delineated with a bluish fluorescing organic phosphor in chloroform. Surface of dry sample was wiped to eliminate background fluorescence. (Nikon, UV; 186×; Polaroid Type 59 Polacolor ER).

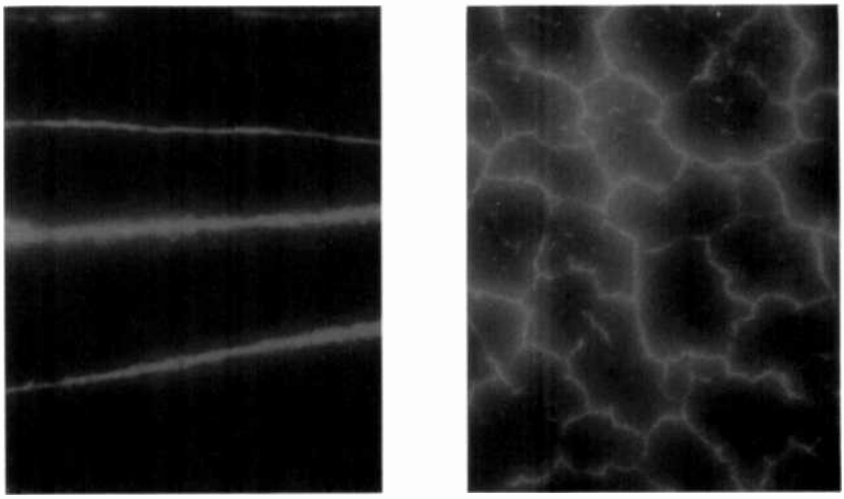

Plate 8—Organic phosphor in chloroform applied to a 180-μm thick glass enamel coating on a steel substrate. Induced mechanical cracks (left) and thermal stress cracks (right) that are otherwise invisible are demarcated clearly by the tracer. (Nikon, UV; 41×; Polaroid Type 58 Polacolor 2 and 59 Polacolor ER).

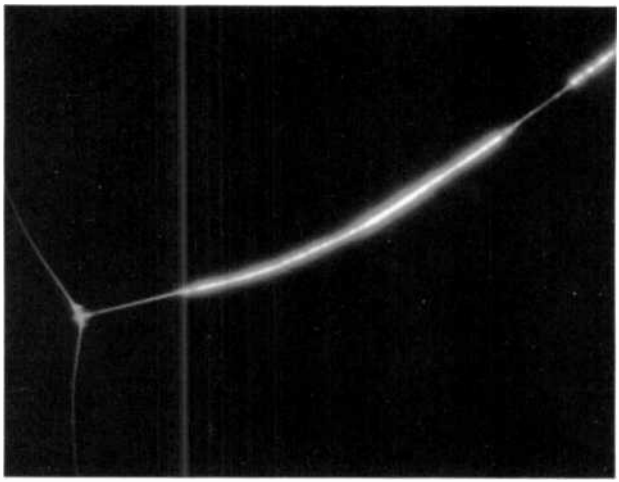

Plate 9—Fine microcrack in a glass film decorated by crystallized organic phosphor from a solution in dimethylsulfoxide and chloroform. (Nikon, UV; 380×; Polaroid Type 58 Polacolor 2).

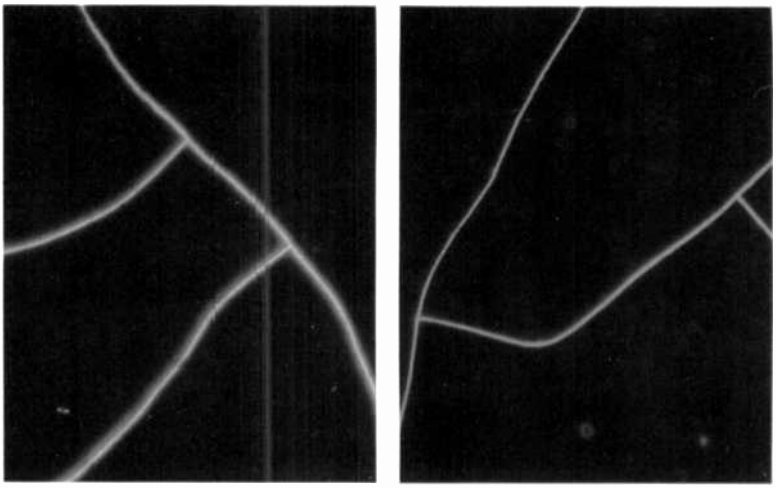

Plate 10—Cracks in 1-μm thick glass films on aluminum, demarcated with green fluorescing solution of fluorescein. (Nikon, violet-blue exciter filter, 295×; Polaroid Type 58 Polacolor ER).

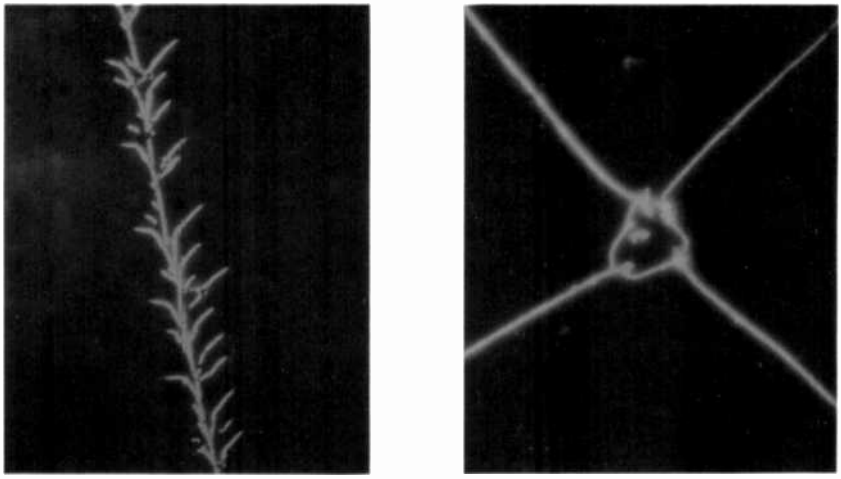

Plate 11—Same as in Plate 10, but showing different types of cracks. (Nikon, 295×; Polaroid Type 58 Polacolor 2).

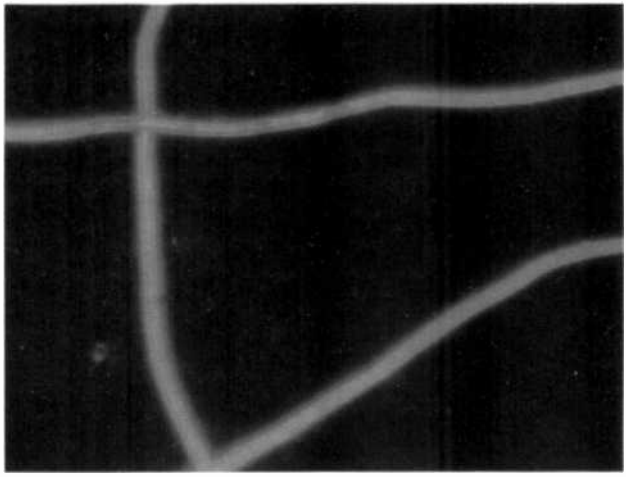

Plate 12—Same is in Plate 10, but showing defect-enlargement effect after selective etching of underlying aluminum to form a channel. (Nikon, 385×; Polaroid Type 58 Polacolor 2).

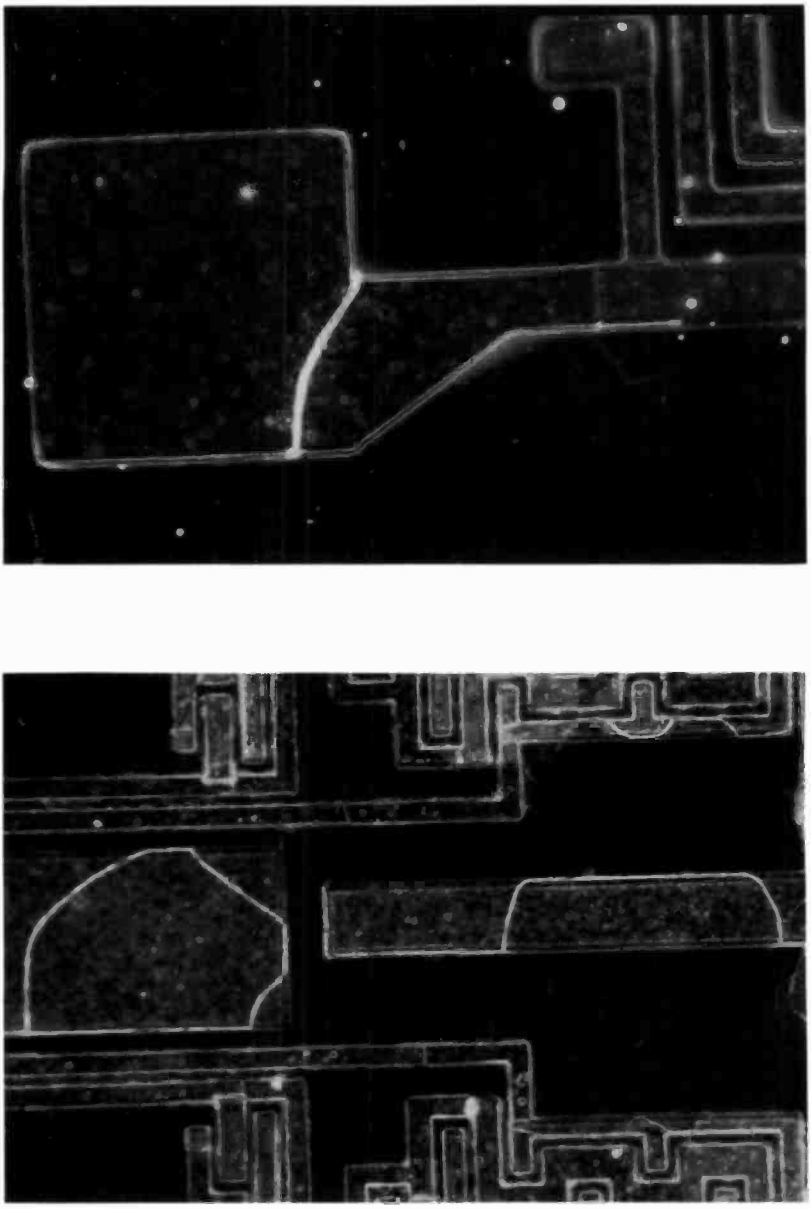

Plate 13—Demarcation of microcracks in a 1-μm thick glass layer over an aluminum-metallized IC using fluorescein solution. Heavy cracks with intense green fluorescence are readily visible over the metal areas; some very fine and narrow microcracks can be seen in the dark areas of glass over thermally-grown SiO_2 on silicon. Square metal area measures 100-μm. (Leitz, Ektachrome 160 ER-135.)

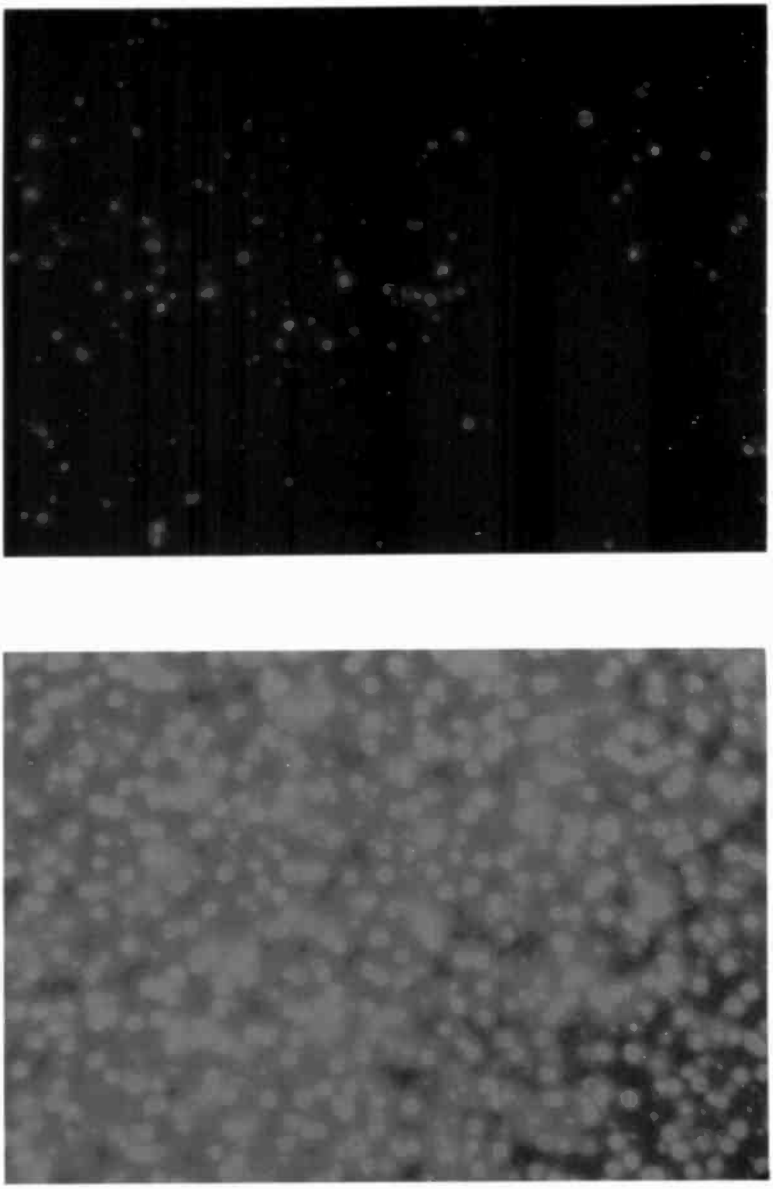

Plate 14—Pinholes in a thin glass layer demarcated with esculin monohydrate solution. The glass, a LPCVD PSG film on aluminum, is thinned by 70% of its original thickness of 8000 Å to test for latent pinholes. (Nikon, violet-blue exciter filter, 470×; Polaroid Type 59 Polacolor ER). The lower photomicrograph shows a similar sample after an additional etching step in aluminum etchant to form a cavity beneath each pinhole (camera, filter and film same as above).

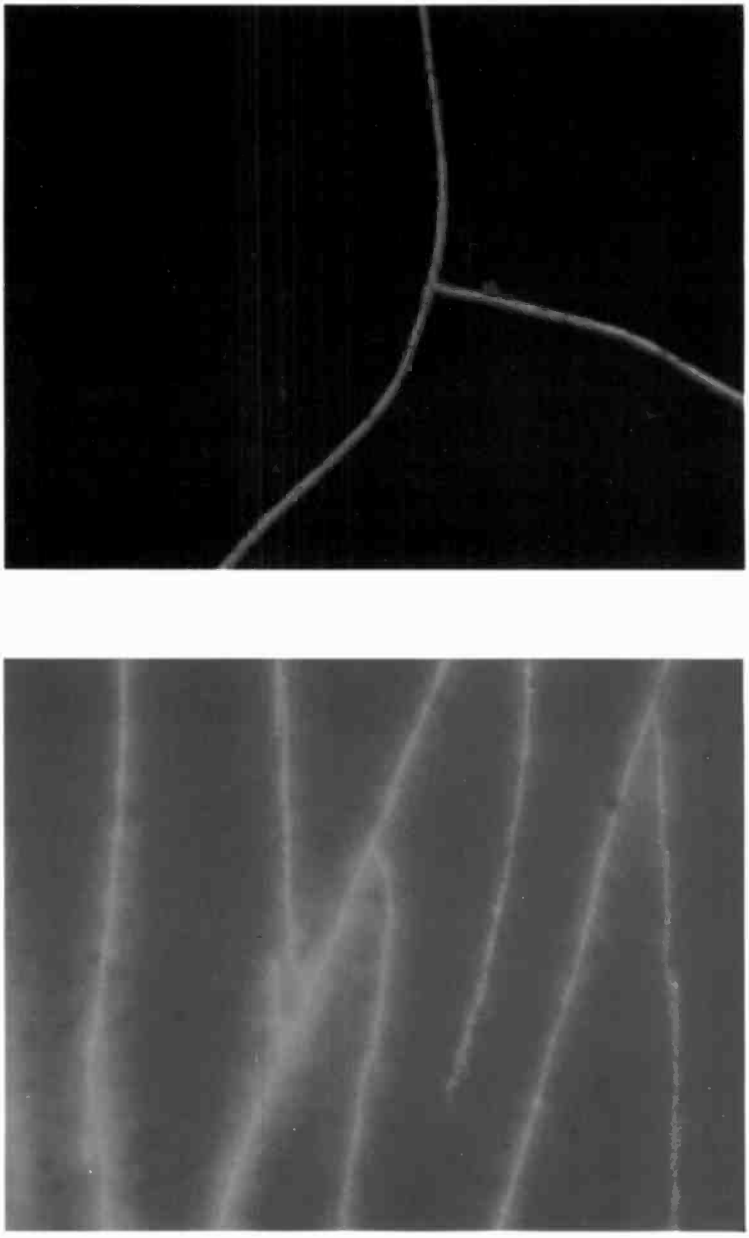

Plate 15—Demarcation of cracks in a 1-μm thick (top, 460×) and a 180-μm thick (bottom, 62×) glass layer using blue-fluorescing β-methylumbelliferone. (Nikon, violet-blue excitation; Polaroid Type 59 Polacolor ER).

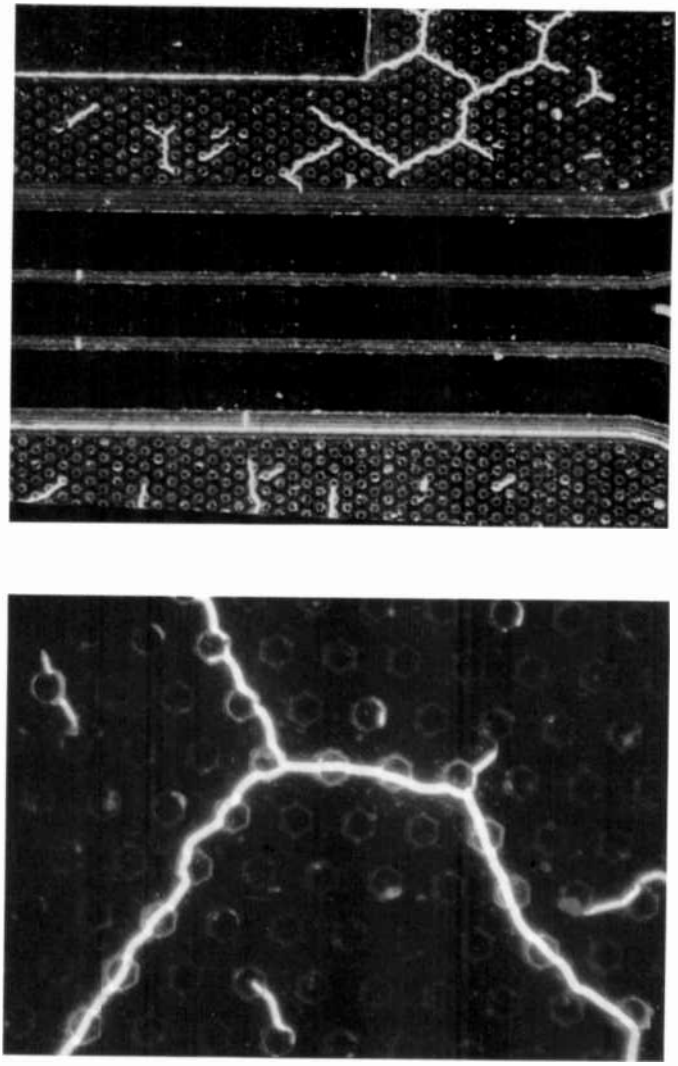

Plate 16—Thermally-induced cracks in the glass coating of an aluminum-metallized MOS power device array. The aluminum was selectively etched to produce a channel beneath the glass. 5-(p-dimethylaminobenzylidene)rhodanine/dimethylsulfoxide-ethanol solution then filled the channel, increasing the detection sensitivity for microcracks greatly. Maximum diameter of the hexagonal structures, illuminated by fluorescence, is 21 μm. (Top: Leitz, Ektachrome 160 ER 135; glass cracks are yellow, tan lines indicate steep steps at the mesa edges. Bottom: Nikon, violet-blue excitation, Polaroid Type 58 Polacolor 2; enlarged section of crack area, 220×.) Differences in color result from different modes of excitation and optical filters.

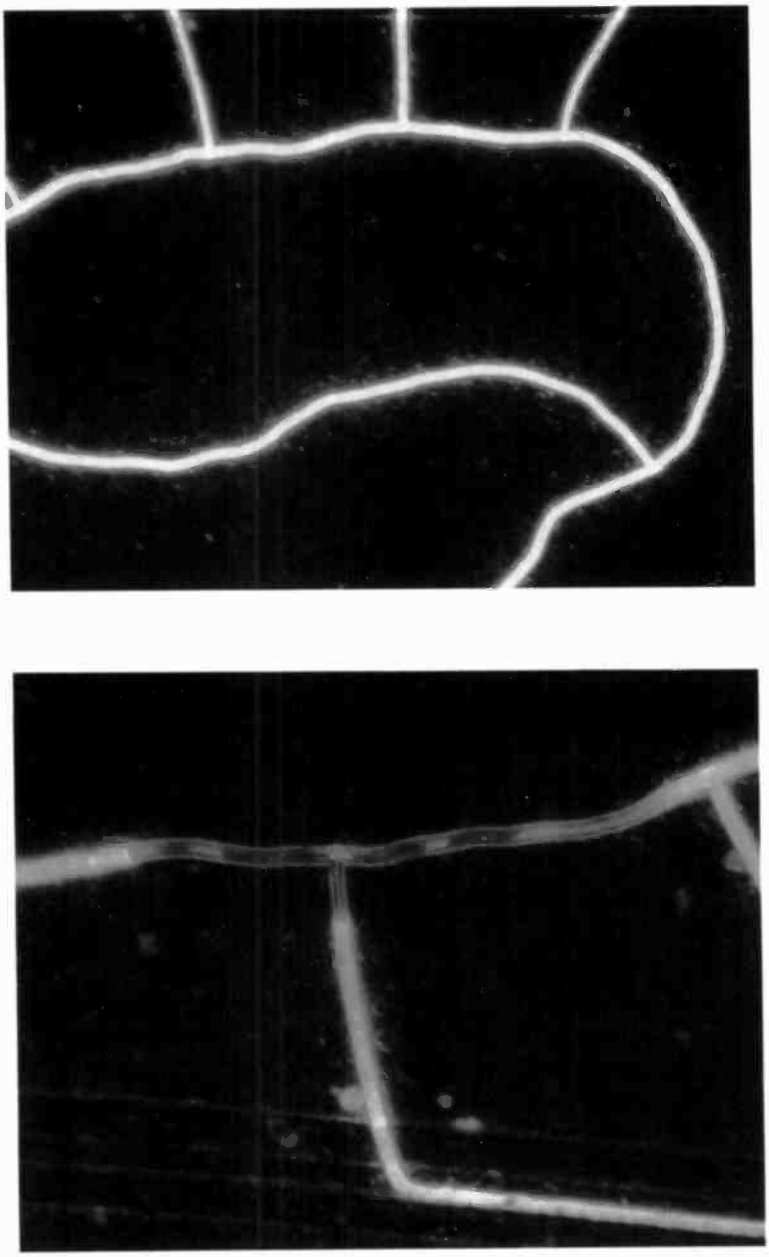

Plate 17—Same as Plate 16 (bottom), but showing filled channels in a planar area of the device. Close up (bottom) shows a partially dried up portion of the 4 to 6-μm wide channel. A fine glass crack is visible in the center of the channel. Top: 230× bottom: 460×.

Three techniques of application have been described: (1) immersion of the sample in the solution, followed by draining and partial drying of the surface and inspection under a UV fluorescence microscope; (2) selective partial etching of the substrate to create a channel for subsequent filling with the fluorescent solution, thereby greatly increasing the detection sensitivity; and (3) crystallization of phosphor around the defect sites resulting in easily visible decoration areas when viewed in ultraviolet light under the microscope. These techniques offer a new dimension for device defect analysis and structural defect detection methodology in general. Although we have applied this method specifically to dielectric films, it can be extended to practically any type of film, or bulk material with depressed defect sites.

Acknowledgments

The section on corrosion phenomena with fluorescent indicators was abstracted from research work originally published in collaboration with Lawrence K. White and Cheryl A. Deckert, as indicated in the references.

The new work on organic fluorescent tracer techniques for defect detection was carried out by Richard E. Berger of our laboratory. We wish to thank also Lawrence K. White for providing important information on fluorescence microscopy techniques, Reinhard Enders of Leitz, Inc., for making available to us all of the Leitz fluorescence photomicrographic equipment, and Jeffrey K. Kern for helpful advice on color photographic processing.

References:

[1] W. Kern, "Characterization of Localized Structural Defects in Dielectric Films," *RCA Rev.*, **34**, No. 4, 655 (1973); also: "Characterization of Localized Defects in Dielectric Films for Electron Devices," *Solid State Technol.*, **17**, No. 3, p. 35; No. 4, p. 78 (1974).
[2] W. Kern and R. B. Comizzoli, "Techniques for Measuring the Integrity of Passivation Overcoats on Integrated Circuits," NBS Special Publication *400-31*, March 1977.
[3] W. Kern and R. B. Comizzoli, "New Methods for Detecting Structural Defects in Glass Passivation Films," *J. Vac. Sci. Technol.*, **14**, No. 1, p. 32 (1977).
[4] R. B. Comizzoli, "Nondestructive, Reverse Decoration of Defects in IC Passivation Overcoats", *J. Electrochem. Soc.*, **124**, p. 1087 (1977).
[5] G. L. Schnable, R. B. Comizzoli, W. Kern, and L. K. White, "A Survey of Corrosion Failure Mechanisms in Microelectronic Devices", *RCA Rev.*, **40**, No. 4, p. 416 (1979).
[6] C. A. Deckert, R. B. Comizzoli, and G. L. Schnable, "Method for Inspecting Electrical Devices," U.S. Patent 4,237,379, Dec. 2, 1980.
[7] L. K. White, R. B. Comizzoli, C. A. Deckert, and G. L. Schnable, "The Detection of Corrosion Phenomena with pH-Sensitive Dyes on Aluminum- and Gold-Metallized IC Devices," *J. Electrochem. Soc.*, **128**, No. 5, p. 953 (1981).
[8] L. K. White, R. B. Comizzoli, and G. L. Schnable, "Method of Detecting a Cathodic Corrosion Site on a Metallized Substrate," U.S. Patent 4,278,508, July 14, 1981.
[9] J. DeMent, *Fluorescent Chemicals and Their Applications*, Chemical Publishing Co., Inc., Brooklyn, NY (1942).

[10] P. Pringsheim and M. Vogel, *Luminescence of Liquids and Solids*, Interscience Publishers, Inc., New York, NY (1943).
[11] G. G. Guilbault, *Practical Fluorescence*, Marcel Dekker, Inc , NY (1981).
[12] "Organic Phosphors", Product Data Sheet 7750-Z, July 1, 1978, General Electric Company, Cleveland, Ohio, 44112.
[13] For example, ZA-43 Zyglo Kit, Magnaflux Corporation, Testing Systems, Chicago, Il. 60656.
[14] "Episcopic-Fluorescence Attachment EF/EFA", Instructions, Nikon, Nippon Kogaku K.K., Tokyo, Japan.
[15] G. E. Schlueter, "Fluorescence Microscopy—Instrumentation and Techniques," *American Laboratory*, **5** (4), p. 47 (1973).
[16] R. K. Vitek and D. N. Schowalter, "Ultraviolet Photography in the Laboratory," *American Laboratory*, **13** (7), p. 43 (1981).
[17] "Leitz Fluorescence Microscopes"; "Fluorescence Microscopy"; "Leitz Vario Orthomat"; E. Leitz, Inc. Rockleigh, NJ 07647.
[18] J. I. Siegel, "Fluorescence Microscopy," *American Laboratory*, **14** (4), p. 65 (1982).
[19] P. Johnson, "Instant Photomicrography," *Functional Photography*, **16** (5), p. 25 (Sept./Oct. 1981).
[20] F. F. Hartline, "Biological Applications for Voltage Sensitive Dyes", *Science*, **203**, 992, March 9, 1979.
[21] J. R. Alburger, "Electrically Responsive Color-Forming Method of Nondestructive Testing," U.S. Patent 3,530,045, Sept. 22, 1970.
[22] J. M. Portaz, *Evaluation of Microencapsulated Penetrant Inspection*, AFWAL-TR-80-4056, 1980, A. F. Syst. Command, WPABF, Materials Laboratory.
[23] L. Ya. Malkes, T. V. Ershova, V. M. Usenko, V. E. Moskalenko, A. D. Nikolaichuk, and L. I. Sukiasova, "Revealing Surface Defects on Cast Steel Parts With The Aid of Type "LZh" Fluorescent Liquids," *Sov. J. Nondestr. Test.* **12**, No. 3, 318, May–June 1976.
[24] R. B. Comizzoli, L. K. White, W. Kern, and G. L. Schnable, *Corrosion of Metal Films with Defective Surface Protection Layers*, RADC-TR-80-236, Final Technical Report, July 1980, Rome Air Development Center, Griffiss Air Force Base, NY 13441.
[25] R. B. Comizzoli, L. K. White, W. Kern, G. L. Schnable, D. A. Peters, C. E. Tracy, and R. D. Vibronek, "Corrosion of Aluminum IC Metallization With Defective Surface Passivation Layer", *18th Annual Proc. Reliability Physics*, p. 282 (1980).
[26] W. Kern, R. B. Comizzoli and G. L. Schnable, "Fluorescence Techniques Allow Defect Study in Microelectronics," *Industrial Research and Development*, **24**, No. 5, p. 151, (May 1982).
[27] W. Kern, "Fluorescent Tracers Simplify Detection of Microdefects", *Industrial Research and Development*, **24**, No. 6, p. 131 (June 1982).

Simplified Analysis of Kinescope Electron Guns

D. A. de Wolf*
RCA Laboratories, Princeton, NJ 08540

Abstract—The numerical integration of trajectory equations to simulate electron beams in kinescope electron guns is complicated because (a) the interior electrostatic fields cannot be computed analytically and (b) space-charge forces couple the trajectory equations to the Poisson equation nonlinearly. Solution by digital computer requires iteration of trajectories and storage of large arrays of potentials, fields, and current densities. Even exploratory analysis can be costly. A simplified analysis is presented here that permits speedy, low-cost evaluation of axially symmetric electron guns, albeit at a loss of high accuracy. The analysis utilizes approximations to the lens fields and to the Coulomb forces in various gun regions. The approximations are especially good in the drift and main-lens regions.

1. Introduction

The design of kinescope electron guns has been greatly enhanced by the ability to simulate electron trajectories numerically with digital computers.[1,2] To do so, one needs to solve the usual[3] second-order differential equations of the trajectory coordinates as functions of time or of the axial coordinate. The differential equations involve the potentials and fields of the regions through which the electrons pass. In all but the most elementary situations, even with known fields and potentials everywhere, it is necessary to integrate the trajectory equations numerically. The techniques are standard[4,5] and pose no particular problem.

However, two factors greatly complicate the numerical integration

*Presently at Virginia Polytechnic Institute and State University, Dept. of Electrical Engineering, Blacksburg, VA 24061.

of trajectory equations. First, if space charge (the mutual Coulomb forces between electrons) is ignored, then the potential is obtained from the Laplace equation with appropriate boundary conditions.[3,6] Numerical methods are nearly always needed. Relaxation methods[7,8] require calculation of a large two- or three-dimensional array of fields, and integral-equation methods[5] either require this also or necessitate repeated evaluation of potential and fields by a time-consuming numerical integration at each trajectory point.

In the second place, space charge renders the differential equations, together with the needed Poisson equation, nonlinear because the fields depend upon (to be calculated) trajectory coordinates. The numerical work is greatly increased by the necessity of an iteration procedure[8,9] through enough cycles so that the fields calculated from the $(n-1)$st trajectory coordinates do not bring about appreciable modifications in the nth trajectory coordinates.

In practice, kinescope electron guns are manufactured from more-or-less standard parts, and one can separate a gun into three regions: a beamforming region (BFR) in which several round-aperture lenses extract and concentrate a beam of electrons emitted from a cathode; a main-lens region (MLR) in which the diverging beam is focussed towards a screen location; and a drift region (DR) in which the redirected electrons move only under space-charge and deflection forces to a relatively distant screen.

Alig[10] has recently reviewed these and related matters. A characteristic sketch is shown in Fig. 1 to clarify the separation. The main lens usually consists of several metallic cylinders of equal radius placed coaxially in tandem to produce a compound-cylinder lens with small gaps between the components.

For much design work with kinescope guns and certainly for the initial determination of operational parameters such as focus voltage, drive-voltage versus current characteristics, etc., it seems unnecessary to demand high accuracy of the trajectory simulation. The purpose of this paper is to present analytical approximations to potentials and fields everywhere that vastly reduce the numerical work to merely the one-time numerical integration of a set of second-order ordinary differential equations with known coefficients under appropriate initial conditions.

A full numerical program, ELOP,[8] has been utilized to provide a standard calculation to which the approximations of this work can be compared. Certain assumptions regarding the fitting of a beam current density to sample trajectory coordinates have been made in ELOP; similar ones have been utilized in this work to make a comparison feasible. The approach is four-fold:

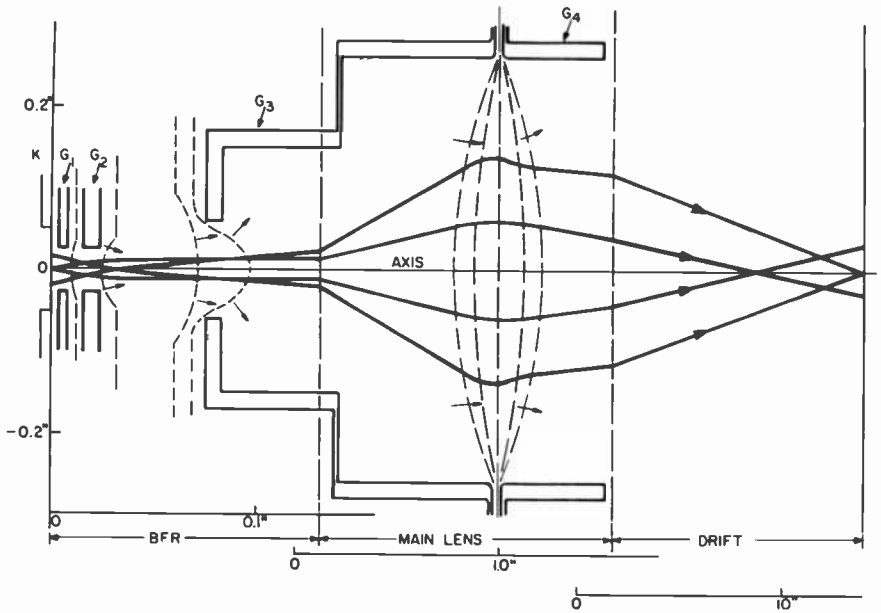

Fig. 1—Sketch of a kinescope emphasizing the electron optics aspects (from Alig, Ref. [10]). Note that G3 and G4 have effectively the same radius with respect to the lens formed by both electrodes. The various regions are drawn to different scales. Some equipotential lines (dashed) and some key trajectories (heavy lines) are depicted.

(1) Replacement of the space-charge fields by an equivalent transverse field. Neglect of longitudinal fields is serious only close to the cathode in the BFR [see point (4) below], and it eliminates the need for iteration.

(2) Approximation of potentials and fields inside the main lens by a two-term analytical approximation based on an extension of Bertram's approximation[11] for axially symmetric cylinders of equal radius.

(3) Approximation of potential and fields inside the BFR by an extension of an analytical procedure due to Regenstreif[12] for compound coaxial aperture lenses.

(4) An analytical determination of the emitted current profile and the concomitant analytical calculation of electron trajectories with Child's law under the space-charge limited conditions close to the cathode.

Because the complexity of these approximations is greatest nearest the cathode, and least in the DR, we shall examine them in reverse order of the actual cathode-to-screen calculation. Thus, we start with the DR, where there are only space-charge and deflection fields; we

then discuss the MLR, where space-charge fields are small but where there are lens forces; and we end with BFR where both forces are strong. An estimate of current density also is obtained from the BFR parameters.

2. The Transverse Space-Charge Approximation in the Drift Region.

The electron beam enters the drift region from the MLR and may undergo deflection forces to focus upon a spot that is not at the center of the screen. Whether or not the beam is deflected, however, the only electrostatic forces in the DR are due to space charge. Each electron can be considered to be in a central-force field due to the collective effect of all other electrons.[13] This field is

$$E(R) = \frac{-e}{4\pi\epsilon_0} \int d^3R_1 n(\mathbf{R}_1) \frac{(\mathbf{R} - \mathbf{R}_1)}{|\mathbf{R} - \mathbf{R}_1|^3}, \qquad [1]$$

where $n(\mathbf{R}_1)$ is the number density of electrons at $\mathbf{R}_1$, e is the electron charge, and ϵ_0 is the vacuum dielectric permittivity. Consider a reference trajectory in the beam, e.g., a central trajectory. It has a longitudinal coordinate ζ_1. All other electrons can then be characterized by the locally orthogonal coordinate system $\mathbf{R}_1 = (\boldsymbol{\rho}_1, \zeta_1)$ where $\boldsymbol{\rho}_1$ has two mutually orthogonal components that need not be specified further.

Typical electron beams in the drift region have a density $n(\boldsymbol{\rho}_1, \zeta_1)$ that varies slowly with ζ_1. Characteristically, there will not be much change in $n(\boldsymbol{\rho}, \zeta_1)$ for a length of several radii of the beam in the longitudinal direction. It is not difficult to perform the $d\zeta_1$ integration in Eq. [1] under the approximation that $n(\mathbf{R}_1)$ does not depend upon ζ_1, and that there is no curvature locally over several beam radii. We then obtain

$$E(\boldsymbol{\rho}, \zeta) = -\frac{e}{2\pi\epsilon_0} \int d^2\rho_1 n(\boldsymbol{\rho}_1, \zeta) \frac{(\boldsymbol{\rho} - \boldsymbol{\rho}_1)}{|\boldsymbol{\rho} - \boldsymbol{\rho}_1|^2}. \qquad [2]$$

The same result can be obtained by applying Gauss's law to a thin pillbox perpendicular to the reference trajectory. The two surface forces on the top and bottom of the pillbox almost cancel each other, and in the approximation they are consequently neglected. The remaining terms can be shown to lead to Eq. [2], which obviously results from ignoring the longitudinal space-charge forces. The result, Eq. [2] is much more advantageous in use than Eq. [1] not only because it represents a two-dimensional integral (instead of a three-dimensional

one) but especially because $E(\mathbf{R})$ depends only on values of $n(\mathbf{R}_1)$ with $\zeta_1 \leq \zeta$. This crucial fact eliminates the nonlinearity, hence also the need for an iterative numerical procedure. The remaining numerical procedure then consists, in the absence of deflection, of solving the equations of motion which we give in nonrelativistic form in the standard cylindrical coordinate system,[14]

$$\mathbf{r}'' = \frac{(1 + \mathbf{r}'^2)}{2\Phi(\mathbf{r}, z)} [\mathbf{E}_r(\mathbf{r}, z) - \mathbf{r}' E_z(\mathbf{r}, z)]. \qquad [3]$$

Here, $\mathbf{E}_r$ and E_z are the three mutually perpendicular components of the field given in Eq. [2] [and $\mathbf{r}$ is a vectorial notation for the x and y components].

It is obviously necessary to discretize the beam into a number of beamlets. Then, Eq. [2] becomes

$$E(\mathbf{R}) = \frac{e}{2\pi\epsilon_0} \sum_m \int_{S_m} d^2\rho_1 n(\rho_1, \zeta) \frac{(\rho - \rho_1)}{|\rho - \rho|^2}, \qquad [4]$$

where S_m is the cross-sectional area of the mth beamlet. The beamlet is represented by one trajectory $\mathbf{r}_m(z)$ which is governed by Eq. [3]. The remaining problem is to choose the areas S_m conveniently in shape and size. Actually, a much more important problem arises here: that of beam representation. Quite in general, the number density $n(\rho_1, \zeta)$ is itself a two-dimensional integral over velocities (or momenta p_1) in the z plane characterized by ζ (the variation of ζ across the beam in a z plane is ignored)

$$n(\rho_1, \zeta) = \int d^2p_1 f(\rho_1, \mathbf{p}_1; \zeta). \qquad [5]$$

Hence Eq. [2] is actually a four-dimensional integral over a phase-space density f, and discretization should occur in all four dimensions. In this work we assume that the discretization in momentum has already been chosen prior to the DR; this is discussed later. It is by no means a trivial point because beam reconstruction at the screen is very difficult for deflected beams, even when all chosen trajectories are simulated accurately. However, we will restrict ourselves largely to rotationally symmetric beams (i.e., without deflection) in which case the momentum discretization is less of a problem.

A square mesh with spacing h is convenient for reducing Eq. [4] under the assumption that $n(\rho, \zeta)$ of the meshblock characterized by its center at $\rho_{mn} = (x_m, y_n)$ is constant. This approximation determines the magnitude of h for desired accuracy. The resulting integral in Eq.

[4] over squares can be performed and it gives

$$\mathbf{E}(\mathbf{R}) = -\frac{e}{2\pi\epsilon_0}\sum_{m,n} n(\rho_{mn}, \zeta)\mathbf{G}^{(mn)}, \quad \text{with}$$

$$G_x^{(mn)} = \frac{1}{2}\, t_f \ln[(t_f^2 + s_f^2)/(t_f^2 + s_i^2)]$$

$$-\frac{1}{2}\, t_i \ln[(t_i^2 + s_f^2)/(t_i^2 + s_i^2)] \qquad [6a]$$

$$+ s_f[A(t_f/s_f) - A(t_i/s_f)]$$

$$- s_i[A(t_f/s_i) - A(t_i/s_i)],$$

where $A(t/s)$ is an abbreviation for the arctangent of t/s, and the arguments of the functions in Eq. [6a] are defined by

$$\begin{aligned} s_f &= (x - x_m) + h/2, \qquad t_f = (y - y_n) + h/2 \\ s_i &= (x - x_m) - h/2, \qquad t_i = (y - y_n) - h/2 \end{aligned} \qquad [6b]$$

A similar expression holds for the y component of $\mathbf{G}^{(mn)}$. These expressions can be greatly simplified if one is willing to allow for some inaccuracy in the vicinity of the edges of the square

$$\mathbf{G}^{(mn)} \sim \frac{(\rho - \rho_{mn})}{|\rho - \rho_{mn}|^2 + h^2/\pi}. \qquad [7]$$

The error can be shown to become negligible as $h \to 0$. In practice, even for a relatively coarse mesh, the error can be kept small because most of the contribution to $E(R)$ in Eq. [4] comes from nonneighboring meshblocks. Admittedly, there may be z planes in which $n(\rho_{mn}, \zeta)$ is very granular in distribution, but even then the forces are most important where Eq. [7] is a good approximation to Eq. [6].

In the case of a rotationally symmetric beam, we may choose $\zeta = z$, and $\rho = r$, and Eq. [2] can then be reduced to

$$E(R) = \frac{e}{\epsilon_0 r_0}\int_0^r dr_1 r_1 n(r_1, z), \qquad [8]$$

where the transverse space-charge field E is now directed radially outwards and is denoted as a scalar in Eq. [8]. A discretization of Eq. [8] is trivial, as the singularity problem is removed by the azimuthal integration of Eq. [2] leading to Eq. [8]. However, some discussion follows because of the beam representation problem. The quantity $-en(r_1, z)$ is the charge density which is equal to $j(r_1, z)/v(z)$ in terms of the current density and velocity at z (we ignore the very minor variation in velocity with r_1). Thus Eq. [8] becomes (with $v \propto \Phi^{1/2}$)

$$E(R) = \frac{\beta}{r\Phi^{1/2}}\int_{r_1 < r} d^2 r_1 j(r_1), \qquad \beta \equiv \frac{(m/2e)^{1/2}}{2\pi\epsilon_0}, \qquad [9]$$

where we have chosen to write the integral in a more general fashion even though $j(r_1)$ is rotationally symmetric. Here, Φ is the (constant) potential in the drift region; it is high enough to ignore the small contribution of the initial electron kinetic energy. The fact that $d^2r_1 j(r_1)$ of an annulus of current arises from a cathode annulus $d^2r_c j(r_c)$ can be used to construct the former from an initial cathode discretization. We assume that,[8, 15]

$$j_c(r_1) = \frac{1}{\pi\sigma^2} \int d^2r_2 j_p(r_2) e^{-(r_1 - r_2)^2/\sigma^2}, \qquad [10]$$

where $j_p(r_2)\, d^2r_2$ is the total current emitted in an annulus d^2r_2.

ELOP assumes that the integral (Eq. [10]) can be reconstructed from three electrons that enable us to determine the center and $1/e$ width of the Gaussian by fitting moments. Here, Eq. [9] is discretized into $3N$ pieces (with $3N$ trajectories) associated with Eq. [3]. The result for Eq. [9] is

$$E(R) = \frac{2\pi\beta}{r\Phi^{1/2}} \sum_{n=0}^{N-1} \sum_{i=1}^{3} a_i n h_c^2 j_c(n h_c) \theta(r_{ni} - r), \qquad [11]$$

where θ is the Heaviside stepfunction that is zero for negative and unity for positive argument. Here, h_c is the discretization interval, and

$$a_1 = (1 + 2e^{-1})^{-1}, \qquad a_2 = a_3 = e^{-1} a_1, \qquad [12]$$

represent the discretization of the Gaussian thermal distribution into three electrons, one at the peak value and two at $1/e$ values, all in one meridional plane with the axis.

It is useful to gun designers to know the ultimate slit current $j_s(r)$ defined as

$$j_s(x) \equiv \int_{-\infty}^{\infty} dy\, j(x, y) = 2 \int_x^{\infty} dr \frac{r j(r)}{(r^2 - x^2)^{1/2}}. \qquad [13]$$

The slit current $j_s(x)$ can be calculated from Eqs. [13], [10], and the approximations underlying Eq. [11] by means of an algorithm developed by Campbell.[8] Only $3N$ electrons need be traced from the cathode on, where N is an integer of the order of 10, to obtain beam representations accurate to well within 5% of ELOP-calculated kinescope beams. Figs. 2 to 4 show comparisons of the above approximations to results obtained from a full-scale computer simulation with the RCA electron-optics program ELOP.[8]

Because space-charge forces are proportional to current density and to length squared, agreement is best in Fig. 2, which simulates a 1.5-mA beam in the DR of a relatively short kinescope. The effect of space

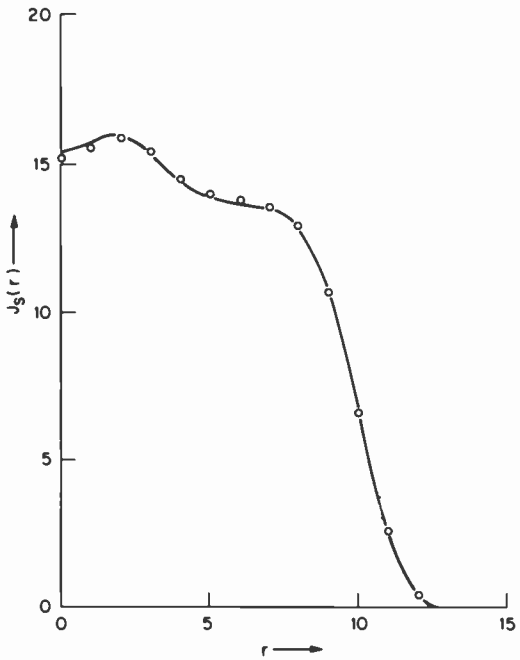

Fig. 2—Slit current $J_s(r)$ in arbitrary units at the screen versus r for the full numerical simulation (curve) and for approximation of the space charge forces based on Eq. [11] (circles). The drift parameters are L = 7.06 inches, V = 30 kV, and I = 1.5 mA.

charge is clearly not negligible at 3.5 mA, as can be seen in Fig. 3, so that it must be incorporated in simulations of typical high-intensity TV screen spots. The shape of the beam of Fig. 3 was varied to produce the quite differently shaped spots in Fig. 4. In all cases, agreement is close to or within the accuracy of the ELOP program.

Beam representation of asymmetric beams is much more difficult because the integral in Eq. [10] is then essentially two-dimensional so that azimuthal smoothing cannot be taken advantage of. However, several symmetric beams were subjected to the more general space-charge field approximations Eqs. [6, 7], and the resulting symmetric spot provided a radial distribution of final screen coordinates $r_m (1 \leq m \leq 3N)$ that could be processed with the azimuthal smoothing as above. In Figs. 5 and 6, two cases are compared with results of the ELOP program. The beam in Fig. 5 is the same as that in Fig. 3; agreement with the numerical computer simulation is perhaps fortuitously good. The beam simulation in Fig. 6 illustrates an interesting aspect of the asymmetric approximations; the mesh choice N_{sc} = 11 gives a poorer result than N_{sc} = 9. The reason is that the number of space-charge meshblocks, N_{sc}^2, must not be so large that the smoothed number density is granular (i.e., so that there are only a few, or less, electrons

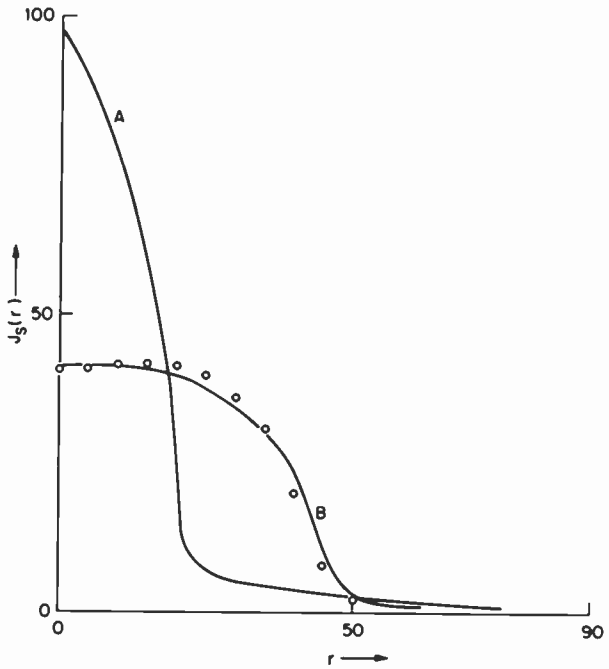

Fig. 3—Slit currents $J_s(r)$ versus r for a drift region with L = 13.5 inches, Φ = 30 kV, and I = 3.5 mA, without space charge (A) and with space charge (B). The circles show the transverse space charge approximation based upon Eq. [11].

per meshblock). The granularity introduces errors in the space-charge forces (Eq., [7]) where the denominators can become too small. On the other hand a very low value of N_{sc} will smooth out the space-charge forces too much. Apparently N_{sc} = 9 is close to an optimal choice as shown in Fig. 6.

3. Field Approximations in the Main Lens Region

The electron beam, having passed a crossover region in the BFR, enters the first cylindrical field-free region of the MLR and is refocussed towards the center of the screen by one or several more cylindrical-lens parts. It then exits into the DR in a field-free region at the so-called ultor voltage[10] of the rest of the kinescope vacuum tube. It is customary to use two or more coaxial cylindrical metallic tubes, all of the same radial extent interspaced with small gaps, as main lens. Each cylinder is given its own voltage, which is maintained during operation of the tube.

It is well-known[6, 16] that the interior of a cylinder of radius R with a boundary potential profile $\Phi(R, z) = V(z)$ (where z is the axial

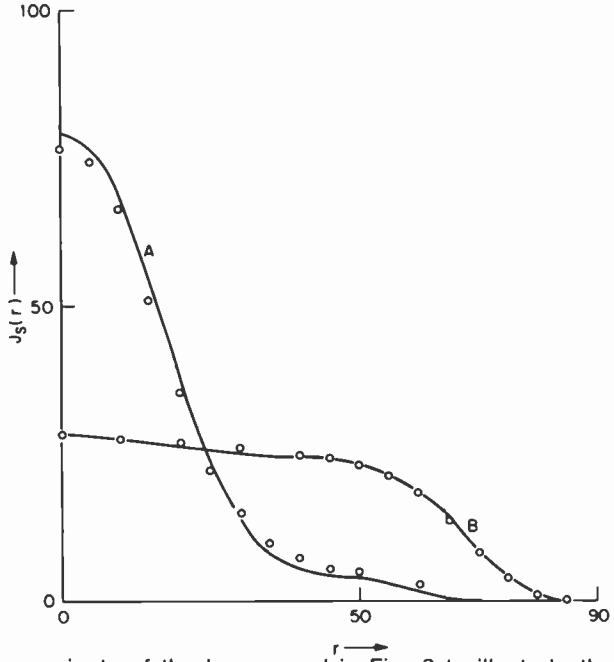

Fig. 4—Two variants of the beam used in Fig. 6 to illustrate the effect of varying electron trajectories in a drift region. An overfocussed beam (A) and underfocussed beam (B) give slit currents evaluated by computer (curves) and with Eq. [11] (circles).

direction) is governed by a potential

$$\Phi(r, z) = \frac{1}{2}\int_{-\infty}^{\infty} dz_1 V(z_1) g(r, z - z_1),$$

$$g(r, \zeta) \equiv \frac{2}{\pi}\int_0^{\infty} dk \frac{J_0(kr)}{J_0(kR)} \cos(k\zeta), \qquad [14]$$

with modified Bessel functions $J_0(kr)$ and $J_0(kR)$ in the Green's function $g(r, \zeta)$. Under the reasonable (and tested) assumption that $V(z)$ is constant on a metallic cylinder and linear in the gaps, Eq. [14] can be reduced to

$$\Phi(r, z) = \frac{1}{2}(V_0 + V_N) + \frac{1}{2}\sum_{n=1}^{N} \frac{V_n - V_{n-1}}{d_n} \int_{z_n}^{z_n + d_n} dz' G(r, z - z')$$

$$G(r, \zeta) \equiv \frac{2}{\pi}\int_0^{\infty} dk \frac{J_0(kr)}{k J_0(kR)} \sin(k\zeta). \qquad [15]$$

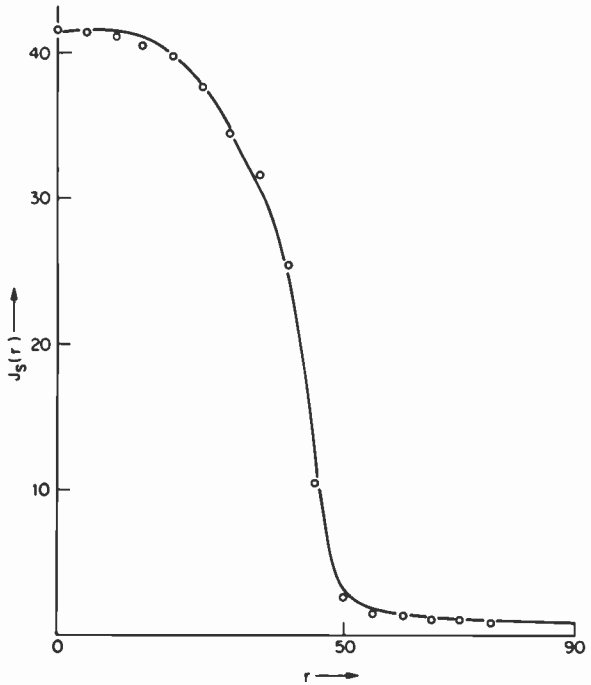

Fig. 5—Slit current $J_s(r)$ versus r for the same situation as in Fig. 3. The transverse space-charge approximation (circles) is evaluated as if the beam were asymmetric with Eq. [7].

The geometry is depicted in Fig. 7. Although the dz' integration can be performed in closed form, it is preferable to write it as above at this stage. The interior potentials (and fields) are thus given as an integral over an oscillatory integrand that must be evaluated numerically. The slow oscillatory asymptotic decrease of the integrand requires many steps in the numerical evaluation. Apparently the evaluation of Eq. [15] offers no clear numerical advantage over the numerical solutions[5] of Laplace's equation in a cylindrical region.

However, Bertram[11] found as early as 1940 that the function $G(0, \zeta)$ is simulated to within 6% errors for $|\zeta| \leq 1.5R$ by the function

$$G_B(0, \zeta) = \tanh(1.318\ \zeta R). \qquad [16]$$

This approximation of the axial Green's function can be improved[17] to give better than 2% accuracy with a two-term version of Eq. [16]

$$G_A(0, \zeta) = A_1 \tanh(w_1 \zeta/R) + A_2 \tanh(w_2 \zeta/R), \qquad [17]$$

with $A_1 = 0.800987$, $A_2 = 1 - A_1$, $w_1 = 1.20241$, $w_2 = 1.82456$ to six

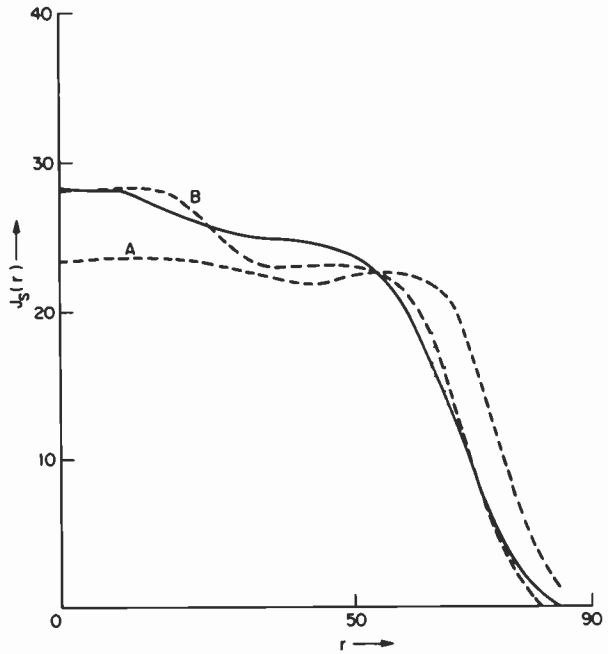

Fig. 6—Slit current $J_s(r)$ versus r for a drift region with L = 13.5 inches, Φ = 20 kV, and I = 3.5 mA (full curve) compared to two calculations based on Eq. [7]: (A) with N_{sc} = 11 and (B) with N_{sc} = 9.

significant figures. The result for $\Phi(0, \zeta)$ is,

$$\Phi(0, z) = \frac{1}{2}(V_0 + V_N) + \frac{R}{2}\sum_{n=1}^{N}\frac{V_n - V_{n-1}}{d_n} \sum_{i=1}^{2} A_i \ln\left\{\frac{\cosh[w_i(z - z_n)/R]}{\cosh[w_i(z - z_n - d_n)/R]}\right\}. \quad [18]$$

The off-axis contributions can be obtained from the symbolical form,

$$\Phi(r, z) = J_0(r\partial/\partial z)\Phi(0, z), \quad [19]$$

where the Bessel function $J_0(r\partial/\partial z)$ is expanded into its Taylor series as if $\partial/\partial z$ were a coefficient of r. The functions in Eq. [18] are analytically differentiable, so that off-axis potentials and fields are easily generated from Eqs. [18] and [19]. The four coefficients in Eq. [17] are obtained by fitting the derivative $G_A'(0, \zeta)$ to $g(0, \zeta)$ at $\zeta = 0$, and at $\zeta = \infty$ using the asymptotic expansion of $g(0, \zeta)$.[18] Thus, an inexpensive simulation of electron beams in standard cylindrical ML lenses can be obtained from numerical integration of the trajectory equations Eq. [3] with additive electrostatic fields approximated by

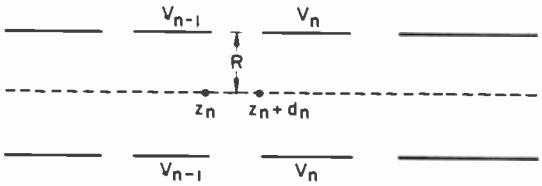

Fig. 7—Sketch of the geometry of a compound axially symmetric cylinder lens with coaxial, equi-radius components.

Eq. [11] for the space-charge forces and by Eq. [18] and [19] for the Laplace forces due to the lens.

A simulation due to lens effects alone is given in Table 1. Here, two cylinders with radius $R = 100$ units (1 inch is 1000 units*) have been chosen. The gap between them is $0.5R$ wide and it lies at $5R$ from the input plane. The output trajectory coordinates r and r' lie at $8.5R$ from the input plane. The input coordinates are not given, but they arise from seven triplets leaving the cathode in one plane containing the axis. Each triplet is emitted at $r_c = m$ units above the axis ($0 \leq m \leq 7$) with $r_c' = -1$ (−sign), 0, or +1 (+sign). Fig. 8 illustrates the trajectories of the $r_c' = 0$ electrons in this region.

The effect of space charge can be shown to be small in this region.

Table 1—Comparison of r,r' in an MLR

r_c	ELOP		2-Term Bertram	
	r	$r' \times 10^3$	r	$r' \times 10^3$
+0	−2.65	0.30	−2.68	0.21
−1	6.06	0.50	6.15	0.71
1	0.47	0.17	0.48	0.19
+1	1.69	1.08	1.72	1.14
−2	8.93	1.19	9.06	1.49
2	5.62	1.20	5.71	1.40
+2	6.45	1.20	6.56	2.22
−3	11.93	1.67	12.12	2.11
3	10.20	1.98	10.35	2.34
+3	11.32	2.73	11.49	3.12
−4	14.67	2.03	14.88	2.53
4	15.27	2.60	15.49	3.12
+4	16.56	3.18	16.81	3.76
−5	19.16	2.21	19.43	2.86
5	20.00	2.78	20.28	3.42
+5	22.54	3.07	22.88	3.89
−6	23.00	1.78	23.33	2.56
6	24.90	2.20	25.25	3.04
+6	28.64	2.00	29.02	2.91
−7	25.86	0.16	26.23	1.09
7	29.23	0.36	29.63	1.35

* One inch is 1000 mils in engineering terminology. I prefer to use the word "unit" because absolute lengths need not be specified in general.

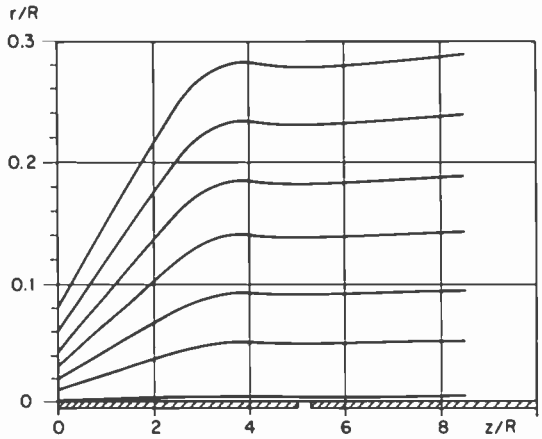

Fig. 8—The trajectories (which lie in one plane through the axis) of seven principal electrons traversing a two-cylinder lens with gap length $0.5R$ and voltage ratio 0.24.

It was excluded from the above example to separate out the effect of the lens approximation. The accuracy in Table 1 is not unreasonable. An error in r' of 0.0004 yields only a 5.5 unit error in r at 13.5 inch (13,500 units) beyond the exit plane, which is acceptable in kinescope spot analysis, at least in an initial determination of parameters.

4. Field Approximations in the Beamforming Region

The analysis of electron trajectories is most difficult in the BFR. While it is true that a (thermionic) cathode emits electrons under the influence of a shaped electric field created by appropriate voltages on the BFR electrodes labeled $G1$ and $G2$ (see Fig. 1), this emission is initially space-charge limited.[19,20] That is to say that the space-charge forces are dominant in the region very close to the cathode (of one to two length units extent, typically), and, moreover, they are largely longitudinal, not transverse. Thus, the electrostatic fields differ sharply from those due to the lens elements alone in this "diode region", and the transverse-space-charge approximation does not apply.

Furthermore, even though a rapid transition takes place beyond the diode region to one in which Laplace forces dominate, the current modulation properties of the $G1$ and $G2$ electrodes force the principal electrons (those with no transverse velocity at the cathode) to cross over the axis somewhere between $G1$ and $G2$ so that relatively large space-charge forces may again occur in a restricted "crossover region."

The analysis by which electron trajectories through the diode region are calculated is postponed until the next section. The input for the

work in this section is a diode plane several units beyond the cathode with values of r and $r' = dr/dz$ of the electron coordinates.

The analytical model for each aperture electrode in the BFR is a pair of infinitesimally thin perfectly conducting plates at voltage V with circular apertures of radius R coaxial with the gun axis. The analytical expression for the potential that arises from one of these in isolation with asymptotic fields E_L (at $z = -\infty$) and E_R (at $z = \infty$) is well known:[21]

$$\Phi(r, z) = V - \frac{1}{2}(E_L + E_R)z + \frac{1}{\pi}(E_L - E_R)|z|\left[A(u) + \frac{1}{u}\right], \quad [20]$$

where $A(u) \equiv \arctan(u)$, and

$$u^2 = \frac{1}{2R^2}\{(r^2 + z^2 - R^2) + [(r^2 + z^2 - R^2)^2 + 4R^2z^2]^{1/2}\}. \quad [21]$$

Regenstreif[22] found that $\Phi(0, z)$ for a coaxial set of three such aperture lenses could be given by a linear superposition of the $r = 0$ versions of Eqs. [20] and [21]. The idea of superposition has been generalized to more than three apertures and to off-axis potentials. Specifically, the BFR is modeled as shown in Fig. 9. Each of the two grids, $G1$ and $G2$, is modeled by a pair of aperture lenses at the same

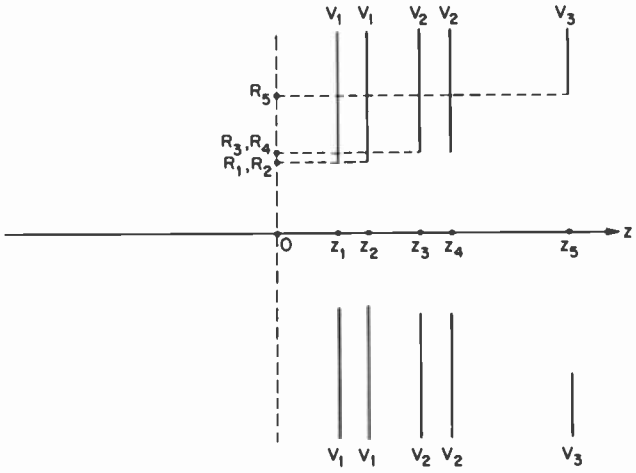

Fig. 9—Sketch of the BFR model by means of circular apertures. Only half of the total number of apertures are shown.

voltage. The entrance to the $G3$ grid requires only one further aperture lens at voltage V_3. To ensure a zero cathode voltage, the $z = 0$ plane is the result of an antisymmetric distribution of 10 aperture lenses in total; each of the 5 sketched ones in Fig. 9 has an antisymmetric counterpart at $z = -z_m$ with $V = -V_m (m = 1, \cdots, 5)$. The electrostatic potential is then approximated by

$$\Phi(r, z) = \sum_{m=1}^{5} \Phi_m(r, z)$$

$$\Phi_m(r, z) = \frac{1}{\pi} E_m \left\{ | z + z_m | \left[\frac{1}{u_m^+} + A(u_m^+) \right] \right.$$

$$\left. - | z - z_m | \left[\frac{1}{u_m^-} + A(u_m^-) \right] \right\}, \qquad [22]$$

$$(u_m^{\pm})^2 = \frac{1}{2R_m} \{ (r + (z \pm z_m)^2 - R_m^2)$$

$$+ [(r + (z \pm z_m)^2 - R_m^2)^2 + 4R_m^2 (z \pm z_m)^2]^{1/2} \},$$

and the fields are given by the expressions

$$E_1 = (V_1 - V_0)/z_1, \qquad E_3 = -E_2 = (V_2 - V_1)(z_2 - z_1), \qquad [23]$$

$$E_5 = -E_4 = (V_3 - V_2)/(z_3 - z_2).$$

The superposition (Eq. [22]) was obtained from linear combinations of Eq. [20] so that the uniform electric fields at $r \gg R$ are asymptotically correct. Certain restraints on the parameters are necessary to ensure accuracy of the approximation close to the axis (where electron trajectories cluster). For example, if only $V_5 \neq 0$ and $V_5 > 0$, then it can be shown that $z_4/R_4 < z_5/R_5$ is a necessary restraint, otherwise negative potentials will result on the axis. The problem is that a region close to $r = R_m$ and $z = z_m$ is incorrectly estimated and the extent of such a region can be obtained from a numerical analysis of Eq. [22].

A first test of the approximation has been to check if it predicts the proper cutoff voltage of $G2$ when $V_1 = -150V$, and V_3 is a fixed voltage of the order of 10 kV (different for different guns). The cutoff voltage is determined by the requirement that the E_z field at the center of the cathode be zero.

Six different gun BFRs have been tested, their parameters are listed in Table 2. The parameters t_1 and t_2 are the thickness of the $G1$ and $G2$ electrodes, whereas the spacings s_{01}, etc., pertain to those between the cathode and $G1$, etc. Certain details of BFR #4 not relevant to this study have been omitted. The cutoff voltages determined by the approximations in Eqs. [22] and [23] are given in Table 3.

The agreement between the analytical results based upon Eq. [22]

Table 2—Parameters of Test BFR's

	#1	#2	#3	#4	#5	#6
t_1	5.5	5	5	1	5	3
t_2	5.5	5	20	5	11	18.5
s_{01}	3	3	3	3	3	3
s_{12}	11.5	13	11.5	27	11	11.5
s_{23}	68	52	68	33	45	45
R_1	12.5	12.5	12.5	12.5	12.5	12.5
R_2	12.5	12.5	12.5	12.5	12.5	12.5
R_3	16	30	30	23	30	20
V_3(kV)	11.5	6.85	10.0	8.7	13.6	11.44

Table 3—Cutoff Voltages (Volts)

BFR	1	2	3	4	5	6
Numerical V_{co}	401	429	627	604	556	437
Analytical V_{co}	397	464	596	650	569	382

and the calculations by the computer program ELOP[8] range from good (#1, 3, 5) to fair (#2, 4, 6). However, fair agreement of V_{co} does not rule out good agreement of trajectory coordinates (see below).

We have also examined the effect of Laplace fields evaluated with Eq. [22] together with the transverse space-charge approximation (Eq. [11]) on numerical integration of the trajectory equations (Eq. [3]), in the BFR for the six different sets of BFR parameters tabulated in Table 2. The results for r are shown in Fig. 10, and those for $r' = dr/dz$ are compared with the full numerical analysis (the left column of each pair of columns) in Table 4. These trajectories originate from triplets of electrons emitted at the cathode at $r_c = m$ units from the center with $r_c' = 0$ (PR), $r_c' = 1$ (THU), and $r_c' = -1$ (THD). Their coordinates at the entrance plane ($z = 2$ units) of this calculation need not be specified here. Several conclusions can be drawn:

(1) It is evident from the last four columns of Table 4 (for BFR #6) that space charge is mainly responsible for the discrepancies between the numerical-field approximation in the left and the analytical-field approximation in the right of each pair of columns. Evidently, the approximation (Eq. [22]) by itself is good, even though the cutoff voltage of BFR #6 (see Table 3) is estimated somewhat low.

(2) Some of the discrepancies in r' may be due to the way Gaussians are fitted to the thermal distribution in Eq. [10]. Fig. 10 indicates a decrease in σ, and therefore larger errors in regions where the principal test electron does not lie between the two thermals, as one progresses from BFR #1 to BFR #6. The full numerical values of r are not shown; they agree quite well and the small discrepancies are not of importance compared with those in r' in determining the accuracy of trajectories deeper into the gun. Errors are largest

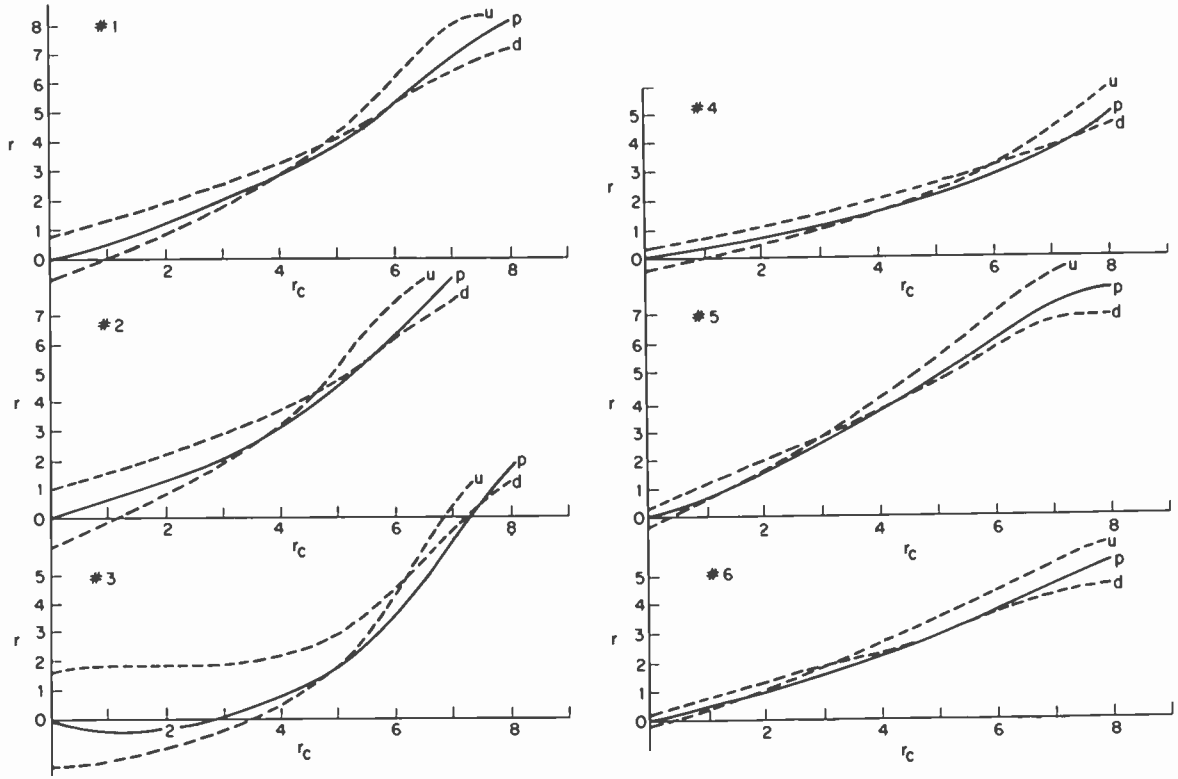

Fig. 10—Graphs of exit r versus cathode r_c for six BFR's. Each graph contains curves for one principal electron (p) and its two associated thermals (u,d).

Table 4—$r' \times 10^3$ for Six Test BFRs

		#1		#2		#3		#4		#5		#6		No Space Charge #6	
PR	1	−6.5	−3.7	−6.8	−2.1	1.1	3.7	−7.6	4.6	7.3	−5.1	−6.8	−5.8	−9.3	−8.7
PR	2	−13.9	−14.1	−14.4	−13.5	−1.9	−2.1	−15.6	−15.1	−15.2	−15.5	−14.7	−15.6	−18.3	−17.2
PR	3	−22.2	−24.1	−23.5	−23.7	−6.1	−9.1	−23.2	−24.7	−23.6	−25.7	−22.1	−25.3	−26.8	−25.4
PR	4	−31.3	−34.1	−33.9	−34.8	−12.1	−16.2	−31.2	−33.9	−32.1	−35.2	−29.8	−34.6	−34.3	−32.8
PR	5	−41.3	−44.3	−45.9	−45.6	−19.8	−23.0	−39.2	−43.5	−40.7	−44.4	−36.9	−42.9	−40.5	−39.0
PR	6	−52.0	−53.4	−58.8	−56.8	−30.2	−31.0	−47.3	−51.6	−49.1	−52.8	−43.1	−49.7	−44.2	−43.1
PR	7	−61.1	−62.3	−67.3	−66.6	−42.2	−40.0	−54.8	−59.0	−55.0	−59.8	−46.5	−53.2	−43.5	−43.3
PR	8	−6.00	−68.0			−43.6	−44.9	−58.2	−59.6	−48.9	−58.4	−39.0	−50.6	−32.8	−32.1
THU	0	3.5	1.9	3.9	5.5	8.1	7.8	−1.4	−1.2	−0.7	−1.6	−3.5	−5.2	−8.2	−10.9
THU	1	−5.3	−7.7	−5.3	−4.4	4.2	2.0	−10.0	−10.8	−10.0	−11.7	−11.9	−14.9	−17.5	−19.0
THU	2	−14.1	−17.5	−14.9	−15.4	−1.5	−4.1	−18.7	−20.6	−18.9	−21.8	−20.6	−24.7	−26.3	−27.5
THU	3	−23.9	−27.6	−26.1	−25.9	−7.5	−10.3	−27.2	−30.6	−28.4	−31.8	−29.4	−34.5	−34.7	−35.4
THU	4	−34.6	−37.8	−38.9	−37.2	−14.6	−17.3	−36.5	−40.3	−38.0	−41.9	−38.1	−44.2	−42.1	−42.4
THU	5	−46.4	−47.7	−53.4	−49.5	−23.2	−26.0	−45.9	−50.0	−47.3	−50.9	−45.5	−51.8	−47.3	−48.0
THU	6	−59.1	−64.7	−68.6	−62.4	−35.0	−33.7	−54.8	−58.4	−55.9	−59.9	−50.2	−58.4	−50.8	−51.2
THU	7	−68.6	−68.4			−48.2	−41.7	−61.5	−63.8	−60.6	−65.5	−50.9	−60.6	−48.2	−49.8
THD	0	−3.5	−1.9	−3.9	−5.5	−8.1	−7.8	1.4	1.2	0.7	1.6	3.5	5.2	8.2	10.1
THD	1	−10.9	−10.4	−12.8	−13.7	−11.8	−12.4	−6.8	−7.7	−7.3	−7.7	−4.6	−4.3	−1.0	−1.6
THD	2	−17.5	−18.7	−20.0	−21.7	−14.1	−15.4	−14.5	−16.9	−14.6	−15.8	−11.6	−13.5	−10.1	−7.0
THD	3	−24.4	−26.0	−27.2	−28.2	−15.5	−18.6	−21.9	−23.9	−21.9	−24.1	−18.4	−21.2	−18.5	−15.2
THD	4	−32.0	−33.8	−35.4	−35.1	−19.0	−20.5	−29.5	−31.8	−29.6	−32.2	−25.4	−40.4	−26.2	−22.9
THD	5	−40.2	−40.9	−44.4	−44.3	−24.8	−23.8	−36.7	−38.7	−37.2	−39.0	−31.9	−36.5	−32.5	−29.4
THD	6	−48.4	−50.2	−53.7	−54.2	−32.1	−30.9	−43.7	−45.8	−44.2	−47.6	−37.5	−41.1	−36.5	−34.1
THD	7	−54.9	−58.0	−58.1	−61.9	−39.7	−38.6	−49.7	−53.1	−48.4	−53.9	−39.9	−47.5	−36.3	−35.0
THD	8	−49.6	−62.2			−36.1	−42.4	−50.9	−51.4	−38.1	−50.4	−28.9	−43.1	−25.2	−23.5

for electrons emitted furthest from the cathode center, but concomitant current contributions from the edge electrons are small.

Thus, even though the effect of space charge is appreciable in the BFR and even though the transverse space-charge force approximation might not be accurate in the crossover region, it appears that fair to good predictions for electron coordinates at the end of the BFR can be made with these simplifying approximations.

The approximations ignore the effect of induced charges in the grids. Sample calculations show the effect of these to be negligible compared with other errors. The neglect of the longitudinal space-charge force was investigated in detail for BFR #6. Fig. 11 shows a comparison of both for the first 150 length units. Up to the crossover region (at $z \approx$ 50 units), the neglect of longitudinal space-charge fields is somewhat serious, probably also accounting for some of the discrepancies. The rapid transition from longitudinally-dominant to transverse-dominant forces is quite apparent at the end of a diode region only a few length units long.

5. The Initial Equivalent-Diode Region

In this section, we present an approximate analysis of the difficult "diode region" of the BFR in which electron emission is space-charge

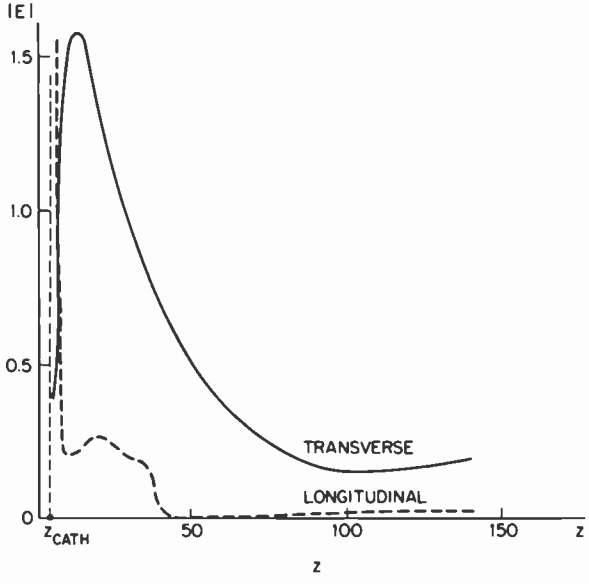

Fig. 11—A comparison in BFR #6 of longitudinal and transverse space-charge fields.

limited, i.e., the preceding cloud of emitted electrons shields its successor from the applied Laplace field so that the electric field at the cathode is essentially zero in the emitting region.

In the circularly symmetric cathode vicinity, the Laplace potential can be written as

$$\begin{aligned}\Phi^L(r, z) &= \Phi^L(0, z) - \tfrac{1}{4}r^2\Phi''(0, z) \\ &= \Phi^L(0, z)[1 - r^2/R_c^2],\end{aligned} \tag{24}$$

to the extent that r^4 and higher-order terms may be neglected. This equality gives a working definition of an effective cathode radius R_c. For $r \ll R_c$, Eq. [24] is a two-term expansion of

$$\Phi^L(r, z) = J_0(2r/R_c)\Phi^L(0, z). \tag{25}$$

One can verify that Eq. [25]) is the solution of the Laplace equation if $\Phi^L(0, z)$ is a linear combination of $\sinh(2z/R_c)$ and $\cosh(2z/R_c)$. Hence, an acceptable solution of $\Phi(r, z)$ with $\Phi^L(0, z) = V_c$ is

$$\Phi^L(r, z) = V_c + v \sinh(2z/R_c) J_0(2r/R_c), \tag{26}$$

where v is an unknown constant voltage determined by the geometry. Fields[23] made the crucial point that the situation in the BFR very close to the cathode is indistinguishable from one in an effective diode where an anode at voltage V_A at some distance d_A produces Eq. [26] as well as the proper solution to the Poisson equation close to the cathode. That is to say, Eq. [26] can be rewritten in terms of this equivalent diode as,

$$\Phi^L(r, z) = V_c + (V_A - V_c)\frac{\sinh(2z/R_c)}{\sinh(2d_A/R_c)} J_0(2r/R_c), \tag{27}$$

even though this predicts the Laplace potential correctly only for an immediate vicinity of the cathode center. In the case of a purely one-dimensional situation ($R_c \to \infty$) it can be seen[23] from Eq. [27] that d_A reduces to the length $d_0 = [\partial E_z{}^L(0, 0)/dV_c]^{-1}$. On the other hand, Eq. [27] yields

$$\frac{\partial E_z{}^L(0, 0)}{\partial V_c} = \frac{2/R_c}{\sinh(2d_A/R_c)}, \tag{28}$$

so that by inversion we relate an effective diode length d_A to the physical length $d_0 \equiv [\partial E_z{}^I(0, 0)/dV_c]^{-1}$,

$$\begin{aligned}d_A &= \tfrac{1}{2}R_c \ln[(2d_0/R_c) + (1 + 4\, d_0{}^2/R_c{}^2)^{1/2}] \\ &= \tfrac{1}{2}R_c \operatorname{arc\,sinh}(2d_0/R_c).\end{aligned} \tag{29}$$

Note that d_0 is entirely determined by the geometry and the Laplace fields of the real problem, where d_A also contains the curvature radius R_c which will later be replaced by an effective beam radius.

Close to the cathode, the fields are governed by the Poisson equation,

$$\frac{\partial^2\Phi}{\partial z^2} + \frac{1}{r}\frac{\partial}{\partial r}\left(r\frac{\partial\Phi}{\partial r}\right) = \frac{1}{\epsilon_0}\rho(r, z) \approx 2\pi\beta\frac{j(r, z)}{\Phi^{1/2}}, \qquad [30]$$

where $j(r, z)$ is the current density and β is the constant given in Eq. [9]. If $\Phi(r, z)$ has $J_0(2r/R_c)$ as a factor containing all the dependence upon r, then the correct solution of Eq. [30] can be written

$$j(r) = \frac{2}{9\pi\beta}\frac{[\Phi(r, z) - V_c]^{3/2}}{\bar{R}_c^2[\sinh(z/\bar{R}_c)]^2}, \qquad [31]$$

where $\bar{R}_c = 2R_c/3$. Now we apply Eq. [31] at $z = d_A$, the effective anode position, and replace the numerator, using Eq. [27],

$$\Phi(r, d_A) - V_c = \tfrac{1}{2}R_c[-E_z^L(r, 0)]\sinh(2d_A/R_c) \qquad [32]$$

to obtain the following analytical expression for the estimated current density:

$$j(r) = \frac{2}{9\pi\beta}[-E_z(r, 0)]^{3/2}D^{-1/2},$$
$$D = \frac{128}{81}R_c\frac{[\sinh(3d_A/2R_c)]^4}{[\sinh(2d_A/R_c)]^3}, \qquad [33]$$

where d_A is given by Eq. [29] and $d_0 \equiv (\partial E_z^L/\partial V_c)^{-1}$ at the center of the cathode. The remarkable aspect of Eq. [33] is that the estimate does not require a lengthy iterative numerical simulation by computer; only the Laplace fields $E_z(r, 0)$ are needed and they are easily obtained from the approximations in the previous section. However, several defects in the assumptions must be borne in mind:

(1) The assumption that potential and current are proportional to $J_0(2r/R_c)$ is incorrect for values of r close to R_c. Fortunately $j(r)$ is very small when $|R_c - r| \ll R_c$.

(2) The curvature radius R_c is close to, but not equal to the effective beam radius, and furthermore R_c is a decreasing function of z in the diode region (in contrast to the constant R_c assumed in developing Eq. [32]). Table 5 shows predictions of $j_c(r)$ made on the basis of Eq. [33] with an ad hoc adjustment for the above points by replacement of R_c in Eq. [33] by $\tilde{R}_c$ [~70% of the actual beam radius obtained from the location on the cathode where $E_z^L(r, 0) = 0$)]. Each pair of columns gives the numerically approximated current (density) to the left and the analytically estimated one to the right. The current density $J_c(m) = 2\pi\beta j_c(mh)$,

where $h = 1$ unit, and $2\pi\beta \approx 190.43$ if $j_c(mh)$ is to be in mA. The total current I in mA is also given.

When reasonably accurate densities have been established by this procedure, we then use Eq. [3] to simulate electron trajectories in the short diode region, with a version of Eq. [31] that gives the Child's law potential and fields in terms of the estimated current densities. At the end of the diode region, a transition is made to the transverse space-charge approximation. This abruptness of the transition, exemplified in Fig. 11, makes it possible to estimate its location from experience with an entire class of not-dissimilar cathode-$G1$ regions.

Table 5—Current Densities Predicted by Eq. [33] Compared with Computer-Determined Ones

	#1		#2		#3		#4		#5		#6	
I(mA)	3.50		2.02		3.48		3.55		3.73		3.47	
$J_c(0)$	6.41	6.06	4.37	4.40	6.21	6.45	5.09	6.72	6.66	6.98	5.66	5.95
$J_c(1)$	6.31	5.97	4.30	4.32	6.12	6.34	5.05	5.65	6.57	6.86	5.60	5.87
$J_c(2)$	6.02	5.69	4.06	4.06	5.85	6.03	4.91	5.44	6.28	6.51	5.40	5.62
$J_c(3)$	5.53	5.24	3.68	3.64	5.41	5.50	4.69	5.07	5.79	5.93	5.07	5.20
$J_c(4)$	4.85	4.60	3.14	3.07	4.77	4.77	4.35	4.56	5.11	5.13	4.58	4.61
$J_c(5)$	3.96	3.80	2.44	2.35	3.93	3.85	3.87	3.86	4.21	4.13	3.91	3.83
$J_c(6)$	2.89	2.86	1.62	1.54	2.90	2.77	3.22	2.97	3.11	2.96	3.03	2.87
$J_c(7)$	1.69	1.81	0.69	0.69	1.72	1.60	2.37	1.91	1.87	1.70	1.96	1.77
$J_c(8)$	0.47	0.76			0.48	0.49	1.29	0.76	0.56	0.53	0.72	0.65

6. Conclusions

The purpose of this work has been to replace accurate but costly numerical simulation (by digital computer) of electron trajectories in kinescope guns by analytical approximations to provide the gun designer with a flexible, low-cost, exploratory tool. We have found that space-charge forces can be approximated by transverse electric fields in typical kinescope beams at high accuracy beyond the crossover region in the BFR. Between the cathode and the crossover region, the transverse-field approximation is somewhat (but not seriously) in error, as long as the immediate vicinity is properly treated separately as an effective diode. For this reason, it is emphasized that the approximations in this work are most useful in the drift region, and in the main-lens region when circularly symmetric cylinder lenses of equal radius are utilized.

Cathode current distributions can be estimated from the Laplace fields. These, in turn, can be approximated analytically in axially symmetric guns with conventionally shaped grids and lenses. While such analytical approximations also carry with them some loss in accuracy, they provide a tremendous gain in time and cost, and therefore are especially useful for exploratory design in which high

accuracy (well within 10% of the ELOP numerical calculations) is not yet necessary.

Acknowledgements

I am grateful to R. W. Cohen whose interest in a simplified analysis spurred me on to attempt the present one, to C. H. Anderson for inducing me to refine the space-charge approximation, and to R. C. Alig and F. J. Campbell for critical discussions and review of this work.

References

[1] C. Weber, "Numerical Solution of Laplace's and Poisson's Equations and the Calculation of Electron Trajectories and Electron Beams," in *Focussing of Charged Particles*, A. Septier (Ed.), Academic Press, N.Y. (1967).
[2] P. W. Hawkes, "Compilation of a Catalogue of Computer Programs in Electron Optics," *Computer Phys. Commun.*, **5**, p. 399 (1973).
[3] Any of the classical treatises on electron optics, e.g., V. K. Zworykin, G. A. Morton, E. G. Ramberg, J. Hillier, A. W. Vance, *Electron Optics and the Electron Microscope*, J. Wiley, N.Y. (1945).
[4] D. Potter, *Computational Physics*, J. Wiley, N.Y. (1977); R. W. Hockney, J. W. Eastwood, *Computer Simulation Using Particles*, McGraw-Hill, N.Y. (1981).
[5] M. A. Jaswon and G. T. Symm, *Integral Equation Methods in Potential Theory and Elastostatics*, Academic Press, London, U.K. (1977).
[6] P. Grivet, *Electron Optics* (2nd English Ed.), Pergamon Press, Oxford, U.K. (1972).
[7] T. Saito S. Kubota, and S. Miyaoka, "Digital Computer Studies of Electron Lenses for Cathode Ray Tubes," *J. Appl. Phys.*, **44**, p. 4504 (1973).
[8] F. J. Campbell, private communication; see also R. H. Hughes and H. Y. Chen, "A Novel High-Voltage Bipotential CRT Gun Design," *IEEE Trans. Consumer Electron.*, **CE-25**, p. 185 (1979).
[9] D. L. Say, R. B. Jaeger, and J. D. Ryan, "Electron Optics for CRT's: Computer Modeling," *IEEE Trans. Consumer Electron.*, **CE-21**, p. 57 (1975).
[10] R. C. Alig, "Kinescope Electron Gun Design," *RCA Review*, **41**, p. 517 (1980).
[11] S. Bertram, "Determination of the Axial Potential Distribution in Axially Symmetric Electrostatic Fields," *Proc. IRE*, **28**, p. 418 (1940). See also Ref. (6), Sec. 8.1.
[12] E. Regenstreif, "Theorie de la Lentille Électrostatique à Trois Électrodes," *Ann. Radioel.*, **6**, p. 51 (1951).
[13] J. D. Lawson, *The Physics of Charged-Particle Beams*, Clarendon, N.Y. (1977).
[14] E. G. Ramberg in Ref. (3), Sec. 12.1.
[15] K. J. Harte, "Theory of Aberration Mixing in Electron-Optical Systems," *J. Vac. Sci. Technol.*, **10**, p. 1098 (1973).
[16] A. B. El-Kareh and J. C. J. El-Kareh, *Electron Beams, Lenses, and Optics*, Academic Press, N.Y. (1970) (see Sec. 3.5).
[17] R. W. Klopfenstein, private communication.
[18] Ref. (6), formula (8.1).
[19] W. Franzen, J. H. Porter, "Energy Spectrum of Electrons Emitted by a Hot Cathode," in L. Morton (Ed.) *Advances in Electronics and Electron Physics*, Vol. 39, Academic Press, N.Y. (1975).
[20] O. Klemperer, *Electron Optics*, Cambridge, U.K. (1971).
[21] E. G. Ramberg in Ref. (3), Sec. 11.8.
[22] Ref. (6), Sec. 8.2.
[23] J. R. Fields, private communication. Fields first pointed out the connection between $(\partial E_z^L/\partial V_c)^{-1}$ and an effective diode width.

Miniature Beryllia Circuits—A New Technology for Microwave Power Amplifiers

F. N. Sechi, R. Brown, H. Johnson, E. Belohoubek, E. Mykietyn, and M. Oz*
RCA Laboratories, Princeton, NJ 08540

ABSTRACT—A new technology for fabricating miniature circuits on glazed beryllium oxide has been developed that is particualrly well suited for miniature, light weight, high performance GaAs power amplifiers.

1. Introduction

Over the last few years a large number of efforts,[1] both government and company sponsored, have been aimed at applying monolithic process technologies to microwave circuits. Whereas in certain applications[2-4] monolithic integrated circuits offer distinct advantages, they are not well suited for high power applications, especially if optimum performance with high design flexibility is required and only moderate quantities are involved.

A new miniature hybrid technology is described here that combines the advantages of very small size, light weight, and the batch fabrication process of the monolithic approach with the flexibility of using separately attached active devices of the hybrid approach. The new process uses a combination of distributed and lumped circuit elements defined on beryllium oxide (BeO) to provide circuit substrates that combine high Q with excellent heat dissipation properties. The BeO substrates, which are rough even when polished, are selectively glazed to provide smooth surfaces for the definition of high-quality-factor

* On sabbatical leave from A.D A., Israel.

lumped-element components, including inductors, thin-film capacitors and bridged interconnections. The active devices, GaAs power FETs in pellet form, are flip-chip mounted on unglazed sections of the BeO surface. A low parasitic ground connection for the FET source contacts is provided by a metal septum that is fabricated as an integral part of the BeO substrate. The fabrication process for the septum follows procedures developed originally for BeO carriers[5] for high power bipolar transistors.

The major advantages of the new technology are the small-size, light-weight properties of the circuits combined with excellent heat dissipation, and low loss. Since batch fabrication processes are used for the circuits, many of the advantages of monolithic circuits are preserved, while flexibility is maintained and the use of expensive GaAs substrates for the passive circuits (which often are one to two orders of magnitude larger than the active devices) is avoided. Since both circuits and devices are fabricated on separate substrates they can be better optimized for their intended functions. This is especially important for power applications where properties such as ease of mounting, good heat dissipation and low circuit losses are of paramount importance.

Circuit Description

Beryllium oxide, also called beryllia, has been the preferred mounting substrate for bipolar power transistors for many years. Since bipolar transistors are customarily fabricated with the back of the silicon chip as the collector, the mounting surface to which the transistor is attached must be dc isolated and becomes part of the rf matching circuit. BeO is ideally suited for this purpose.

With the advent of power GaAs FETs fabricated on semi-insulated substrates and featuring all three contacts—source, gate and drain—accessible on the top surface, the need for an electrically isolated mounting medium seemed to have disappeared. In effect, monolithic designs rely on the insulating substrate and on the availability of all three contacts at the top surface to easily integrate the active device with the rf circuit based on processing steps all performed on one side of the GaAs substrate.

This technology is well suited for low- and medium-power-level applications but leads to difficulties at higher power levels. The major reason is the incompatibility between requirements for good heat conduction and low rf losses. Specifically, for high power applications it is very important to fabricate the FETs on a very thin GaAs substrate—typically 2 to 4 mil thick—in order to dissipate the heat

effectively. However, the very thin substrates cannot maintain a high Q for matching components of very small size. In addition, thin substrates cause severe mechanical interface problems due to the inherent fragility of GaAs.

High Q for the circuit components is particularly important for power amplifiers, since the active devices require very high impedance transformation ratios. Some recent work by Schellenberg[6] using hybrid technology shows that very good device efficiencies can be obtained for high power FETs even at Ku-band. This approach is based on combining many FET cells with very low impedance $\lambda/4$ transformers on thin substrates. In principle, this technique could also be applied to a fully monolithic design. However, large $\lambda/4$ matching lines are required, which results in an unfavorable ratio of circuit to device area, particularly at frequencies below 20 GHz.

In view of the above considerations and noting that, for most GaAs power amplifier applications of today, the fabrication volume is not large enough to justify a fully monolithic implementation, the need for a different approach is apparent. A new technology called MBC, short for miniature beryllia circuits, has been developed. It uses a common BeO substrate as the basic carrier for the devices and for all circuit components realized in either distributed or lumped form. Ground septums are provided wherever the circuit topology requires low inductance ground returns. The devices are flip-chip mounted on the BeO substrate which simultaneously provides very good heat conduction and low parasitic interconnections with the rf circuit. Since the thermal expansion coefficient of BeO and GaAs are nearly equal, the mounting of the devices can be achieved with very low thermal stresses.

Fig. 1 shows the principal implementation of the MBC technology for a two-stage power amplifier. Each stage has a ground septum that is the mounting base for the source contacts of the FET. In comparison with a hybrid technique, the elimination of wire bonds for interconnecting the devices with the circuit results in greatly improved reproducibility and a much lower assembly labor content. Mixed lumped and distributed circuits are used for input, interstage, and output matching. The substrate, containing two septums, is fabricated from three sandwiched BeO wafers, the center one having a thickness equal to the desired spacing of the ground septums. The BeO wafers are metallized with Cr-Cu and then thermocompression bonded at high temperature and pressure. After slicing and polishing, individual substrates, with thicknesses ranging typically from 10 to 50 mil, are available for circuit processing.

Since the surface quality of polished BeO is not suitable for the fabrication of thin-film capacitors, the BeO substrate is selectively

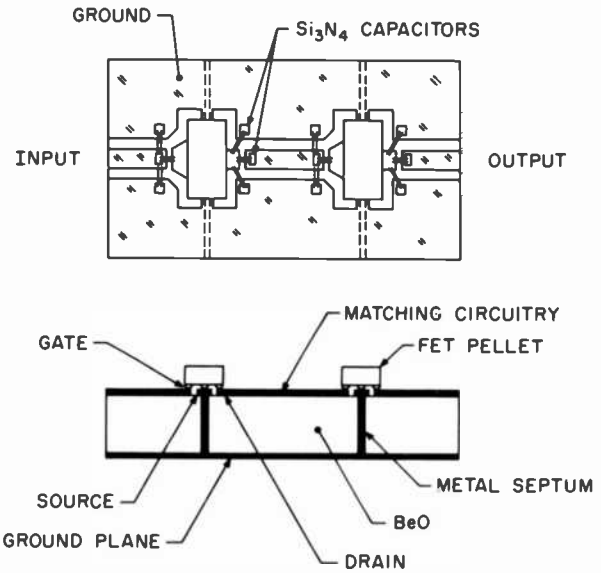

Fig. 1—Schematic drawing of two-stage MBC amplifier.

glazed to provide the necessary smooth, high-quality surface finish. Fig. 2 shows the individual layers of the MBC structure that is being used for high power amplifier applications. The thin-film base conductor forms the ground contacts, the bottom electrodes of the capacitors, and the first level of interconnections. A thin film of sputtered silicon nitride is the dielectric for the capacitors. Another metal layer forms the second layer of interconnections and the top electrodes of the capacitors. As a last step, air bridges are formed on top of the capacitors to provide a third level of interconnections. Air bridges are more reliable and reproducible than wirebonds and are thus expected to contribute to a low cost, reproducible circuit fabrication. The circuits

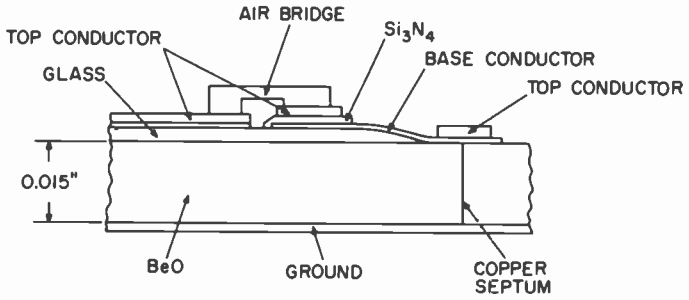

Fig. 2—Cross section of layered MBC structure.

are batch fabricated on substrates that are relatively low cost when compared to GaAs wafers.

An important factor in the fabrication of matching circuits is a high capacitor yield. Dielectric films are particularly sensitive to isolated defects protruding from an otherwise perfect surface. Low breakdown voltages and destruction of the capacitors result from the greatly increased electric field at these points. A substantial effort was therefore devoted to finding a suitable glaze that combines excellent surface properties with good definition and low rf loss. Si_3N_4 capacitors formed on this glaze show acceptable yield and good reproducibility.

Since the capacitor yield is greatly affected by the surface defect population, capacitors with larger areas are more prone to failures. This is apparent in the yield values for the Si_3N_4 capacitors. Small capacitors of approximately 6 mil^2 area (C = 0.3 pF) show yields of approximately 98%. For larger capacitors, in the order of 100 mil^2 (C = 5 pF), the yield decreases to 96%. Overall, the circuit yield is approximately 85%. This value reflects the relative early stage of this process technology and is expected to increase with further improvements in the glaze's surface quality and in the Si_3N_4 deposition process.

Experimental Results

The new miniature BeO circuit technology was applied to the fabrication of two types of microwave power amplifiers, a medium power, very high efficiency amplifier at X-band for satellite applications and a high-power Ku-band amplifier module for light-weight radar applications. That the examples given here were designed to operate at the high end of the microwave frequency range is a result only of momentary program needs. The technology is suited for a wide range of frequencies and actually becomes more advantageous at S- and L-band where size and volume savings would be even more pronounced.

X-band High Efficiency Amplifier

For most of today's space borne communications systems, travelling wave tubes together with reflector antennas are used as rf transmitters to ground. Recent advances in GaAs FETs offer the promise to replace this system with a large number of solid-state moderate power amplifiers that are directly integrated with the radiating elements of an active array antenna. The key requirements for such amplifiers are very light weight/small volume, very high efficiency, high reliability, and low fabrication cost.

The amplifier described here fulfills practically all of these objectives; it is a 12-GHz, 150-mW amplifier optimized for very high effi-

ciency operation and using the MBC technology, which results in very small size, good reproducibility, and the potential for large-volume batch fabrication. Fig. 3 shows a closeup of a single amplifier stage. The FET pellet, a 0.5 W MSC 88202 device, is mounted at the center of the H-shaped metal pattern grounded through the septum. The input and output tuning circuits are formed by short inductive lines, arranged in pairs, and by silicon nitride capacitors, connected to ground. These capacitors are connected to the circuit by means of short bond wires that eventually will be replaced by airbridge interconnections. By the selection of different capacitors, the center of the operating band can be tuned over approximately 1 GHz.

The amplifier was initially tuned for maximum gain based on small signal S-parameter measurements. A gain of 8.5 dB was obtained in this way at 12.4 GHz. To increase the available power output, both input and output matching networks had to be readjusted. Use of different size thin-film capacitors together with different bond wire lengths were used to change the transformation ratio between device and feedlines. The efficiency was optimized under the retuned condi-

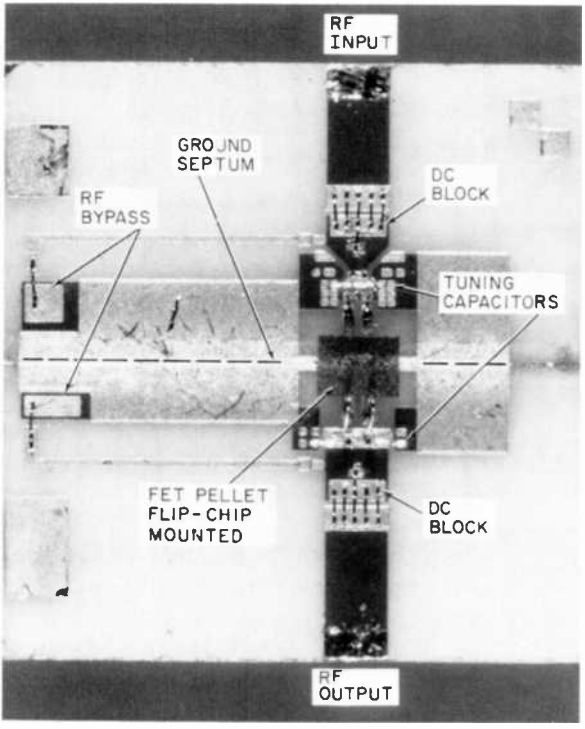

Fig. 3—12-GHz amplifier.

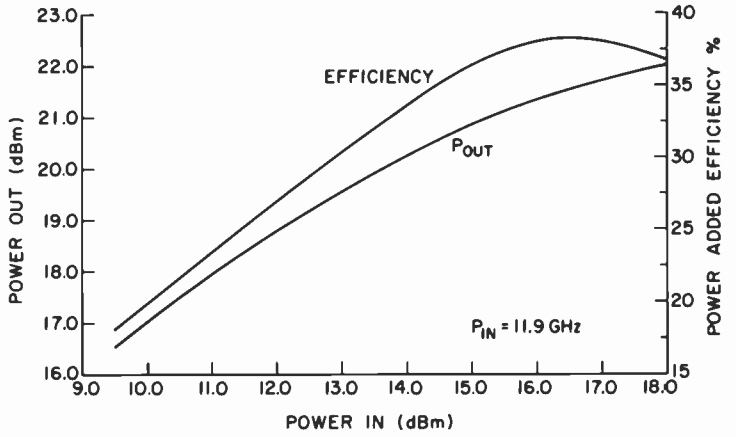

Fig. 4—Power performance of 12-GHz amplifier.

tions by varying the device bias voltages at various rf drive levels. To simplify the optimization procedure, extensive use was made of a computer aided efficiency optimization setup together with load-pull measurements. Fig. 4 shows the performance of the amplifier when adjusted for maximum efficiency at moderate power level. A power added efficiency of 38% was measured at a power output of 135 mW and a gain of 5.0 dB. These values include the losses of input and output connectors which at 12 GHz are in the order of 0.2 dB each. With direct integration of the amplifier with the antenna element, power added efficiencies in excess of 40% are well within the practical range using commercially available GaAs FETs in chip form. The MSC pellets are equipped with bumps on all three contacts and thus lend themselves readily to direct thermocompression mounting on the BeO carrier.

Because the FET is operated well below its maximum rated output and the heat sinking of the device is excellent, the operating temperature is very low and very long life expectancy is obtained. Preliminary data based on previous test results by MSC and temperature measurements on the device indicate an order of magnitude increase of the MTBF when operated at high efficiency and reduced power output compared to normal full-power operation. No effort has been devoted so far to optimizing the amplifier's bandwidth performance. Fig. 5 shows the measured results for the amplifier with a four-element input and two-element output matching network. Since, for communications applications, the bandwidth rarely exceeds 500 MHz in this frequency range, the present performance (1 dB bandwidth of 600 MHz) is close to being satisfactory.

Ku-band Power Amplifier

Another amplifier presently under development that uses the new beryllia based circuit technology is aimed at providing 1 W of power output over the frequency range from 16.0 to 16.5 GHz. This circuit, still in an early experimental stage, is more difficult to implement because the required device performance is at the limit of the state-of-the-art, and circuit losses and parasitics become more dominant at higher frequencies. Special efforts have thus been devoted to analyzing circuit losses and determining ways to achieve proper power sharing between multiple cells of the high power FET. Two types of devices are being considered for this amplifier: one is an RCA 16-gate, 4-cell FET with a nominal gate length of 1 μm, the other is the MSC 88204. Both devices have gate widths of approximately 2400 μm, have similar impedance levels, and are equipped with bumps for flip-chip mounting.

A photograph of a batch-processed strip of four circuits is shown in Fig. 6. The substrates are selectively glazed in the areas dedicated to thin-film matching circuits. The two center circuits have GaAs FET pellets mounted on the BeO in the unglazed section above the ground septum. The present size of a single amplifier circuit is 0.200 × 0.200 inches. Even though the circuit includes bias lines and dc bypass capacitors, it could be reduced further in size to approximately 1/8 × 1/8 inches without difficulty.

Fig. 7 shows a closeup of the Ku-band amplifier. Since the FET pellet is relatively large in transverse direction, proper sharing between individual cells presents a major problem. For instance, the lines of current circulating through the outer cells of the FET pellet enclose a

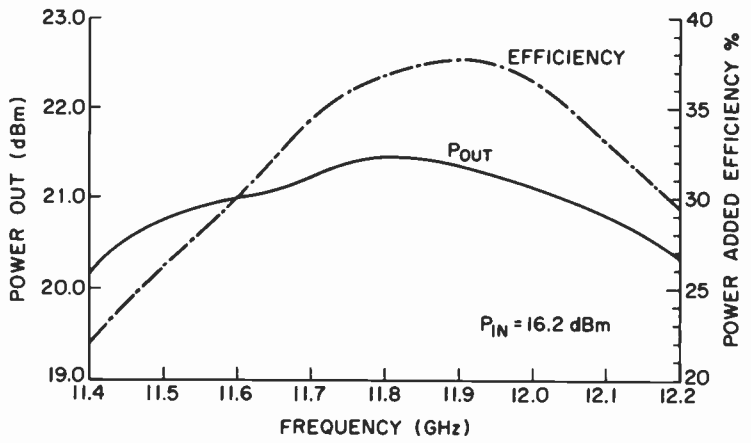

Fig. 5—Frequency response of 12-GHz amplifier.

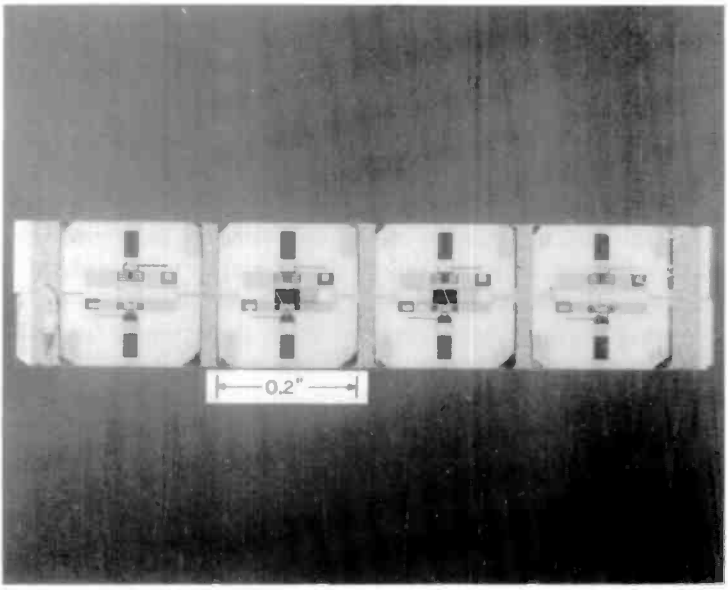

Fig. 6—Batch-fabricated strip of amplifiers.

smaller area than the lines circulating through the center cells. Therefore, the former have a lower associated inductance which results in detuning and an uneven impedance transformation. This effect has been counteracted by "necking down" the feedlines to the gate and

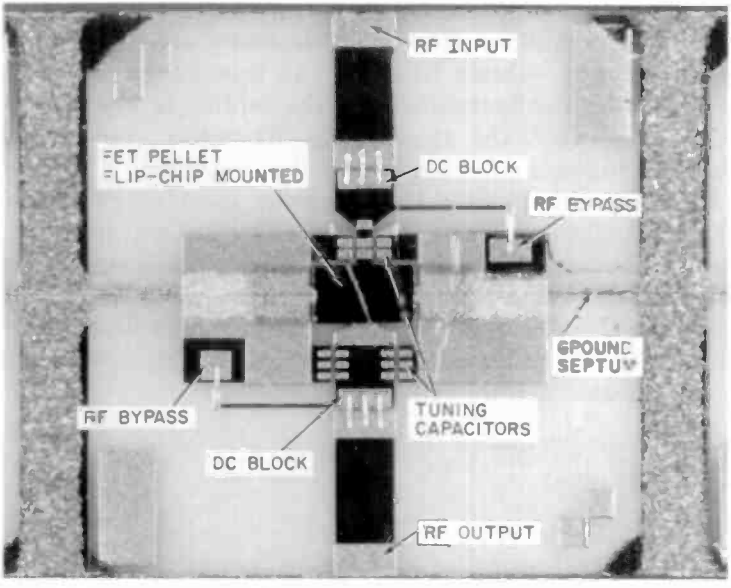

Fig. 7—16-GHz power amplifier.

collector contact pads in the area where the shunt capacitors are attached to ground. The tuning patterns for both the input and output matching are arranged in planar fashion on top of the BeO. The high reactive currents associated with the necessary large transformation ratios for power FETs thus remain on top and do not circulate through the ground septum. This reduces the normally existing negative feedback through the inductance of the septum and improves the gain. Also the tuning patterns are made symmetrical by using a shunt tuning capacitor on either side of the input and output lines.

The losses of the tuning circuits were determined using both a reflection and a transmission measurement technique. First, the reflection coefficient of a shorted tuning circuit was measured with the FET replaced by 5 short bond wires connected in parallel. A circuit computer model, which includes lossy elements, was then optimized to match the measured reflection coefficient under shorted-load conditions. Thus, the overall loss computed with this method under nominal loading conditions includes the ohmic losses in the inductors, in the capacitors, and in the septum. It also includes radiation losses that are present because of the large standing waves set up by the shorted load. Since radiation losses will be lower under normal operating conditions, this method indicates a total loss that exceeds the true value.

The other technique consisted of measuring the insertion loss of two identical circuits connected back to back. The loss of each circuit is simply one-half of the insertion loss of the combined structure. An attractive feature of this technique is that the circuits operate under nominal load conditions; thus radiation losses are representative of normal operation. Ohmic losses in the septum, however, are not included in this configuration since the septum is bypassed by the connection between the two circuits. Therefore the transmission method will indicate a loss lower than the true value.

A summary of the test results obtained at 16 GHz is shown in Table 1. The transmission and the reflection losses are listed for the input circuit, the output circuit, and for a low-loss control circuit designed for the same impedance transformation as the input circuit and built with a high-Q rutile capacitor and with inductive bond wires. The estimated true loss of the circuits is the average of the losses measured with transmission and the reflection methods.

Table 1—Comparison of Losses in Different Matching Circuits

	Loss (dB)		
Circuit	Trans.	Refl.	Estimated
Input	0.62	0.88	0.75
Output	0.40	0.45	0.42
Rutile Input	0.46	0.53	0.50

The input circuit, which is designed for a 50-to-1 impedance transformation ratio, shows a loss of 0.75 dB, a value 0.25 dB higher than the control. The estimated loss of the output circuit, designed for a 20-to-1 impedance transformation ratio, is 0.42 dB. These values of loss seem acceptable for the high transformation ratios, although an improvement of 0.2–0.3 dB should still be achievable with process improvements.

Conclusions

The new miniature BeO circuits technology offers excellent electrical and thermal properties for power amplifier applications, the possibility for batch processing of circuits separate from devices, and a very small circuit size that approaches that of the monolithic counterparts. The process is highly flexible which makes it suitable for small-to-moderate quantities at frequencies ranging from UHF to Ku-band. The fabrication and assembly processes involved are in principle well reproducible and hold great promise to become a low-cost production technology.

Initial experimental results illustrate the basic viability of this approach. A 12-GHz amplifier using commercially available FET pellets has shown a power output of 135 mW with a power-added efficiency of 38% and 5.0 dB of gain. The circuit portion for a 1-W, 16-GHz amplifier was developed and the high transformation ratio matching circuits showed reasonably low loss. Good yields have been demonstrated for lumped-element capacitances on glazed BeO.

Further work will be required in the flip-chip attachment of GaAs power FETs, which includes reshaping of the contact pads for best thermal conduction, ease of assembly, and high mounting strength.

Acknowledgment

The authors wish to acknowledge the contributions of G. Rolland, P. Jozwiak, and K. Lev in the fabrication and processing of the circuits, of P. Czajkowski, J. Brown, R. Marx, and J. Goldweber in the assembly and the rf measurement of the amplifiers, and of G. Filipsson (on leave from the National Research Insititute, Linköping, Sweden) for computer simulations of the microwave circuits.

References:

[1] J. Fawcette, "Competition Intensifies in Monolithic Gallium Arsenide," *Microwave System News*, p. 35, April 1979.
[2] R. Van Tuyl, "A Monolithic GaAs IC for Heterodyne Generation of RF Signals," *IEEE Trans.*, **ED 28**, p. 166, Feb. 1981.

[3] R. S. Pengelly, "GaAs Monolithic Microwave Circuits for Phased-Array Applications," *IEE Proc.*, **127**, pt.F, p. 301, Aug. 1980.
[4] P. Harrop, P. Lesartre, and A. Collet, "GaAs Integrated all FET Front-End at 12 GHz," *GaAs IC Symposium*, paper #28, Nov. 1980.
[5] E. Belohoubek, A. Presser, and H. Veloric, "Improved Circuit-Device Interface for Microwave Bipolar Power Transistors," *IEEE Trans.*, **SC-11**, p. 256, April 1976.
[6] J. M. Schellenberg and H. Yamasaki, "A New Approach to FET Power Amplifiers," *Microwave* J, p. 51, March 1982.

Interpreting The Beta Versus Collector Current and Temperature Characteristics of a Transistor

Robert Amantea
RCA Laboratories, Princeton, NJ 08540

Abstract—A tutorial discussion on the composition of beta in bipolar transistors is presented. The beta versus collector-current (β-I_c) characteristics are discussed in detail with particular emphasis on the structure of the characteristics and their dependence on temperature. Several graphical ways of viewing the β-I_c characteristics are presented, along with their interpretation and use.

Introduction

Beta, the ratio of the collector current to base current in a transistor, is intimately dependent upon the complex physical mechanisms that occur within the transistor. It also is relatively simple to measure beta with excellent accuracy and repeatibility. For these reasons, the beta-versus-collector-current characteristics are commonly used to analyze the behavior of transistors.

In this work, we first present a short tutorial discussion on the composition of beta. This is followed by a discussion of how the individual components of base current impact the β-I_c characteristics and their temperature dependence. Several graphical ways of viewing the β-I_c characteristics are presented, along with their interpretation and use. Definitions of the symbols used throughout the paper are given in Appendix 1.

The Definition of Beta

Beta is the ratio of collector current to base current at the external terminals of a transistor. Therefore, to characterize beta, each component of current that flows either into or out of these two terminals must be considered. In particular, we are interested in the case where the base–emitter junction is forward biased and the base–collector junction is reverse biased or in quasisaturation.

In a forward-biased junction, the *np* product is greater than n_i^2, therefore, carrier recombination takes place. In an *npn* transistor, the holes that recombine in the base–emitter space-charge region are supplied from the base region and, therefore, contribute a positive component to the net base current. This current component is termed I_{BRE}. Holes and electrons also recombine in the neutral base region, thereby giving rise to a positive base current component I_{BRN}. Holes also are injected across the base–emitter space-charge region into the emitter. These holes form the injected minority current from the base into the emitter, I_{BE}.

In a reverse-biased junction the *np* product is less than n_i^2, therefore carrier generation takes place. In an *npn* transistor, the electric field is in the direction from the collector toward the base, thereby forcing the holes into the base region. These holes give rise to a negative base current component, I_{BRC}.

These four base-current components make up the total base current. Note that the recombination terms also can include surface effects,[5] and in totality may be referred to as emitter–base leakage current. The total base current, I_B is

$$I_B = I_{BRE} + I_{BRN} - I_{BRC} + I_{BE}. \qquad [1]$$

The generation that takes place in the base–collector space-charge region produces an electron current equal to the hole current. The electron flux flows toward the collector, under the influence of the electric field, giving rise to a positive collector-current component equal in magnitude to I_{BRC}. This component also may include surface generation or conductance, and in totality may be referred to as collector–base leakage current. Electrons are injected from the emitter into the base region. These produce a current I_{EB}. A portion δ_T, of these electrons recombine in the neutral base region with the holes supplied by I_{BRN}. Therefore a negative component of collector current, equal in magnitude to I_{BRN} is created.

The net collector current is therefore

$$I_C = I_{EB} + I_{BRC} - I_{BRN}. \qquad [2]$$

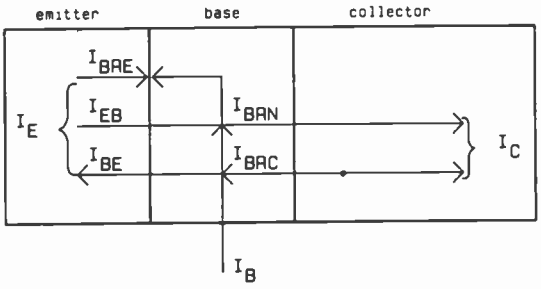

Fig. 1—Pictorial representation of the current components.

Thus beta is, by definition,

$$B = \frac{I_{EB} + I_{BRC} - I_{BRN}}{I_{BE} + I_{BRE} + I_{BRN} - I_{BRC}}. \quad [3]$$

A graphical summary of the above discussion is given in Fig. 1. The arrows point in the direction of carrier flow.

The Current Components

The emitter-base space-charge-region recombination current, I_{BRE}, varies with the base-emitter voltage according to

$$I_{BRE} = I_{BREO}\exp(qV_{be}/nkT) \quad [4]$$

where I_{BREO} and n are approximately constant. The diode-ideality factor n is usually between one and two. There have been a number of papers describing the relationships of I_{BREO} and n to the physical structure of the diode. For example, Sah, Noyce, and Shockley[1] present a derivation that shows that this current component arises from Shockley-Read-Hall[2, 3] recombination occurring in the space-charge region. Buckingham and Faulkner[4] go on to describe a localized trap theory that accounts for the relative invariance of n over large ranges of current. In any event, it is generally agreed that this component of current is caused by Shockley-Read-Hall recombination in the emitter-base space-charge region in deep recombination centers, i.e., centers near the center of the band-gap in energy. This recombination may occur in both the bulk silicon and at the surface.

The kind of contaminants that can give rise to these deep recombination centers are iron, nickel, copper, gold, and other metallic species. Therefore, the presence of this current component usually indicates the presence of some deep-level contaminant.

The hole current injected into the emitter from the base, I_{BE}, varies with base-emitter voltage according to

$$I_{BE} = I_{BEO}\exp(qV_{be}/kT). \qquad [5]$$

This current component arises from the normal injection process, therefore I_{BE} is dependent upon the doping and geometry of the emitter region. The coefficient I_{BEO} is characterized by the generalized Moll-Ross relation[6]

$$I_{BEO} = \frac{qA}{\int_0^{x_e} [N(x)/D_p n_{ie}^2]\, dx}. \qquad [6]$$

Its temperature dependence comes about from the temperature dependence of the diffusion constant and the effective intrinsic-carrier density. The only control we have over I_{BEO} is through changes in the impurity concentration profile.

The base recombination current component, I_{BRN}, is proportional to the number of minority carriers in the neutral base region and, therefore, to the current injected from the emitter into the base I_{EB}. This current arises from the normal injection process and is described by

$$I_{EB} = \frac{qA\exp(qV_{be}/kT)}{\int_{x_b}^{x_c} [N(x)/D_n n_{ie}^2]\, dx}. \qquad [7]$$

The collector leakage current can arise from several possible sources. The three most important cases are generation current in the collector-base depletion layer, avalanche multiplication, and resistive surface currents. At low voltages, avalanche multiplication can be ruled out. As we shall see, temperature measurements can identify whether bulk generation or surface leakage occurs.

The β-I_c Curves

Fig. 2 shows two plots of $\log_{10}\beta$ versus $\log_{10}I_c$ taken at room temperature. They are for the same type of device (i.e., the same geometry and impurity profile) except for two things: the LCE device has a lower impurity concentration in the emitter, and gettering has been used to reduce the effects of defects. Note that there are several differences between these graphs. Of particular importance are the flatness with respect to current and the high value of beta for the LCE device as

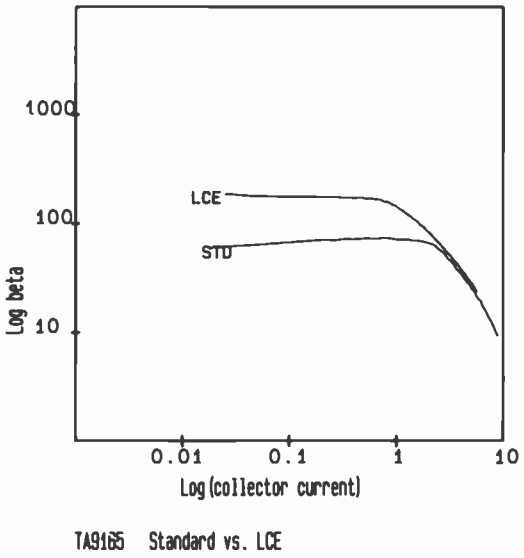

Fig. 2—β-I_c curves for a standard transistor and one with a low-concentration emitter region.

compared to the standard device. These differences are a direct result of the low-concentration emitter region and the gettering process.

To help us understand these differences better, we show in Fig. 3 a series of β-I_c curves taken for the standard device with temperatures ranging from −50°C to +150°C in 25°C steps. The lowest curve is at −50°C. At low temperature and low current, the β-I_c curves show a positive slope. This slope results from I_{BRE}. To see this, consider beta in this region of current and temperature,

$$\beta = \frac{(1 - \delta_T) I_{EBO} \exp(qV_{be}/kT)}{I_{BREO} \exp(qV_{be}/nkT) + (I_{BEO} + \delta_T I_{EBO}) \exp(qV_{be}/kT)}. \quad [8]$$

This expression can be rearranged by dividing through by the second term in the denominator and using

$$I_c = (1 - \delta_T) I_{EBO} \exp(qV_{be}/kt). \quad [9]$$

The results are

$$\beta = \frac{(1 - \delta_T) I_{EBO}/(I_{BEO} + \delta_T I_{EBO})}{(I_{BREO}/(I_{BEO} + \delta_T I_{EBO}))(I_c/(1 - \delta_T) I_{EBO})^{(1/n)-1} + 1}. \quad [10]$$

Since the ideality factor, n, is always greater than unity, the first term in the denominator dominates unity at low current. Thus, at low

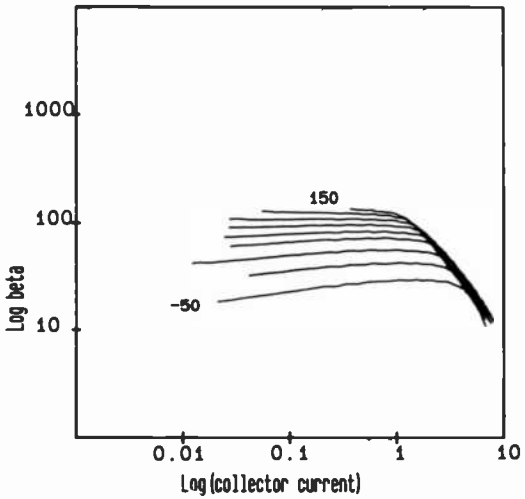

Fig. 3—β-I_c for standard transistor with temperature as a parameter.

currents

$$\beta \propto I_c^{1-(1/n)}, \qquad [11]$$

or

$$\log_{10}(\beta) \propto [1-(1/n)]\log_{10} I_c. \qquad [12]$$

This result shows that the slope of the β-I_c curve at low current is asymptotic to $1-(1/n)$.

Fig. 4 shows a plot of n versus $1/T$ for the device shown in Fig. 3. Note how n decreases toward unity as temperature increases. This behavior arises because I_{BREO} tends to vary as n_i, while I_{BEO} and I_{EBO} vary as n_i^2. Therefore, the coefficient of the $I_c^{(1/n)-1}$ term varies as $n_i^{1-(2/n)}$, which is decreasing with temperature for $n < 2$. Thus, as temperature increases, the $I_c^{(1/n)-1}$ term becomes less and less important. One indication of the quality of a device, with respect to defects, is the temperature at which n becomes unity, since this is proportional to the magnitude of I_{BREO}. A lower temperature at which $n = 1$ indicates a better device.

Fig. 5 shows the β-I_c curves for the LCE-gettered device. In this case, the ideality factor n is unity for all temperatures, thus indicating the relative absence of defects.

One way of isolating the different mechanisms that affect β is to plot $\log_{10}\beta$ versus $1/T$ as shown in Fig. 6. Here we have plotted the results for the standard TA9165 devices. The curve is nearly linear with a small amount of downward curvature at low temperatures. This implies that β is nearly proportional to $\exp(-c/T)$, where the param-

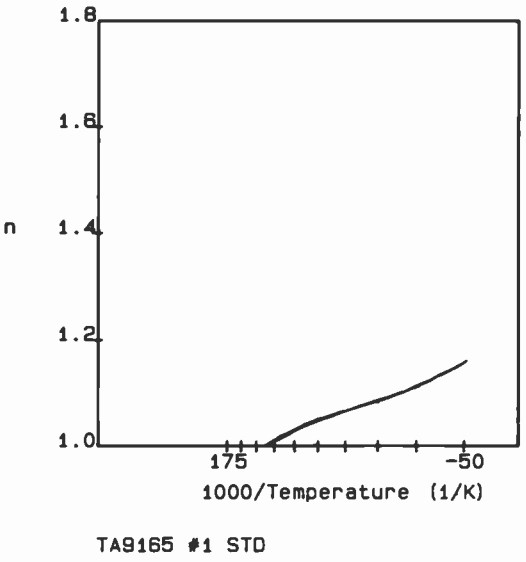

Fig. 4—The diode-ideality factor versus $1/T$.

eter c is a constant. If there were negligible emitter–base and collector–base leakage currents and the device were operated in the active mode, then this plot would be a straight line, as shown in Fig. 7 where we have plotted $\log_{10}\beta$ versus $1/T$ for the LCE device.

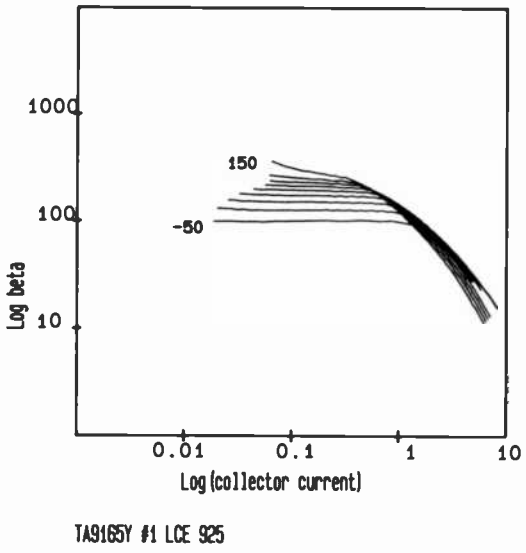

Fig. 5—β-I_c for LCE transistor with temperature as a parameter.

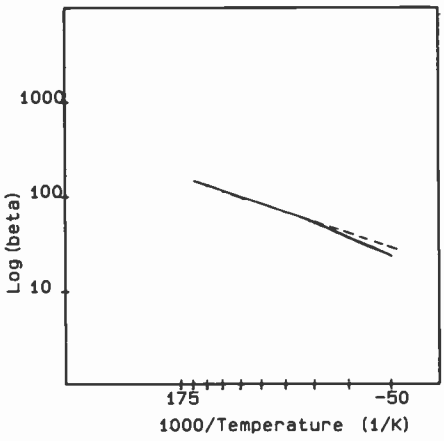

Fig. 6—$\text{Log}_{10}(\beta)$ versus $1/T$, standard transistor.

The mechanism that is generally held responsible for this temperature dependence of beta is band-gap shrinkage in the emitter region due to heavy doping.[7] From the equations for I_c and I_B when leakage and recombination currents are neglected, we find

$$\beta = \frac{\int_0^{x_e} [N(x)/D_p n_{ie}^2]\, dx}{\int_{x_b}^{x_c} [N(x)/D_n n_{ie}^2]\, dx}. \qquad [13]$$

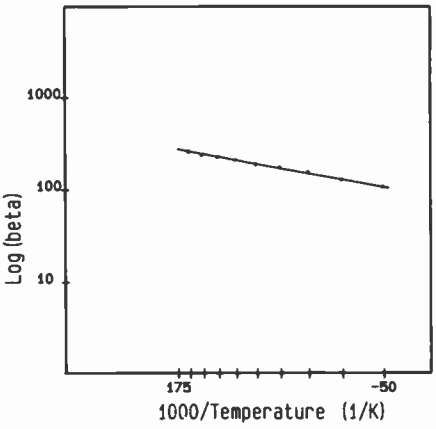

Fig. 7—$\text{Log}_{10}(\beta)$ versus $1/T$, LCE transistor.

From these equations we find that β is proportional to the ratio of the averaged effective intrinsic-carrier density in the base to that in the emitter. Since the temperature dependence of D_p and D_n cancel and

$$n_{ie}^2 = N_c N_v \exp(-E_g/kT), \qquad [14]$$

we find

$$\beta \propto \exp((\hat{E}_{ge} - \hat{E}_{gb})/kT), \qquad [15]$$

where $\hat{E}_{ge}$ and $\hat{E}_{gb}$ are the effective band-gap energy in the emitter and base region. Since the band-gap shrinks only as impurity concentration rises well above 10^{17} cm^{-3}, the amount of shrinkage in the base is usually negligible[8]. However in the emitter region it can be substantial.

From these relationships we find that $d\log_{10}(\beta)/d(1/T) = \Delta\hat{E}_g/k\log_e 10)$. Thus the linear slope of the curves in Figs. 6 and 7 is proportional to the effective band-gap shrinkage in the emitter. For the two devices shown we find ΔE_g is approximately 75 and 36 meV in the standard and LCE device, respectively. These magnitudes are consistent with those found in the literature.

To understand the temperature dependence of a bipolar transistor when it is in quasi-saturation we must understand the dependence of the forward transit time τ_F on collector current, since β is proportional to $(1 + \tau_F I_c/Q_{B0})$.[9] Three physical mechanisms dominate the behavior of τ_F with collector current: conductivity modulation in the base region, base widening,[10, 11] and two-dimensional current spreading in the collector region. Each of these mechanisms causes τ_F to increase with increasing collector current. Furthermore, the temperature dependences of these mechanisms are such that they cause τ_F to increase with increasing temperature.

At low current, the forward transit time is given approximately by

$$\tau_F = w_B^2/\eta D, \qquad [16]$$

where η is a constant, greater than 2, that is determined by the amount of built-in electric field in the base region due to the logarithmic gradient in the impurity profile.[12] As current rises, the minority-carrier density in the base region rises. As the minority-carrier density approaches the background concentration, η begins to fall and eventually goes to 4 when the carrier density is well in excess of the background concentration.

At very high currents, the forward transit time is given approximately by

$$\tau_F = (w_B + \Delta w)^2/4D, \qquad [17]$$

where Δw is the distance that the base has moved into the collector due to the base-widening effect. Unfortunately, the transition from the

low-current formula to the high-current formula is not easily expressed quantitatively. Furthermore, the high-current formula needs modification due to current spreading in the collector region. However, in each case we note that τ_F is inversely proportional to a diffusion constant. Since the diffusion constant varies with temperature approximately as $T^{-1.5}$, the transit time varies at least as $T^{1.5}$.

The amount of base widening can be estimated by considering the ohmic voltage drop across the collector region, which is held fixed during the measurement at approximately the applied collector–emitter voltage, V_c. If the collector is uniformly doped and has resistivity ρ and thickness w_c, then by Ohm's law

$$I_c \rho w_c / A_c = V_c. \qquad [18]$$

This determines the approximate current, I_c, at which quasi-saturation begins. For currents exceeding this critical current, the resistive collector width must be reduced by Δw, so that

$$I\rho(w_c - \Delta w)/\mathrm{A}_c = V_c. \qquad [19]$$

Thus,

$$\Delta w = w_c - V_c A_c / \rho I. \qquad [20]$$

As temperature increases, resistivity increases, thereby causing Δw to increase and finally causing τ_F to increase. Thus, this mechanism adds to the temperature dependence of τ_F.

The net effect of quasi-saturation is to produce a large negative temperature coefficient for beta, as illustrated in Fig. 5, at high currents (i.e., for this particular device $I_c > 1$ ampere). These particular curves also have the band-gap shrinkage effect built into them, which partially cancels the negative temperature coefficient due to τ_F. To observe quasi-saturation effects independently of the band-gap shrinkage effect, we plot log(beta) normalized to its peak value.

Fig. 8 shows a plot of log(beta) versus log(collector current) with beta normalized to its peak value at each temperature. In the case where collector–base leakage plays a role, the normalization is to beta at 0.1 amperes. Comparing these curves with those drawn in the conventional way (Fig. 5), we see that the temperature dependence due to band-gap shrinkage has been eliminated leaving only the temperature dependence due to quasi-saturation.

The effect of removing the band-gap shrinkage mechanism is shown in Fig. 9 where we have plotted $\log_{10}\beta$ versus $1/T$ for the device TA9165Y #1 at $I_c = 3.16$ amperes from both Figs. 5 and 8. The lower curve shows the temperature effects of quasi-saturation, while the upper curve shows the effects of both quasi-saturation and band-gap shrinkage. The numerical difference between these two curves is a

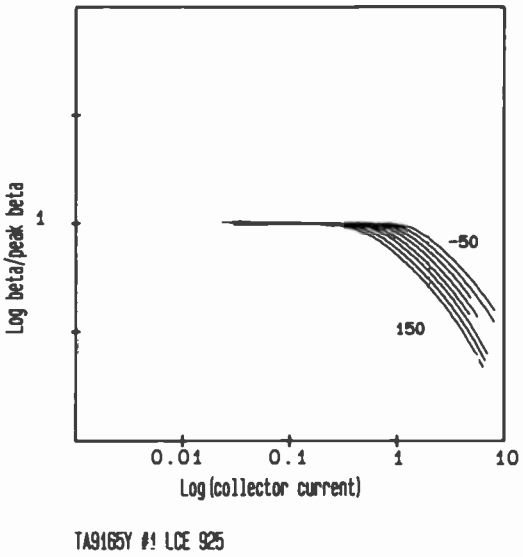

Fig. 8—$\text{Log}_{10}(\beta/\beta_{pk})$ versus $\log_{10}$, LCE transistor.

straight line with a slope equal to that obtained at low currents, thereby showing that the band-gap shrinkage effect is active at an equal level at both high and low currents.

Since the diffusion coefficient and resistivity vary as a power law with temperature, we replot in Fig. 10 the lower curve in Fig. 9 as $\log_{10}(\beta)$ versus $\log_{10}(T)$. As expected, the results are nearly a straight

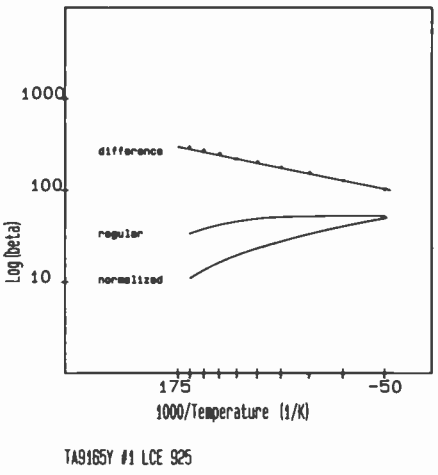

Fig. 9—A comparison $\log_{10}(\beta)$ versus $1/T$ and $\log_{10}(\beta/\beta_{pk})$ versus $1/T$ for the LCE transistor.

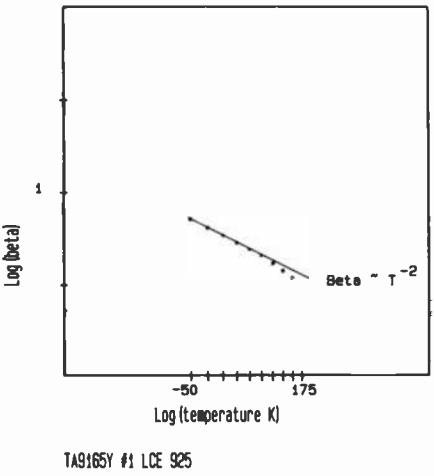

Fig. 10—$\text{Log}_{10}(\beta/\beta_{pk})$ versus $\log_{10} T$ for LCE transistor in quasi-saturation.

line; however, at the higher temperatures, some downward curvature appears. This curvature probably comes about because the temperature dependencies of the diffusion constant and resistivity occur simultaneously.

Applications

For low-current applications, the essential problem is to eliminate both collector-base and emitter-base leakage currents. By proper gettering techniques, the point defects that cause the emitter-base bulk leakage current can be effectively removed. For example, the LCE device shown in Fig. 5 has flat beta down to 1.0 μA collector current at room temperature. A good part of the collector-base leakage current can be removed by proper surface passivation; however, the bulk generation current is band-to-band generation and cannot be affected.

For high-current applications, there is a need to minimize the temperature coefficient of β while increasing the knee current at which the β fall off begins. If the band-gap shrinkage effect is removed completely, as simulated in Fig. 8, then at high currents, β has a large negative temperature coefficient which gives the device high resistance to forward second breakdown. To increase the knee current, the base charge Q_{Bo} can be increased as much as possible until emitter efficiency is adversely affected. This, of course is dependent on the effective emitter charge Q_{Eo}, which depends on the amount of band-gap shrink-

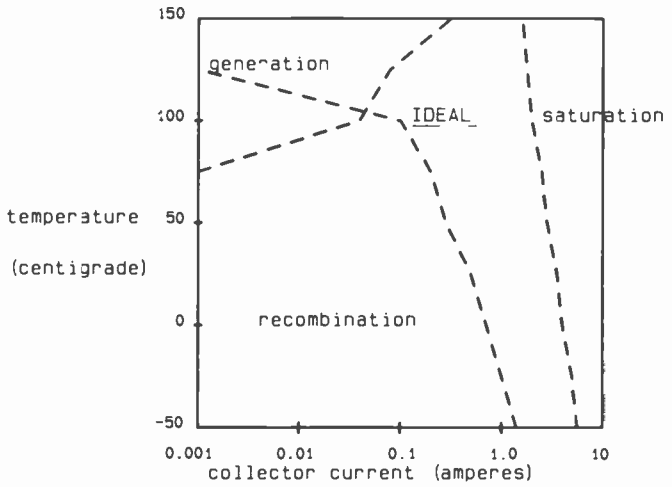

Fig. 11—β in the current-temperature plane for a standard device.

age and the emitter-region lifetime.[13] Depending on the desired peak beta, there is a relatively flat optimum relating Q_{Bo}, Q_{Eo}, β.

The above discussion is summarized graphically in Fig. 11. In this figure we plot, for a standard device, contours in the current-temperature plane, where the contours determine the onset of the region where β deviates from its desired value. In the case of high currents, β falls off; at low current and low temperature β falls off; and at low current and high temperature β rises. The ideal goal is to remove these contours from the domain of interest or, lacking this possibility, at least to squeeze them into the corners, as in Fig. 12 where a lightly doped, gettered device is shown.

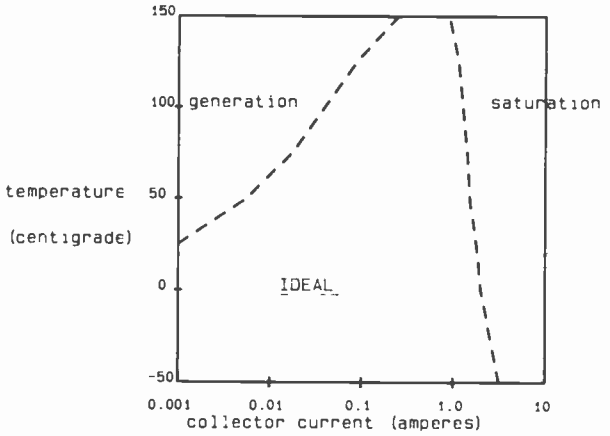

Fig. 12—β in the current-temperature plane for an LCE device.

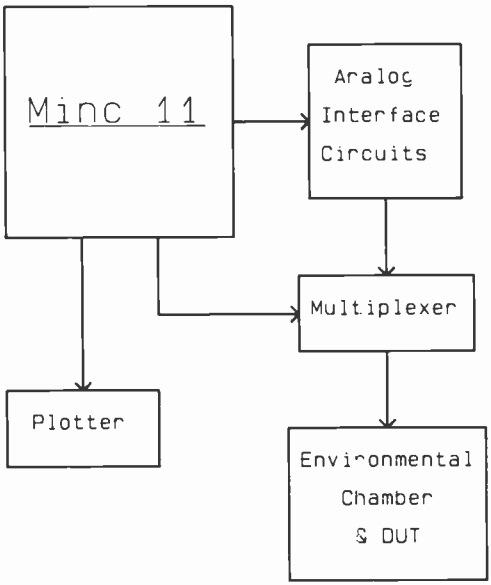

Fig. 13—Block diagram of automatic test system.

Measurements

The large quantity of data necessary for the analysis in this work is made managable by using automated data acquisition to measure the devices and process the data. A block design of the system is shown in Fig. 13. A Digital Equipment MINC 11 Laboratory system is used as the system controller. The analog-interface circuits scale applied and measured voltages and currents so that a wide variety of devices can be measured with the same system. Multiplexing is included, so that a group of devices (usually 6 to 10) can be measured at the same time and the variability of the data with respect to devices of the same type may be estimated.

Software has been developed to present the data in the many different ways shown in this report. All the figures in this work were created in this manner.

Appendix I: Symbols

Terminal Quantities:

I_c = collector current
I_B = base current
V_{be} = base-emitter voltage
V_c = collector voltage

Current Components:

I_{BE} = current injected from the base into the emitter
I_{EB} = current injected from the emitter into the base
I_{BRE} = recombination current in the emitter–base space-charge region
I_{BRC} = generation current in the base–collector space–charge region
I_{BRN} = recombination current in the neutral–base region

Diode-Law Components:

n = diode ideality factor, $1 < n < 2$
q = electronic charge, 1.062×10^{-19} coul.
k = Boltzmann's constant, $8.62 \times 10^{-5}\ eV/°K$
T = temperature (Kelvin)

Geometrical Parameters:

x_c = position of the emitter edge of the base–emitter space-charge region
x_b = position of the base edge of the base–emitter space-charge region
x_c = position of the base edge of the collector–base space-charge region
w_B = base width $(x_c - x_b)$
w_c = width of the high resistivity portion of the collector region
A = emitter area
A_c = effective collector area

Physical Parameters:

n_i = intrinsic carrier density
n_{ie} = effective intrinsic carrier density
N_c = conduction–band density of states
N_v = valence–band density of states
D = diffusion constant
D_n = diffusion constant of electrons in p-type silicon
D_p = diffusion constant of holes in n-type silicon
E_g = band–gap
$\hat{E}_{gb}$ = effective band–gap in the base region
$\hat{E}_{ge}$ = effective band–gap in the emitter region

References:

[1] C. T. Sah, R. N. Noyce, and W. Shockley, "Carrier Generation and Recombination in *p-n* Junctions and *p-n* Junction Characteristics", *Proc. IRE*, **45**, p. 1228, Sept. 1957.
[2] W. Shockley and W. T. Read, "Statistics of the recombinations of holes and electrons", *Phys. Rev.*, **87**, p. 835, Sept. 1952.
[3] R. N. Hall, "Electron-Hole Recombination in Germanium", *Phys. Rev.*, **87**, p. 387, July 1952.

[4] M. J. Buckingham and E. A. Faulkner, "On the Theory of Logarithmic Silicon Diodes", *The Radio and Electronic Engineer*, **38,** No. 1, July 1969.
[5] C. T. Sah, "Effect of Surface Recombination and Channel on *p-n* Junction and Transistor Characteristics", *IRE Trans. ED*, p. 94, Jan. 1962.
[6] H. J. J. DeMan, "The Influence of Heavy Doping on the Emitter Efficiency of a Bipolar Transistor", *IEEE Trans. ED*, **18,** No. 10, p. 833, Oct. 1971.
[7] D. Buchanan, "Investigation of Current Gain Temperature Dependence in Silicon Transistors", *IEEE Trans. ED*, **16,** No. 1, 1969.
[8] J. W. Slotboon and H. C. DeGraaf, "Measurement of Bandgap Narrowing in Silicon Bipolar Transistors", *Solid State Electron*, **19,** p. 857, 1976.
[9] S. K. Ghandi, *Semiconductor Power Devices*, John Wiley, p. 157 (1977).
[10] C. T. Kirk, "A Theory of Transistor Cutoff Frequency (f_T) Fall-Off at High Current", *IRE Trans ED*, **ED-9,** p. 164, 1962.
[11] R. J. Whittier and D. A. Tremere, "Current Gain and Cutoff Frequency Fall Off at High Current", *IEEE Trans. ED*, **16,** No. 1, p. 39, 1969.
[12] R. S. Muller and T. I. Kamins, *Device Electronics for Integrated Circuits*, John Wiley, p. 262 (1977).
[13] R. Amantea, "A New Solution for Minority-Carrier Injection into the Emitter of a Bipolar Transistor", *IEEE Trans. ED*, **27,** p. 1231, 1980.

Positive and Negative Tone Near-Contact Printing of Contact Hole Maskings

Lawrence K. White

RCA Laboratories, Princeton, NJ 08450

Abstract—Near-contact (proximity) lithographic printers offer an inexpensive, low maintenance, high thruput method for noncontact printing. The imaging capability of these printers is limited by diffraction-induced exposure variation. In this work, the diffraction-induced imaging distortions for contact hole maskings are examined in detail. Using the Fresnel approximation and Babinet's principle, contact hole imaging limitations in the negative and positive tone are presented. A single imaging parameter, $\Delta_v = d\sqrt{2/\lambda g}$, is sufficient to characterize the diffraction pattern. Here, d is the square mask feature dimension, λ is the effective wavelength of resist exposure, and g is the print gap. The effects of polychromatic light sources, deep-UV exposure, mask and wafer flatness deviations, and the coherence of the light source are also presented for proximity lithography. Similar considerations are operative for high resolution (<2 μm) contact printing with thick resist coatings (>1 μm).

1. Introduction

The advent of improved near-contact (proximity) printers has produced a relative inexpensive, low maintenance, high throughput, noncontact photolithographic technique.[1-3] More reliable gapping mechanisms and the use of a fly's eye lens to produce more uniform exposure across a wafer are primarily responsible for the improved performance of these printers. Although proximity printing is not a prime candidate for VLSI manufacture, it may have useful applications for near-term, noncontact photolithographic requirements.

Contact hole maskings present some of the most demanding imaging requirements for lithographic printers. In this paper the imaging of contact hole maskings is examined in detail for near-contact printers. Isolated square aperture and square shadow maskings are analysed for positive and negative tone contact hole printing, respectively. Aerial images produced from the diffraction of actinic radiation as it passes through mask apertures are numerically computed and then compared with the corresponding resist image. The aerial image computations are done with the aid of the Fresnel approximation and Babinet's principle.

The resist type, the nature of the UV actinic light source, and the proximity gap setting can alter the image transfer process to the resist significantly. Portions of this study address these points, including effects of deep-UV exposure, polychromatic light sources, and wafer flatness. Our aerial image calculations provide insights into expected imaging features for new resists, light sources and variable mask dimensions. This analysis is also relevant for high resolution contact-printing with thick resist films. Although only flat surfaces are considered in detail here, the ramifications of proximity printing on topological features are discussed briefly.

2. Experiment

Our near-contact printing experiments were done on a Canon PLA 500F proximity printer. The HPR 204 resist system was used.[4] A conventional mercury vapor light source was employed without any intervening filters. A mask having various dimensional square contact hole maskings exposed resist images onto three-inch bulk silicon wafers.

All calculations were done on a time-shared computer system. The IMSL subroutine DCADRE was employed to calculate Fresnel integrals.[5] The PLOT3D subroutine developed by A. W. Jessup of RCA Laboratories[6] was used to display the relative intensity data on the scope-printer.

In theory, wave amplitudes and intensities can be computed for any shaped aperture, or shadow, but we considered only square mask features. Conveniently, computation of the integrals defining the amplitude of the diffracted light waves have been done for this shape aperture.[7-9] Contact holes are one of the more critical lithographic levels for proximity printing of ICs. An intuitive leap is required for a comparison between the theoretical diffraction pattern and the actual observed resist image. The development and response characteristics of the resist are important. A completely rigorous treatment requires models of the etching of the resist image during the development

process, since the exposure latitude of the resist, the nature of the function group conversions, and the size of sensitizer and resin molecules provide some inherent smoothing of exposure variations. Despite these considerations, major features of the resist image can be translated into rather gross differences in resist exposure without a detailed treatment of the development or photoreaction processes.

Our comparisons of computed diffraction patterns with experimental resist images are all made with assumed correlation between the degree of resist exposure and the final developed image. For a positive-tone resist this means that overexposed regions have excessive amounts of resist removed and underexposed regions have resist left behind. Negative-tone resists behave conversely, i.e., exposed regions of the resist are left behind and unexposed regions of the resist are removed.

3. Fresnel Diffraction Calculations

Other workers[10, 11] have pointed out that near-contact printing phenomena can be treated with the Fresnel diffraction approximation. Diffraction patterns are computed for the entire region and for the periphery region using the Fresnel approximation. A brief description of the approximation is discussed below. More detailed descriptions can be found elsewhere.[7-9]

The Fresnel approximation can be derived from the Kirchoff integral, assuming some additional conditions. The distance between the mask and the light source (r_{10}) is assumed to be large. The spacing between the mask and wafer (r_{20}) is assumed to be much larger than the aperture dimensions. This later assumption makes it possible to set the obliquity factor equal to two and to further simplify the Kirchhoff integral. The Kirchhoff integral from which the Fresnel approximation can be derived is represented by:

$$\mu(P) = \frac{-2ikA}{4\pi} \int_{y_1}^{y_2} \int_{x_1}^{x_2} \left[\cos(n, r_{20}) - \cos(n, r_{10}) \right] \frac{e^{ik(r_{10}+r_{20})}}{r_{10}r_{20}} \, dx \, dy,$$

where $\mu(P)$ equals the amplitude of the wave at a point P in the image plane; r_{10} is the distance between the source and the mask; r_{20} is the distance between the aperture and the image plane; k, the transmission constant, is set equal to $2\pi/\lambda$; A is the amplitude of the undiffracted wave and λ its wavelength. The term $[\cos(n, r_{20}) - \cos(n, r_{10})]$ represents the obliquity factor. The integration is done over the entire aperture as it is defined with respect to the coordinates of the viewpoint. Here the aperture is represented by an $x - y$ coordinate system. The Kirchhoff integral assumes a coherent light source and no edge effects at the masks. The latter assumption means that mask reflec-

tions and electric field effects at the mask surface are negligible. Reflections from the substrate are also neglected in this analysis.

In practice, the condition that r_{20} (the print gap) be much larger than the mask dimensions is not entirely true. However, calculations employing the Kirchoff double-integral without this simplifying assumption show only insignifcant changes in the computed diffraction patterns.[20] Apparently, the mathematics are quite forgiving for Fresnel-type calculations employing this approximation.

With the use of the simplifying assumptions, the amplitude of the wave at a poin, P, in the image plane for a square aperture is

$$\mu(P) = \frac{-i\mu_o}{2}\{[C(\xi_2) - C(\xi_1)]$$

$$+ i[S(\xi_2) - S(\xi_1)]\}\{[C(\eta_2) - C(\eta_1)] + i[S(\eta_2) - S(\eta_1)]\}.$$

μ_0 is the amplitude of the undiffracted wave, and C and S represent Fresnel integrals given by

$$C(\nu) = \int_0^{\nu} \cos\frac{\pi t^2}{2}\,dt \quad \text{and} \quad S(\nu) = \int_0^{\nu} \sin\frac{\pi t^2}{2}\,dt.$$

ξ_2 and ξ_1 and η_2 and η_1 are the integration limits related to the aperture dimension with respect to the viewpoint in the image plane. ξs take the form $x\sqrt{2/\lambda r_{20}}$, and similarly ηs take the form $y\sqrt{2/\lambda r_{20}}$. The resulting relative intensity at point P in the image plane is obtained by squaring the amplitude $\mu(P)$. The integration limits, $\Delta\nu$, define the total diffraction pattern and provide a means of relating the diffraction pattern to wavelength, aperture dimension, and printing gap; where $\Delta\nu$ equals $d\sqrt{2/\lambda g}$, and d represents the dimension of a side of the square aperture, λ the effective wavelength of exposure, and g the print gap r_{20}.

The Fresnel integrals employed to calculate diffraction patterns for square apertures are also used to calculate diffraction patterns for square shadows. To convert the Fresnel integrals into the correct wave amplitudes for the shadowed region, Babinet's principle is used. The amplitude of the diffracted wave under the mask shadow is given by

$$\mu^s(P) = \mu^0(P) - \mu^A(P),$$

where, $\mu^s(P)$ equals the amplitude of the wave under the shadow, $\mu^0(P)$ the amplitude of the undiffracted wave, and $\mu^A(P)$ the amplitude of wave under the correspondingly dimensioned aperture. Thus, for squared shadows, the intensity at a point P in the image plane is given by

$$I(P) = \tfrac{1}{4}[4.0 + A^2C^2 + A^2D^2 + B^2C^2 + B^2D^2 - 4AD - 4BC].$$

Here

$$A = C(\xi_2) - C(\xi_1)$$

$$B = S(\xi_2) - S(\xi_1)$$

$$C = C(\eta_2) - C(\eta_1)$$

$$D = S(\eta_2) - S(\eta_1).$$

The beauty of the $\Delta\nu$ parameter for predicting the nature of the diffraction patterns should be emphasized. A computed $\Delta\nu$ value produces the same diffraction pattern no matter what the individual values of the aperture dimension, wavelength, or printing gap may be. The nature of diffraction effects for smaller dimensioned apertures, shorter wavelengths, and varied gap settings can be predicted to some degree from results obtained at other wavelengths and gap and aperture dimensions provided the $\Delta\nu$ value is the same. It is sufficient to compute diffraction patterns only as a function of $\Delta\nu$. The actual resist images, however, may be somewhat more complex, since the response range of resists usually include multiple wavelengths and other conditions assumed for these calculations may not always be precisely met.

4. Resist Response Characteristics

Before we attempt to correlate these computed diffraction patterns with actual experimental developed resist images, it is useful to examine just how resists are exposed in terms of their response characteristics. Fig. 1 is a schematic of the wavelength output of a conventional high-pressure mercury light source. The most intense line is at 365 nm. Superimposed on this graph are the response characteristics of typical negative-acting and positive-acting resists. The response of the negative resist is centered on the 365-nm line, and very little resist is actually exposed at other wavelengths. Thus, diffraction calculations employing a single wavelength should be sufficient to describe the resist imaging.

The case for a positive resist is somewhat more complex. Three main peaks of the mercury emission spectrum are covered by the response range of the resist (365, 405, and 436 nm). Several wavelengths expose the resist, and a complete treatment of the exposure pattern must add together the diffraction pattern for every wavelength. Since the diffraction intensity nodes occur in different locations as a function of wavelength, relative exposure differences in the resist are smoothed to some degree for the positive resist.

The imaging of most conventional negative resists is dominated by

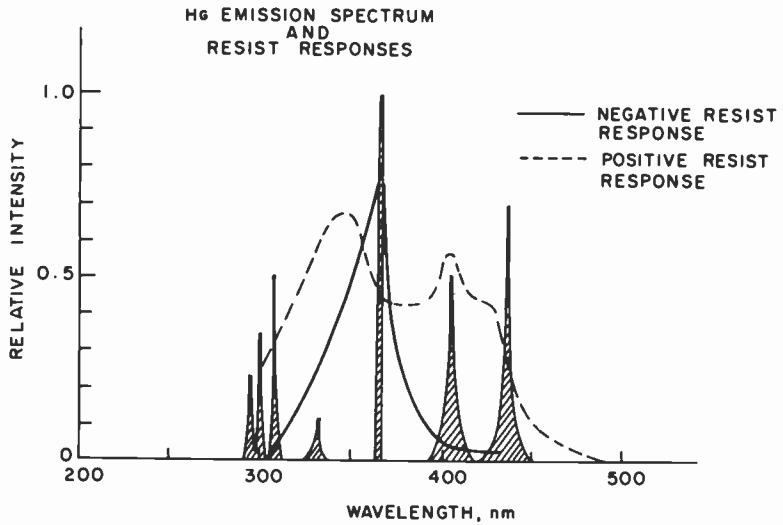

Fig. 1—Mercury vapor lamp emission spectrum and resist responses.

the single diffraction pattern associated with the 365-nm wavelength and very little smoothing actually occurs for such exposure. Some proximity printers have special filters that reduce the intensity of the 365-nm mercury line, so that other wavelengths can contribute to the exposure of the negative resist. This method does produce some smoothing of the diffraction pattern, but at great expense to resist speed. A more satisfying solution to correct the distortions produced by negative resists is to employ negative resists that have a wider response range and to expose the resist with a polychromatic light source.

For positive resist contact holes, comparisons with experimental resist images are easier than would appear, even though several actinic wavelengths must be considered. Our experiments show that only the shape of the perimeter of the resist image need be considered. Since longer wavelength exposures tend to concentrate more intensity closer to the center of the aperture, the perimeter exposure and resolution of the resist image are determined primarily by the lowest wavelengths effectively exposing the resist. Thus, the major features of the positive resist image can be predicted using the 365-nm wavelength. This approximation assumes the use of normal glass masks and a high-pressure mercury light source.

5. Positive-Tone Contact Holes

Diffraction patterns for various $\Delta\nu$ imaging setting are displayed in Figs. 2 & 3. To relate these patterns more easily to IC device design-

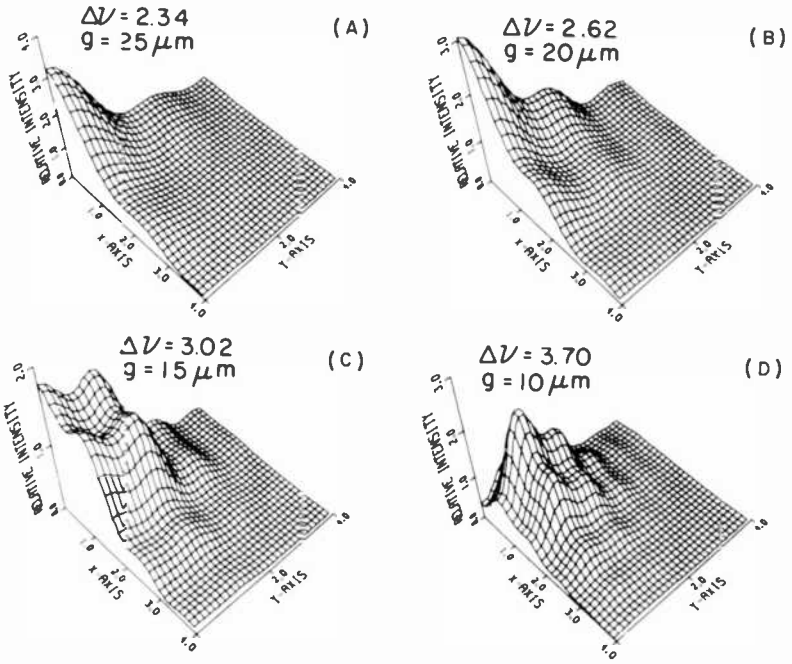

Fig. 2—Aerial images for positive-tone, isolated-square contact hold maskings, 5 × 5 μm aperture, 365 nm wavelength, coherent irradiation: (a) Δv = 2.34, print gap 25 μm; (b) Δv = 2.62, print gap 20 μm; (c) Δv = 3.02, print gap 15 μm; (d) Δv = 3.70, print gap 10 μm.

rule considerations, both figures display various diffraction patterns in terms of 5 × 5 μm apertures. The gap setting is used to vary Δv. Only a quarter of the diffraction pattern under the aperture is computed. The effective wavelength of resist exposure is 365 nm. The coordinates (0, 0) represent the center of the square aperture and (2.5, 2.5) the corner of the square. Regions between the coordinates 0 and 2.5 on both the x and y axes represent a quadrant of the square aperture. Regions on x and y axes between 2.5 and 4.0 are periphery regions under the mask. Fig. 4 shows a schematic of the calculated region of the square mask feature. The same regions are computed for the negative-tone square shadows.

Fig. 3 displays quadrants of diffraction patterns for 7 × 7 and 10 × 10 μm apertures at a 15 μm print gap. For the 7 × 7 μm apertures the coordinates 0.0 to 3.5 are part of the aperture quadrature. The coordinates 3.5 to 4.0 are periphery regions. For the 10 × 10 μm aperture the coordinates 0.0 to 5.0 are part of the aperture quadrature. The coordinates 5.0 to 8.0 are periphery regions.

Several aspects of these computed diffraction patterns are notewor-

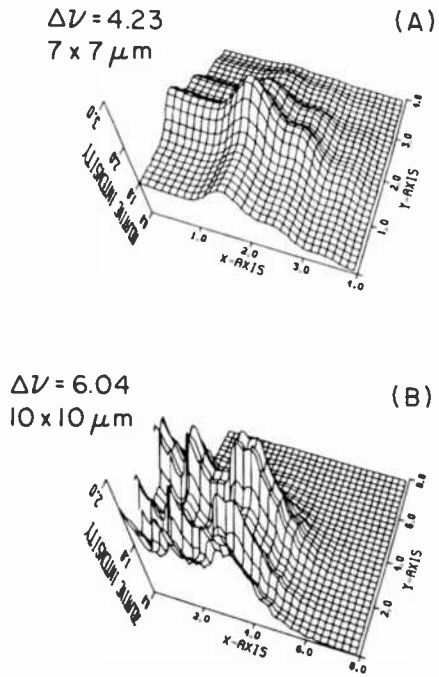

Fig. 3—Aerial images for positive-tone, isolated square contact hole masking, 15-μm print gap, 365 nm wavelength, coherent irradiation: (a) $\Delta\nu$ = 4.32, 7 × 7 μm aperture and (b) $\Delta\nu$ = 6.04, 10 × 10 μm aperture.

thy. Fig. 2 shows that as the $\Delta\nu$ imaging parameter increases (i.e., the print gap decreases), the intensity nodes generally move more toward the edges of the mask opening. Large changes in the appearance of the diffraction pattern are evident even with relatively small changes in the gap setting. There are wide deviations in exposure across the aperture for most patterns. In some cases even regions close to the center of the aperture exhibit marked exposure deviations. Exposure variations on the order of a factor of four are possible within the distance of one micron (Fig. 2d).

Examination of the diffraction pattern can be used to predict the resist image shape. At $\Delta\nu$ values of 2.0 and below, only a single intensity node is in the center of the aperture (Fig. 2a). A circular resist image is the probable result. At $\Delta\nu$ values of 2.5, intensity nodes are also present on the x and y axes (Fig. 2b). Corners of the square aperture are still not exposed. Diamond-shaped resist images result from this diffraction pattern.

At $\Delta\nu$ values in the vicinity of 3.0, both off-axis and off-center intensity nodes are present (Fig. 2c). This diffraction pattern generally produces near-square images from square apertures. However, de-

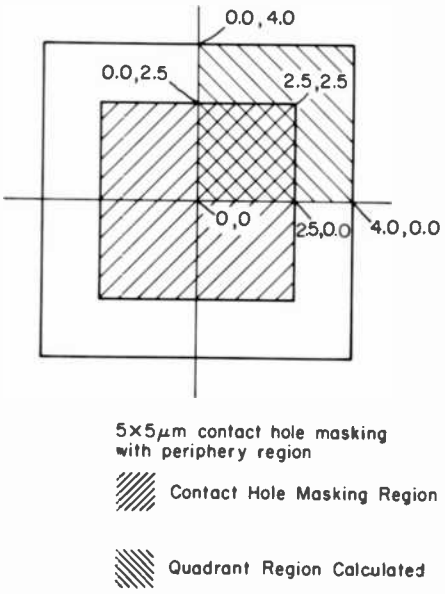

Fig. 4—Aerial Images Calculation Schematic.

pending on the exact intensity of the off-axis intensity node, near-circular resist images can also result at $\Delta\nu$ values slightly less than 3.0. At $\Delta\nu$ values of 3.5, the center node and on-axis node intensity have dropped relative to the off-axis intensity nodes (Fig. 2d). This diffraction pattern produces cloverleaf-shaped resist images.

At still larger $\Delta\nu$ values (Fig. 3) there is always a large intensity node at the corner of the square aperture. A characteristic ballooning at the corner of the resist image results. Table 1 summarizes these imaging results for various $\Delta\nu$ parameters.

Tracking the center node intensity versus the $\Delta\nu$ imaging parameter provides some noteworthy information (Fig. 5). Although the center-node intensity does not determine the image shape in the positive tone, some of the trends of the center node intensity plot mark the points where specific shaped images are formed. The intensity minimum at a $\Delta\nu$ value of 3.7 marks the lack of intensity on the x and y axis or the cloverleaf resist image shape. As the intensity rises to the right of this point, ballooned corners become more prevalent as inten-

Table 1—Parameters for Various Resist Images ($\Delta\nu = d\sqrt{2/\lambda g}$)

$\Delta\nu < 2.0$	Circular resist image
$\Delta\nu \approx 2.5$	Diamond resist image
$\Delta\nu \approx 3.0$	Square resist image
$\Delta\nu \approx 3.5$	Cloverleaf resist image
$\Delta\nu > 4.5$	Square with ballooned corners

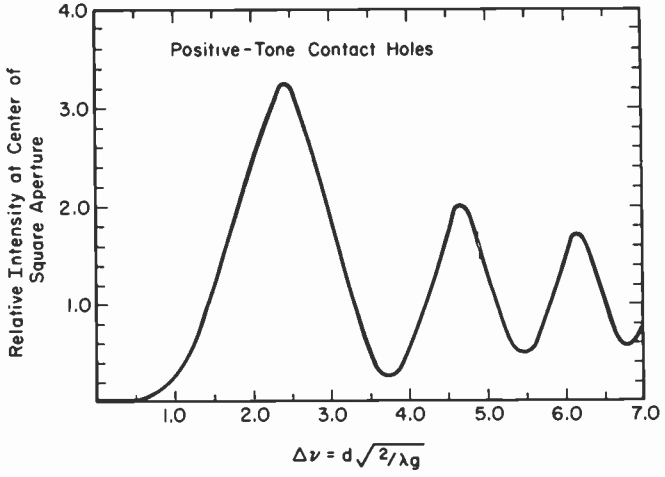

Fig. 5—Center-node intensity for positive-tone maskings.

sity nodes return to the x-y axis. To the left of this point, the intensity of the center-node begins to increase dramatically and the resist image shape undergoes pronounced changes. Accompanying this increase in intensity at the center of the aperture is a reduction and disappearance of intensity nodes off and on the x and y axis. Although intensity of periphery regions of the aperture decreases, overexposure of the center of the aperture occurs simultaneously to a $\Delta\nu$ value of 2.4.

Experimental examples of resist images for all the diffraction patterns at appropriate $\Delta\nu$ imaging setting are presented in Figs. 6 and 7. The major features of the resist image are predicted well from the diffraction pattern. The resist thickness is 1.3 μm. In theory, the gap setting should represent both the resist thickness and the distance between the mask and resist. In practice, however, gap settings usually exceed 15 μm and the resist thickness is generally less than 2 μm. The increase in gap setting, including the resist thickness, is usually within the tolerances of the gap setting unit. This is not the case for contact printing using thick resist films. SEM micrographs of the resist image do show a difference in the image shape from the bottom to the top of the resist layer. If there is no resist deterioration during the etch, the etched image reflects the shape of the bottom portion of resist image. In most cases, the diffferences in image shape from the top to the bottom of the resist are small.

6. Negative-Tone Contact Holes

Diffraction patterns for negative-tone isolated square contact holes (shadows) are displayed in Fig. 8. The same quadrature is computed

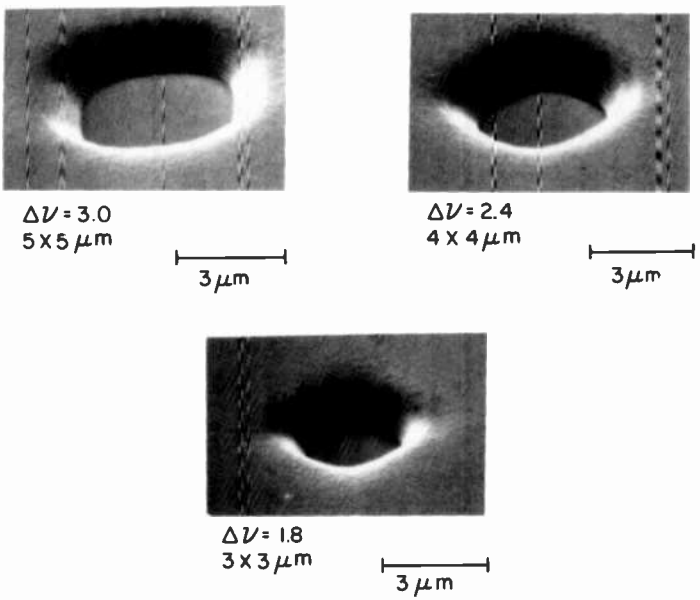

Fig. 6—Positive resist images (HPR 204) for various aperture sizes: SEM micrographs from Canon proximity printer, 15 μm gap.

as in Figs. 2 and 4. The region between the coordinates 0.0 and 2.5 are under the square shadow. Regions between the coordinates 2.5 and 4.0 represent the periphery of the mask feature.

Diffraction pattern features include an intensity node in the center of the shadow, excessive intensity around the outside edge of the shadow boundary, and intensity under the mask at the corners of the shadow. The feature of the diffraction pattern that presents the most serious limitation to opening contact holes in the negative tone is the

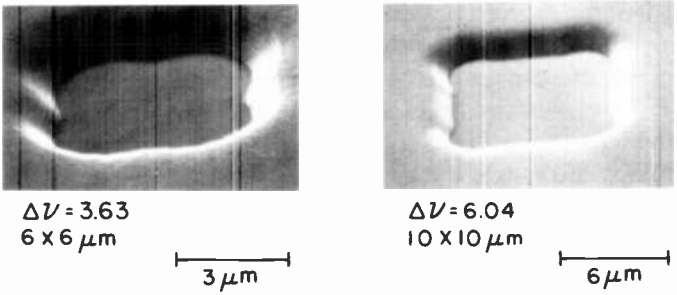

Fig. 7—Positive resist images (HPR 204) for various aperture sizes: SEM micrographs from Canon proximity printer, 15 μm gap.

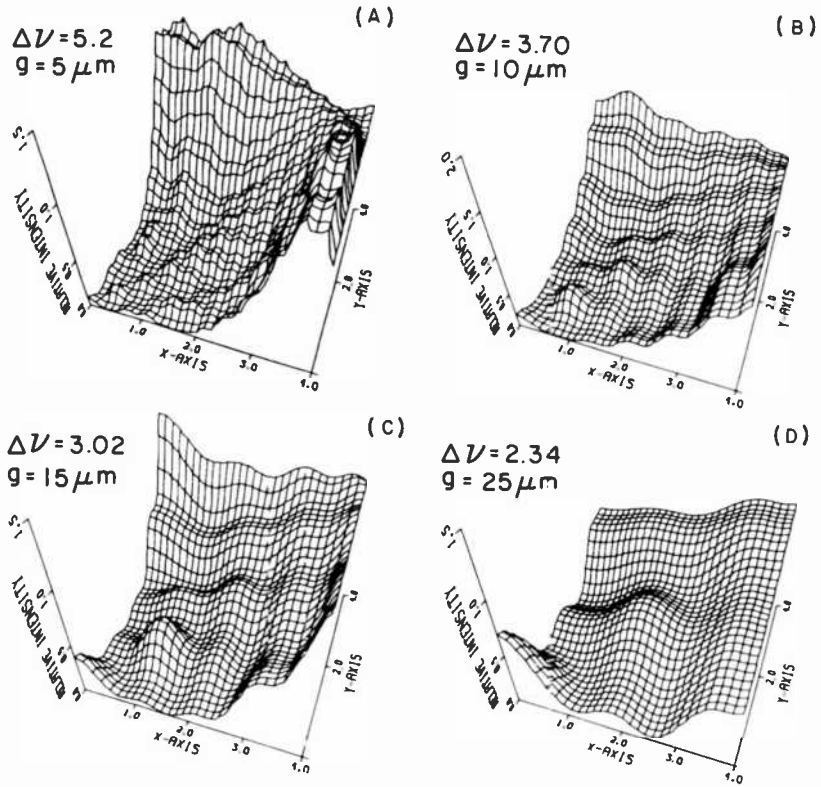

Fig. 8—Aerial images for negative-tone, isolated square contact hole masking: 5 × 5 μm shadow, 365 nm wavelength and coherent irradiation: a. $\Delta\nu$ = 5.23, print gap 5 μm; b. $\Delta\nu$ = 3.70, print gap 10 μm; c. $\Delta\nu$ = 3.02, print gap 15 μm; and d. $\Delta\nu$ = 2.34, print gap 25 μm.

presence of the intensity node in the center of the square shadow. Smoothing effects from resists with wide response ranges and polychromatic light sources are not very effective in removing this limitation, since all the possible diffraction patterns must contribute some intensity to the center of the shadow. The relative intensity of the center-node versus the $\Delta\nu$ of the diffraction pattern is plotted in Fig. 9. Because the curve shows a rapidly rising center-node intensity at a specific $\Delta\nu$ value range, a $\Delta\nu$ imaging setting greater than a particular value can be selected to guarantee reasonable imaging across a wafer.

A $\Delta\nu$ value of around 4.0 was selected as the limiting imaging setting for conventional negative-resists. At $\Delta\nu$ values below 4.0, a rapid rise in the center node's intensity is observed. Although individual contact holes may be opened at $\Delta\nu$ values somewhat below 4.0, the variation in gap settings across a wafer make $\Delta\nu$ values below 4.0 a precarious imaging setting. In some cases, a $\Delta\nu$ imaging setting of 4.0 and above

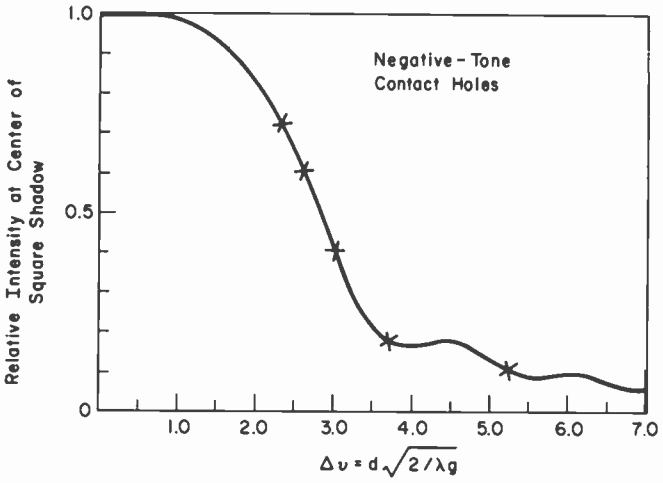

Fig. 9—Center-node intensity for negative-tone maskings.

may not be sufficient for opening contact holes. In many cases contact holes are made in recessed regions on the device. There is increased intensity just outside the shadowed region in all the diffraction patterns presented here. For example, instead of an intensity of 1.0 outside the shadowed regions, intensities in the range of 1.5–2.0 are common. The most significant periphery intensities also occur at Δv values of around 4.0. It is possible that contact holes in recessed regions on the device may not be opened because of excessive reflections in the actinic radiation off the surrounding topology. In the proximity printing mode, these effects are only enhanced by the presence of increased intensity around the periphery of the shadow.

This diffraction-induced intensity deviation is the primary reason that it is often desirable to substantially underexpose the negative resist to obtain best resolution. However, underexposed resists have been known to present adhesion problems during wet-chemical etching. This may not be a major concern for proximity printing, since the periphery region surrounding a masked feature is usually overexposed at normal exposures. For square shadows, the magnitude of the overexposure at the periphery of the shadow is generally 1.3 to 1.5 times that of the unshadowed exposures. Thus, underexposures in the range of 20 to 30% may present no adhesion problems at the edges of a contact hole during wet chemical etching. On the other hand, underexposed regions in the unshadowed expanses may exhibit a more substantial thinning of the resist during development, which could promote pinhole formation.

Another characteristic of these negative-tone diffraction patterns is that regions near the corner under the mask's shadow generally have

more intensity than other regions near the shadow edge. This phenomenona produces rounded-corners for large $\Delta\nu$ imaging settings and diamond-shaped resist images for imaging settings approaching the resolution limits.

Smoothing mechanisms can be of some benefit for opening contact holes that are closed due to excessive periphery exposure. The periphery exposure is characterized by intensity nodes that change position with respect to wavelength. Reflections are also wavelength dependent. Thus, resists with wide response ranges and polychromatic light sources can be used to improve, or at least smooth out, the periphery exposure pattern.

An experimental verification of the computed diffraction patterns is difficult to obtain with conventional negative resists. Negative resists swell during development, and this swelling distorts the final image. Also, in cases where the center node intensity is large, the contact hole is effectively closed and there is little resist image to actually observe. However, positive tone imaging of square shadow maskings do record imprints of intensity nodes under the shadow. Fig. 10 displays resist images of positive tone shadows. The left-hand figure was taken with a high pressure mercury lamp at a $\Delta\nu$ setting of nominally 2.0. The right-hand figure was taken with a polychromatic source at a $\Delta\nu$ setting of nominally 2.4. Both images leave imprints of the center node intensity. The right-hand photo even records imprints of the intensity nodes on the diagonal of the square shadow (Figs. 8c, d).

It appears that the presence of an intensity node in the center of isolated square shadows provides the ultimate imaging limitation in the negative tone. It appears unlikely that with conventional resists contact holes can be imaged uniformly across a wafer with $\Delta\nu$ parameters less than 4.0. In some cases, contact holes in difficult topology cannot be printed at this imaging setting because of the excessive periphery exposure.

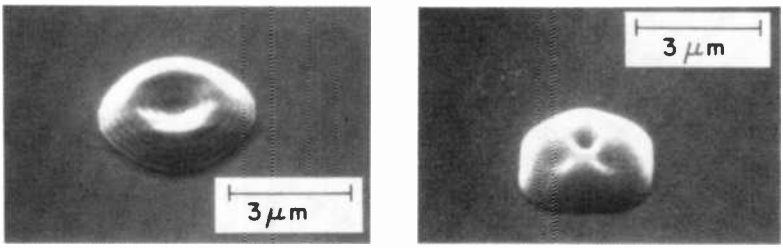

Fig. 10—Positive resist images (HPR 204) for isolated square shadow (3 × 3 μm): left, mercury lamp $\Delta\nu \approx 2.0$ and (right) polychromatic exposure $\Delta\nu \approx 2.4$.

7. Polychromatic Light Sources

Previous discussions showed that polychromatic sources provide advantages for near-contact printing. The total response characteristics of the resist are utilized to improve resist speed. It is apparent (Fig. 1) that conventional mercury light sources do not make use of the total response characteristics of the resist. In addition to the improved resist speed, the multiple wavelength exposure should help smooth out diffraction effects. Resists that exhibit the most marked improvement are those that have a single mercury line to activate their sensitizer. The resolution improvement is expected to be minimal, since the additional wavelengths employed to expose the resist usually are not significantly lower than those employed with conventional mercury lamp exposures.

The most significant advantage of polychromatic sources—absence of standing waves—is beyond the scope of this study, but is mentioned here so as not to belittle its effect. In Fig. 10, there is an absence of standing waves on the sidewalls of the resist image for the polychromatic exposure. For smaller features this improvement appears to produce much sharper, although not necessarily acceptable, resist images. Standing-wave phenomenon[12-15] are wavelength dependent. Polychromatic exposures appear to minimize these effects, and improved resist step coverage should result from such resist exposures. Generally, exposure conditions that minimize image distortion on flat surfaces should also improve step coverage over topology.

8. Flatness Deviations

Flatness deviations across wafers and masks are important to any noncontact photolithographic process. The $\Delta\nu$ imaging parameter provides the means for predicting the effects of resist imaging as a function of wafer flatness (i.e., the variation in the print gap). Fig. 11 shows how the $\Delta\nu$ imaging parameter changes with respect to print gap for various square dimensioned contact holes. Several aspects of printing across nonflat substrates and masks are evident. As mask dimensions shrink, the change in the $\Delta\nu$ imaging parameter at a constant print gap is less. For example, printing 5×5 μm at a 15 μm print gap ($\Delta\nu = 3.0$) produces imaging parameter changes of 2.62 to 3.70, for $\pm$ 5 μm flatness deviations. The 7×7 μm contacts at a 15 μm gap ($\Delta\nu = 4.23$) produces imaging changes of 3.66 to 5.18 for ± 5 μm flatness deviations. However, if the $\Delta\nu$ imaging parameter is set at a constant for any contact-hole dimension, flatness deviations produce smaller $\Delta\nu$ imaging parameter changes for the larger contact holes. For example at a constant $\Delta\nu = 3.0$ setting, the print gap would be set at 15 μm for the 5×5 μm contact

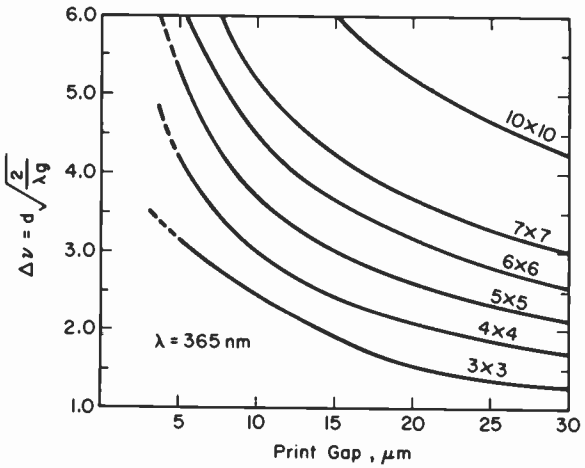

Fig. 11—Print gap versus $\Delta\nu$ imaging setting for various dimensioned contacts.

and at 29.8 μm for the 7 × 7 μm contact. A 5 μm reduction in print gap produces a $\Delta\nu$ imaging parameter of 3.29, while a 5 μm increase yields a $\Delta\nu$ to 2.80 for the 7 × 7 μm contact. In effect, there is no real advantage to reducing contact hole dimensions to lessen flatness sensitivity, because print gaps must also be reduced to produce the same $\Delta\nu$ imaging parameter setting. The X's marked on $\Delta\nu$-versus-center-mode-intensity curve in Fig. 9 show the changes in the $\Delta\nu$ imaging parameter for a 5 × 5 μm contact with 5 μm changes in the print gap.

The effects of flatness deviations on resist images can be analyzed using the $\Delta\nu$ imaging parameter. Our experiments show that the changes in the positive resist image shape do occur with flatness deviations. The near-square resist images produced from a 5 × 5 μm aperture at a 5 μm print gap can change to diamond-shaped resist images with just a 5 μm increase in print gap. A 10 μm increase in print gap produces circular-shaped resist images (see Fig. 2). The resist image shape for appropriately dimensioned contact holes can be used to monitor wafer and mask flatness deviations on a proximity printer.

9. Deep-UV Exposure

Available deep-UV resists contain sensitizers that respond to wavelengths below 300 nm. Their use requires quartz masks and optics. In addition, there is competitive absorption between the sensitizer and resin that contributes to slower speeds, sloped wall profiles, and sometimes an inability to expose thick resist coatings. A major incen-

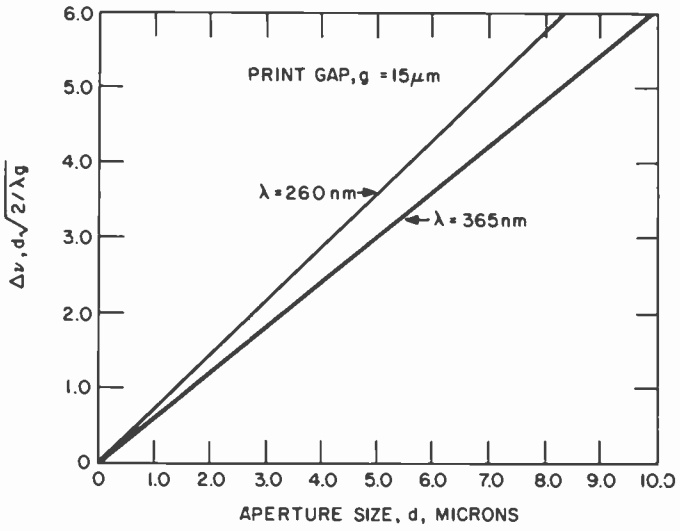

Fig. 12—Deep-UV resolution comparison.

tive for using deep-UV resist is the improved resolution their lower wavelength response provides.[16]

The $\Delta\nu$ imaging parameter can be used to predict the resolution improvement for proximity printing modes. Fig. 12 shows the $\Delta\nu$ imaging parameter versus the dimension of the square mask feature for a relevant deep-UV wavelength (260 nm) and the 365-nm mercury line. The print gap is a constant 15 μm. The increase in resolution is relatively small. Setting the image parameter constant at $\Delta\nu = 3.0$, a 5×5 μm feature is printed at the 365-nm wavelength. At the 260-nm wavelength, a 4.3×4.3 μm feature is printed. The resolution improvement goes as the square root of the wavelength. The sensitivity-to-flatness deviation is also increased by the same square-root function in the $\Delta\nu$ imaging parameter. Although the deep-UV resolution improvement appears marginal, deep-UV resist may have applications on reflective substrates. At the 260-nm wavelength, less reflection of the actinic radiation is expected off aluminum, while increased reflection is expected from silicon layers.

10. Contact Printing with Thick Resist Films

Resist thickness becomes a significant factor for determining the imaging limitations of contact printing. For high resolution (<2 μm) contact printing with thick resist films (>1 μm), diffraction effects become important, particularly if changes in resist thickness over underlying topology are considered. Although conventional contact

printing techniques (i.e., glass mask in contact with wafer) produce too much mask and resist damage to be useful for high resolution VLSI patterns, rather novel contact printing schemes that have no hard glass mask in physical contact with the wafer do show promise. These schemes involve multilevel resist processing.[21-23] Usually a comformable resist mask is formed with projection lithographic techniques on top of a topology planarizing, deep-UV resist layer. Since the patterned material is designed to screen out deep-UV radiation, flood exposure of the deep-UV resist is essentially contact printing with no physical mask contact. Fig. 13 shows a plot of computed $\Delta\nu$ values versus resist thickness for various line or space dimensions. A wavelength of 230 nm, which corresponds to the maximum response of polymethylmethacylate resist material, is employed in computing these curves.

The imaging limitations at particular $\Delta\nu$ values for various tone contact hole maskings should also be operative here, and standing wave phenomena can become more important at these dimensions depending on the exposure and development techniques.[24] Also, the $\Delta\nu$ values change considerably with resist thickness. Dimensional variations over topological features are a probable result for $\Delta\nu$ values below 3.5. At a given $\Delta\nu$ value, contact-printing with thick resist layers should exhibit diffraction-induced imaging distortions similar to those observed for near-contact printing.

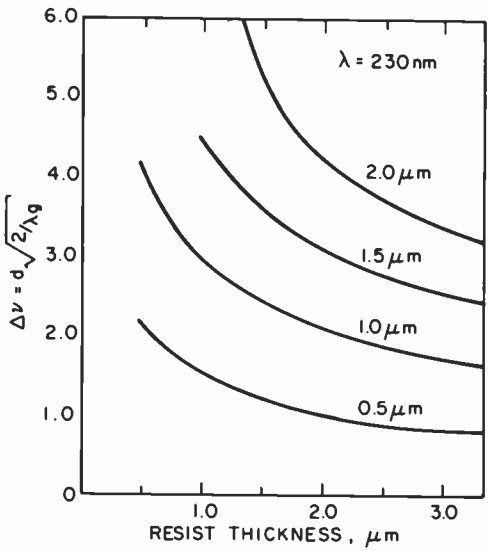

Fig. 13—Imaging parameters for thick resist layers.

11. Coherence Effects

The degree of coherence of the light source is an important aspect of any optical printer. The coherence can affect resolution limits and the degree to which diffraction-induced image distortions are transferred to the resist image. Tradeoffs between reduced resolution and image distortion sometimes have to be made.[12, 17, 18] The computer simulations of the aerial images presented here assume a completely coherent light source. This is nearly, but not precisely, the case for many light sources used on proximity aligners. MTF versus spatial frequency curves for various proximity printers all show near-constant spatial frequency behaviors characteristic of coherent light sources.[12, 19] MTF evaluations of relatively new proximity machines do not exhibit as steep an MTF-versus-spatial-frequency curve, but the curve does exhibit near-constant spatial frequency characteristics.[20] Some slight degree of incoherence is conceivably introduced by the optics of the fly's-eye lens. This slight partial coherence does affect the computed aerial images to some degree. Previous work[12, 17] comparing coherence and incoherent irradiation at straight edge maskings show that the position of the diffraction induced intensity nodes remain relatively constant. The valleys between intensity nodes, however, tend to be less precipitous, essentially smoothing the diffraction pattern. Increased incoherence does help smooth diffraction induced defects; however, resist wall profile and resolution suffer.

The coherence level should not affect the resist image shapes substantially, because the position of intensity nodes at the periphery of the positive-tone contact hole images determines the image shape, and only slight changes in intensity node positions are expected with small changes in the coherence level. For negative-tone contact holes, the intensity smoothing between intensity nodes at increased incoherence levels may provide improved imaging. The effect of the periphery exposure is reduced and the center node intensity does not play as prominent a role in the resist image formation. In both cases, however, the resist wall profile is expected to deteriorate to some degree with increased incoherence. The coherence of the light source provides another parameter to adjust for resolution and distortion effects. The optimum coherence level, however, depends on the resist response characteristics and the imaging requirements of the IC pattern.

12. Summary

Fresnel approximation and Babinet's principle have been used to compute the aerial images for contact hole maskings in both the positive and negative tone. A single imaging parameter, Δr, is sufficient

to characterize the aerial image or, if desired, the resist exposure pattern for various square mask dimensions d, gap settings g, and actinic wavelengths of exposure λ. The $\Delta\nu$ parameter equals $d\sqrt{2/\lambda g}$. Positive-tone contact hole images are characterized by variable image shapes due to changes in the periphery of the diffraction pattern. At $\Delta\nu$ parameters greater than 3.5, cloverleaf-shaped resist images and ballooning at contact holes corners are observed. A $\Delta\nu$ parameter of around 3.0 produces nearly square images from square apertures. Diamond-shaped images are produced from a 2.5 imaging setting. At $\Delta\nu$ imaging parameters below 2.0, circular resist images are produced. Since wafer flatness deviations contribute to variable print gaps, an imaging setting equal to 3.0 or greater is recommended for reliable imaging in the positive tone.

Diffraction-induced image distortions generally are more severe in the negative tone. Intensity nodes at the periphery of the shadow can exceed the intensity of the unshadowed expanses by 50%. This diffraction-induced image distortion can effectively closeup contact hole maskings in recessed regions on devices. The effects of reflections off surrounding topology are enhanced, and printing on reflective substrates made more difficult. Polychromatic light sources and resists with wider response ranges can smooth the effects of the periphery exposure. Another diffraction-induced imaging distortion, however, produces the ultimate imaging limitation. A diffraction-induced intensity node is present in the center of the shadow. At $\Delta\nu$ imaging parameters greater than 4.0, the intensity of this center node is less than 0.2 the intensity of the unshadowed expanses. Below $\Delta\nu$ imaging settings of 4.0, the intensity of this node increases rapidly. Because of the rapid rise in the center node intensity, contact hole imaging with conventional negative resists at $\Delta\nu$ imaging settings below 4.0 cannot be done effectively across nonflat substrates.

The $\Delta\nu$ imaging parameter can also be used to predict the resolution improvement possible with deep-UV exposures. Effects of flatness deviations on the imaging can also be analysed. Polychromatic light sources, resists with wide response ranges, and the degree of coherence can help smooth some of the diffraction-induced image distortions. However, the basic limitations presented here with the $\Delta\nu$ imaging parameter are still applicable to resists with conventional image formation properties.

References:

[1] K. G. Clark and K. Okusu, *Solid State Technology*, **19**, p. 79 (1976).

[2] Canon Proximity Mask Aligner PLA 520F/FA with Deep-UV Illumination, Canon, USA, Inc. (1978).

[3] T. Kaneko, T. Usnegaki, and Y. Kamakami, "A Practical Approach to Sub-micron Photolithography," *Proc. Kodak Interface '80*, (1980).

[4] Philip A. Hunt Chemical Corp., "Waycoat HPR Positive Resist Systems Processing Procedures," Technical Bulletin No. 48-1.
[5] *IMSL Library Reference Manual*, Vol. 1, A-E Ed. 8, June 1980.
[6] A. W. Jessup, private communication.
[7] Born and Wolf, *Principles of Optics*, Pergamon Press, 3rd Ed., New York (1965).
[8] J. M. Stone, *Radiation and Optics*, McGraw-Hill, New York (1963).
[9] B. Rossi, *Optics*, Addison-Wesley, Mass. (1957).
[10] J. G. Skinner, *Proc. Kodak Interface '73*, G-35, p. 53 (1974)
[11] D. Widmann and K. U. Stein, "Semiconductor Technologies with Reduced Dimensions," Solid State Circuits, *Proc. 2nd Eur. Solid State Circuits Conf, 1976*, 29 (Pub. 1977).
[12] J. D. Cuthbert, *Solid State Technology*, **20**, p. 59 (1977).
[13] F. H. Dill, *IEEE Trans. Electron Devices*, **22**, p. 440 (1975).
[14] F. H. Dill, A. R. Neurether, J. A. Tuttle, and E. J. Walker, *IEEE Trans. Electron Devices*, **22**, p. 456 (1975).
[15] E. J. Walker, *IEEE Trans. Elec. Devices*, **22**, p. 464 (1975).
[16] B. J. Lin, *J. Vac. Sci. Technol.*, **12**, p. 1317 (1975).
[17] M. M. O'Toole and A. R. Neurether, "Influence of Partial Coherence on Projection Printing," *SPIE Developments in Semiconductor Microlithography IV*, **179**, p. 22 (1979).
[18] M. J. Bowden, *J. Electrochem. Soc.*, **128** (5), p. 195C (1980).
[19] M. C. King and M. R. Goldricks, *Solid State Technology*, **21**(2), p. 37 (1977).
[20] L. K. White, unpublished results.
[21] B. F. Griffing, P. D. Johnson, and J. F. Norton, *Proc. of SPIE*, **175**, p. 136, (1981).
[22] T. Batchelder and Clifford Takemoto, *Semiconductor International*, p. 213–220, (1981).
[23] B. J. Lin and T. H. P. Chiang, *J. Vac. Sci. Tech.*, **16** (6), p. 1669 (1979).
[24] T. LaRue and C. Ting, *Proc. of SPIE*, **175**, p. 17 (1981).

AUTHORS

Robert Amantea received the BSEE degree from the City University of New York in 1965 and the MS degree from the Polytechnic Institute of New York in 1969. He was a David Sarnoff Fellow at the University of California at Berkeley, where he received the PhD in 1977. Dr. Amantea joined RCA Laboratories, Princeton, NJ, in 1965 and has since worked in the area of power semiconductor devices. He has authored several papers on such topics as power transistors, TRAPATT devices, gated-diode physics, and gate-turn-off thyristors. He holds several U.S. patents. Recently, his interests have been in the area of automated fault isolation, artificial intelligence, and computer-aided design.

Dr. Amantea is a member of IEEE, Eta Kappa Nu, and Tau Beta Pi.

Daniel W. Bechtle received a BA (Honors) in Physics from the University of Oregon in 1971 and a PhD degree in Physics in 1977 from the University of Colorado. As part of his graduate work, he designed and built an automatically stabilized scanning Fabry-Perot interferometer. His PhD dissertation was concerned with experimental laser-light scattering in a transparent semiconductor. While at the University of Colorado he also consulted for Burleigh Instruments. He has designed one of two electronic instruments that received an IR-100 award from *Industrial Research* magazine in 1976. In 1978 he joined RCA Laboratories at Princeton, NJ, as a Member of Technical Staff. There he has developed analog and digital fiber-optic communication systems for studio video applications, and is currently developing a 1-GHz optical delay line.

Dr. Bechtle is a member of Phi Beta Kappa.

Erwin F. Belohoubek received a Diplom-Ingenieur degree in 1953 and a PhD in Electrical Engineering in 1955 from the Technical University in Vienna, Austria. He joined RCA in 1956 as a Member of the Technical Staff and currently is Head of Microwave Integrated Circuits at the Microwave Technology Center of RCA's David Sarnoff Research Center in Princeton. In this capacity, he is responsible for the development of active and passive microwave integrated circuits, including transistor amplifiers, multipliers, active microwave filters, various solid state radars and other microwave subsystems.

Dr. Belohoubek holds 8 patents and has authored more than 30 technical papers in the areas of traveling-wave tubes, microwave measurements and microwave integrated circuits. He is a Fellow of the IEEE.

Richard Brown received his B.S. in Chemistry from Wagner College in 1951. After returning from the USAF in 1956, he attended Seton Hall University, taking the Master's Program in Chemistry. He joined the Bell Telephone Laboratories in 1959 where he worked on thin-film substrate interactions and analytical techniques for thin-film chemical analysis. He continued this work after joining RCA in 1971. Between 1971 and 1979 Mr. Brown worked on all phases of the air insulated crossover hybrid substrate for the Trident Program. Since 1979 he has been at RCA Laboratories working on developing new technologies for microwave hybrids. In his present position he is responsible for the fabrication of thin-film hybrids. This includes the mask manufacture, vapor deposition, photolithography and electroplating.

Mr. Brown is a member of the Electrochemical Society, American Ceramic Society, International Society for Hybrid Microelectronics (ISHM), and American Vacuum Society.

Robert B. Comizzoli received a BS degree in Physics, summa cum laude, from Boston College in 1962 and was awarded Wilson, Danforth, and National Science Foundation Fellowships. He attended Princeton University from 1962 to 1966, receiving a PhD in Physics in 1967. His thesis work involved polarization effects in photoconductors. He joined RCA Laboratories, Princeton, NJ, in 1966. His research experience includes color centers in alkali halides, atomic beams, neutron interactions with polarized nuclei, photoconductivity, electrophotography, silicon device surface effects, and dielectric breakdown evaluations. Dr. Comizzoli has studied the glass passivation of silicon devices and has developed novel methods for the deposition of thick-glass passivating films. He originated a useful method for decorating localized defects in insulating films over conductors or semiconductors. He has also studied failure mechanisms of bipolar and CMOS integrated circuits, and has made important contributions to understanding and eliminating these failure mechanisms. In November 1979 Dr. Comizzoli was appointed Manager, Quality Assurance and Special Projects, at the Solid State Technology Center of RCA Laboratories in Somerville, NJ, with responsibility for the quality and reliability of custom LSI devices.

Dr. Comizzoli is author or coauthor of 25 technical papers and has five issued patents. He received a 1973 RCA Laboratories Achievement Award for his team contributions to the glass passivation of silicon device structures, and a 1978 RCA Laboratories Achievement Award for team contributions to integrated circuit reliability. He is a Senior Member of IEEE and a member of the Electrochemical Society, and serves as Symposium Chairman of the Dielectric and Insulation Division of the Electrochemical Society. In March 1981, Dr. Comizzoli left RCA.

David A. de Wolf received the B.Sc. in 1955 and the M.Sc. in 1959 from the University of Amsterdam, both degrees in physics. He obtained a Ph.D. in Electrical Engineering from the Technological University of Eindhoven in 1968. He has been at RCA Laboratories since 1962 where he has worked in plasma physics, wave propagation in the atmosphere, reentry physics, radiation from antennas, communications in planetary atmospheres, diffraction optics, liquid-crystal properties, and electron optics of display devices. He is one of the early contributors to the understanding of multiplescattering effects of high-frequency waves propagating through random media such as turbulent air. He is a member of the U.S. national Committees B and F of the International Union of Radio Science (U.R.S.L.), and served as Associate Editor of the Journal of the Optical Society of America from 1969 to 1981.

Henry Johnson attended Johns Hopkins University and received the BS Degree from Drexel University. He joined the RCA Electron Tube Division in Harrison, NJ in 1956 working on pencil tube design. In 1959, he transferred to the Microwave Technology Center at the RCA Laboratories in Princeton, NJ, where he has made significant contributions in the fields of optical communications and microwave transistor and bulk device circuitry. He has successfully completed programs involved with the development of microwave sources, FET phase shifters, and radar transponder systems. More recent responsibilities include the design of a microwave synthesizer, an active antenna array, and the development of pulse-compression and FM-CW radars. He was the recipient of RCA Laboratories Achievement Awards in both 1978 and 1979.

Mr. Johnson holds 10 patents and has contributed more than 30 papers to technical journals or conferences.

Werner Kern received his education in chemistry in schools in Switzerland and the U.S.A. The research thesis he published in 1947, on the discovery of fluorescing carcinogenic hydrocarbons in soil, established an important new branch of environmental science. He was a research chemist with Hoffmann-La Roche in Switzerland and New Jersey, and later with Nuclear Corporation of America; there he became chief chemist directing research in radiation chemistry. In 1959 Mr. Kern joined RCA Electronic Components and Devices Division to investigate semiconductor processes by radiochemical methods, was project scientist and consultant on several research projects, and was in charge of radiological safety. Since 1964 he has been at RCA Laboratories, Princeton, N.J. as a Member of Technical Staff. He has been working in semiconductor process research, specializing in the characterization and device applications

of dielectric films, chemical vapor deposition, and etching processes. From 1974 to 1979 he was project scientist for government-sponsored research contracts on glass passivation, dielectric defects, and silicon solar cells.

Mr. Kern is Vice Chairman of the Dielectric and Insulation Division of the Electrochemical Society, is a member of the American Chemical Society, the American Vacuum Society, the Electrochemical Society, and the Research Honorary Society of Sigma Xi, and is listed in *American Men and Women of Science* and *Who's Who in the East*. He is the author or coauthor of over 60 scientific publications, holds five U.S. patents, has presented numerous invited technical lectures, and has organized scientific symposia. He received an RCA Achievement Award in 1966 for his work in integrated-circuit process research, and is the recipient of the Callinen Award for 1971 of the Electrochemical Society, in recognition of his pioneering research in chemical vapor deposition. Mr. Kern received a 1973 RCA Laboratories Outstanding Achievement Award for his team contributions to the glass passivation of silicon device structures. He also coedited and coauthored a book, *Thin Film Processes*, published by Academic Press in 1978.

Edward Mykietyn joined the RCA Microwave Tube Engineering Section at Harrison, NJ in 1950 where he was involved in the construction of magnetron tubes. He became Foreman of the Microwave Tube Assembly group in 1953 and was responsible for the assembly, mounting, processing, and finishing of microwave tubes. From 1960 to 1964 as a Specialist, Microwave Manufacturing, he was responsible for the construction of special-purpose traveling-wave tubes including assembly techniques on highly reliable metal-ceramic traveling-wave tubes for military satellite applications. In 1965, Mr. Mykietyn joined the Microwave Technology Center, Princeton, NJ as a Technical Staff Associate and was responsible for the assembly and processing of microwave cross-field delay tubes, solid state power sources, linear power amplifiers, transistor chip carriers, GaAs FET amplifiers, and bonding techniques. In his present position, Mr. Mykietyn is responsible for running a high technology assembly area providing technical skills in the building of sophisticated microwave components and amplifiers.

Mr. Mykietyn is the holder of five U. S. patents.

Moshe Oz received his B. S. Degree from Ben-Gurion University, Beer-Sheva, Israel in 1971. He then joined Armament Development Authority, Haifa, Israel. As a research engineer he was involved in the development of microwave antennas, filters, amplifiers and sources. In 1978 he became head of the transmitting and receiving group working on large rf communications systems. He is now on a one-year sabbatical with RCA and is involved with the development of an amplifier for an active antenna array and filters for communications systems.

George L. Schnable received a B.S. degree in Chemistry from Albright College, Reading, Pa., in 1950, and M.S. and Ph.D. degrees in Chemistry from the University of Pennsylvania, in 1951 and 1953, respectively. From 1953 until 1971, he was employed by Philco-Ford Corporation, where he became Manager of the Advanced Materials and Processes Department in the R & D Operation of the Microelectronics Division. In 1971, Dr. Schnable joined RCA Laboratories, Princeton, N.J., as Head, Process Research, in the Process and Applied Materials Research Laboratory, where he supervised projects dealing with thin-film dielectrics and metallization, silicon device fabrication technology, ion-implantation technology, and silicon device reliability. In 1977, he was named Head, Solid State Process Research. He is presently Head, Device Physics and Reliability in the Integrated Circuit Technology Laboratory of RCA Laboratories.

Dr. Schnable holds over 20 U.S. Patents and is listed in American Men and Women of Science. He is a Member of the American Chemical Society, the Electrochemical Society, the Franklin Institute, the Pennsylvania Academy of Science, Alpha Chi Sigma, Phi Lambda Upsilon, and Sigma Xi; a Senior Member of the American Association for the Advancement of Science and the Institute of Electrical and Electronics Engineers; and a Fellow in the American Institute of Chemists.

Franco N. Sechi received the degree of Doctor in Electrical Engineering in 1964 from the Polytechnic Institute of Milano, Italy. From 1965 to 1968 he was employed by ITT in Milano, where he was concerned with the design of solid-state microwave radio-link equipment. In 1968, he joined RCA, Electronic Components, as a design engineer in the Solid State Product Design Group. In this position he designed transferred-electron oscillators and developed a technique for measuring the impedance of transferred-electron diodes under large-signal conditions. In 1973, he transferred to the Microwave Technology Center, RCA Laboratories, Princeton, NJ. In his present position he is involved in the development of power transistor amplifiers. For his work on linear microwave power amplifiers, he received an RCA Laboratories Outstanding Achievement Award in 1976. He received a second Achievement Award in 1979 for his work on a solid-state radar system for aircraft.

Dr. Sechi has authored papers on transferred-electron oscillators, the thermal and large-signal characterization of microwave devices, and high-power microwave transistor amplifiers. He currently holds six U.S. patents. Dr. Sechi is a member of the IEEE.

Steve Siegel received his BSEE summa cum laude in 1974 from the Polytechnic Institute of New York. He has done graduate work at the University of Pennsylvania and is currently completing his MSEE degree at Rutgers University. Mr. Siegel joined RCA Laboratories in 1979 and has been involved in the design and development of both analog and digital fiber-optic communication systems. He has designed fiber-optic transmitter and receiver modules for both high-speed digital systems and video frequency analog links. His work has included fiber coupling and lensing techniques.

He is a member of Sigma Xi and Eta Kappa Nu.

Lawrence K. White received an A.B. degree from Earlham College (1970) and a Ph.D. degree in physical chemistry (1975) from the University of Illinois (Urbana). He joined RCA Labs in 1978 where he became involved in IC device processing and reliability research. He is now engaged in studies of patterning technologies for ULSI circuits. Dr. White is a member of Phi Lambda Upsilon, Sigma Xi, Alpha Chi Sigma, the American Chemical Society, and the Electrochemical Society.

Patents Issued to RCA Inventors–First Quarter 1982

January

R. A. Bartolini, W. J. Burke, and A. Bloom Method of Recording an Ablative Optical Recording Medium (4,313,188)
H. W. Bilsky and P. J. Callen Battery Charging System (4,313,078)
S. Bloom and C. A. Catanese CRT With Dipolar Deflection and Quadrupolar-Focusing Color-Selection Structure (4,311,944)
D. F. Bowman Transmission Line Hybrid Junction (4,310,814)
L. A. Boyer Magnetic Variable Capacitor (4,312,025)
R. E. Cardinal Coaxially Mounted High Frequency Light Detector Housing (4,309,717)
T. J. Christopher Error Coding for Video Disc System (4,309,721)
R. D. Faulkner and R. E. McHose Alkali Antimonide Layer on a Beryllium-Copper Primary Dynode (4,311,939)
W. H. Groeneweg Signal Processor for Beam-Scan Velocity Modulation (4,309,725)
W. Hinn Dual Standard PAL-SECAM Receiver Circuitry (4,309,719)
S. T. Hsu Method of Manufacturing Submicron Channel Transistors (4,312,680)
S. T. Hsu Electrically Programmable Logic Array (4,313,106)
G. John Dual Parallelogram Cutterhead Suspension Apparatus (4,310,915)
F. B. Lang, J. J. Gibson, and M. D. Ross Non-Linear Aperture Correction Circuit (4,312,013)
B. E. Lock Method and Apparatus for Coating Recorded Discs With a Lubricant (4,309,456)
W. G. McGuffin Stylus Position Sensor for Video Disc Player Apparatus (4,313,189)
M. E. Miller Stylus Tracking Aid Using Two Bimorph Elements Longitudinally Aligned (4,310,913)
R. C. Palmer Video Disc Player Noise Reduction Circuit (4,309,722)
J. J. Prusak Cathode Mask Knob (4,309,265)
G. H. Riddle Skipper-Assisted Active Search (4,310,914)
J. C. Rustman and M. J. Mindel Track Error Correction System as for Video Disc Player (4,313,134)
O. H. Schade, Jr. Compensation for Transistor Output Resistance (4,311,967)
P. Sheng Optimal Polarization for the Optical Readout of High Density Video Recording (4,310,910)
F. Sterzer and R. W. Paglione Nonsymmetrical Bulb Applicator for Hyperthermic Treatment of the Body (4,311,154)
J. A. Wilber and T. J. Christopher Bidirectional Deflector Driver for Video Disc (4,313,062)
T. D. Yost Keying Signal Generator With False Output Immunity (4,313,130)

February

R. A. Altenschulte A.C. Power Line Assembly (4,317,152)
J. G. Amery Chrominance Transcoder (4,314,273)
C. H. Anderson, T. L. Credelle, and W. W. Siekanowicz Guided Beam Display Device (4,316,118)
O. Ben-Dov Duopyramid Circularly Polarized Broadcast Antenna (4,317,122)
C. W. Benyon, Jr. and J. J. O'Neill, Jr. Method of Reducing Edge Current Leakage in N Channel Silicon-on-Sapphire Devices (4,313,809)
O. H. Bismarck Fast Level Shift Circuits (4,314,166)
A. Bloom, R. A. Bartolini, A. E. Bell, and S. S. Seffren Thick Protective Overcoat Layer for Optical Video Disc (4,315,269)
W. M. Boyd Bias Adjustment Responsive to Signal Power (4,317,083)
C. B. Carroll Baseplate Assembly for Flat Panel Display Devices (4,316,117)
R. M. Castle Speed Deviation Detector for Servo Controlled Disc Mastering Turntable (4,316,143)
R. M. Castle Head Suspension Velocity Control Apparatus for Electromechanical Recorder (4,317,192)
R. M. Christensen Sound Field Transmission System Surrounding a Listener (4,316,058)
J. C. Cooper Tilted Unitary Degaussing Coil Arrangement (4,316,119)
F. C. Farmer, Jr. RF Generator Monitor Circuit (4,317,223)
R. E. Fernsler and D. H. Willis Two-loop Horizontal AFPC System (4,317,133)

W. G. Gibson and T. M. Wagner Non-Linear Aperture Correction Circuit Having a Signal Bypass Arrangement (4,315,277)
D. Hampel and K. J. Prost Data Classifier (4,316,177)
J. J. Hanak High Voltage Series Connected Tandem Junction Solar Battery (4,316,049)
R. H. Hedel Method for the Manufacture of Capacitive Pickup Styli (4,315,358)
J. G. N. Henderson and C. M. Wine Channel Identification Apparatus Useful in a Sweep Type Tuning System (4,317,225)
P. Ho Redundant Microwave Switching Matrix (4,316,159)
E. F. Hockings and C. A. Catanese Color Television Picture Tube With Color-Selection Structure and Method of Operation Thereof (4,316,126)
S. T. Hsu Multi-Mode Circuit (4,317,110)
R. H. Hughes Color Picture Tube Having an Improved Electron Gun With Expanded Lenses (4,317,065)
S. T. Jolly and J. P. Paczkowski Vapor Phase Deposition Apparatus (4,316,430)
N. A. Macina Multichannel Frequency Translation of Sampled Waveforms by Decimation and Interpolation (4,316,282)
D. Mackey and E. D. Fox Color Kinescope Convergence Measuring System (4,316,211)
A. Miller Array Positioning System (4,314,546)
M. W. Muterspaugh and G. E. Theriault IF Bandpass Shaping Circuits (4,316,220)
E. J. Nossen On Line Quality Monitoring (4,317,206)
D. H. Pritchard and A. C. Schroeder Input-Weighted Transversal Filter TV Ghost Eliminator (4,314,277)
J. J. Prusak Spacer for Stacked Recorded Discs (4,316,281)
W. E. Rodda Method for Adjusting the Bias of a Kinescope in a Color Television Receiver and Apparatus to Facilitate Same (4,316,212)
M. R. Royce and D. D. Shaffer Method for Preparing Copper-Aluminum-Gold-Activated Zinc-Sulfide Phosphors (4,316,816)
J. P. Russell, A. H. Firester, and I. Gorog Optical Recording in Thin Photoresist (4,316,279)
P. M. Russo Priority Vectored Interrupt Having Means to Supply Branch Address Directly (4,315,314)
S. Shiratsuchi Television Receiver Focus Voltage Circuit (4,316,128)
G. A. Simmons and K. W. McGlashan Self-Converging Deflection Yoke and Winding Method and Apparatus Therefor (4,316,166)
T. R. Smith and F. J. Marlowe Synchronizing Circuit Adaptable for Various TV Standards (4,316,219)
J. C. Sokoloski Method of Manufacturing Submicron Channel Transistors (4,313,782)
E. F. Steigmeier and K. Knop Defect Detection System (4,314,763)
M. L. Tarng Method of Making Semiconductor Device With Passivated Rectifying Junctions Having Hydrogenated Amorphous Regions (4,315,782)
L. A. Torrington Video Disc Caddy (4,316,539)
H. R. Warren Stop and Variable-Speed Motion on Segmented-Scan Tape Recording (4,317,140)
J. H. Wharton Video Signal Processing Apparatus (4,316,210)
J. H. Wharton and J. E. James Video Processor Employing Variable Amplitude Compression of the Chrominance Component (4,316,213)
C. F. Wheatley, Jr. Method of Fabricating a Schottky Barrier Contact (4,313,971)
M. L. Whitehurst Method for the Manufacture of Recording Substrates for Capacitance Electronic Discs (4,316,778)
C. M. Wine User Control Arrangement for Controlling a Plurality of Functions (4,317,050)
T. D. Yost Keying Signal Generator With Input Control for False Output Immunity (4,316,214)

March

A. Acampora Color TV Buried Subcarrier System (4,318,120)
A. Acampora Synchronizing Transmissions From Two Earth Stations to Satellite (4,320,503)
J. H. Atherton and W. C. Dreisbach Level Shift Circuit (4,321,491)
R. E. Cardinal Apparatus for Resistance Welding of an Electro-Optic Device Housing (4,322,599)
D. E. Carlson Semiconductor Device Having a Body of Amorphous Silicon and Method of Making the Same (4,317,844)
H. Chen Electron Gun With Deflection-Synchronized Astigmatic Screen Grid Means (4,319,163)

R. S. Crandall Method for Measuring the Drift Mobility in Doped Semiconductors (4,319,187)
R. S. Crandall and A. Bloom Reversible Optical Storage Medium and a Method for Recording Information Therein (4,320,489)
R. J. D'Amato Method of Making a Grid for a Cathode-Ray Tube Electron Gun (4,318,026)
R. A. Dischert, E. M. Nagle, and J. J. Williams, Jr. Technique for Optimally Encoding Digitally Encoded Video Signals (4,320,416)
R. A. Dischert and J. M. Walter Rapid Synchronization of Information on Separate Recorded Mediums (4,322,747)
W. V. Fitzgerald, Jr. Side Pincushion Correction Circuit (4,318,035)
W. G. Gibson and F. C. Liu AFT Circuit (4,321,624)
J. Guarracini and V. Ruggeri Video Disc Stylus Control Apparatus (4,320,487)
L. A. Harwood and E. J. Wittmann Symmetrically Gain Controlled Differential Amplifier (4,318,051)
R. J. Hollingsworth Two Input Sense Circuit (4,321,492)
S. T. Hsu Extended Drain Self-Aligned Silicon Gate MOSFET (4,318,216)
L. M. Hughes Carriage Reset Apparatus for Disc Record Player (4,321,702)
R. H. Hughes and H. Chen High Potential, Low Magnification Electron Gun (4,318,027)
L. A. Kaplan Over-Current Protection Circuits for Power Transistors (4,321,648)
M. Kaplan, D. Meyerhofer, and E. S. Poliniak Electron Flood Exposure Apparatus (4,321,470)
H. G. Kiess and B. K. Binggeli Repetitive Readout of Electrostatically Stored Information (4,319,284)
R. W. Kipp Frequency-Tracking Filter, as for Use in FM-CW Radar (4,321,602)
P. R. Knight Television Receiver High Voltage Protection Circuit (4,321,513)
K. Knop Solid-State, Color-Encoding Television Camera (4,318,123)
J. E, Krupa, P. L. Magness, and T. J. Brady Symmetrical Waveform Signal Generator Having Coherent Frequency Shift Capability (4,318,045)
M. E. Malchow Circuitry for Generating Electric Signals With Proportional, Opposite-Sense Rates of Change (4,322,691)
J. G. Martin Susceptor for Heating Semiconductor Substrates (4,322,592)
D. D. Mawhinney Doppler Signal Processing Apparatus (4,319,245)
A. Mayer Wettable Carrier in Gas Drying System for Wafers (4,318,749)
J. E. Nicholson and P. C. Wilmarth Institutional Audio-Visual System Including a Plural Operating Mode Television Receiver (4,319,277)
E. J. Nossen Television Signal With Encoded Synchronizing Signals (4,319,273)
S. T. Opresko Step Mask for Substrate Sputtering (4,322,277)
J. I. Pankove and C. P. Wu Method of Making Selective Crystalline Silicon Regions Containing Entrapped Hydrogen by Laser Treatment (4,322,253)
D. R. Preslar Digital Phase Comparator With Improved Sensitivity for Small Phase Differences (4,322,643)
G. H. Riddle and B. K. Taylor Video Disc Cartridge Having a Self Retaining Electrode (4,320,490)
J. C. Rustman Apparatus for Video Disc Stylus Electrode Reconditioning (4,320,491)
O. H. Schade, Jr. Level Shift Circuit (4,318,015)
G. K. Sendelweck Latch-up Prevention Circuit for Power Output Devices Using Inductive Loads (4,322,770)
T. E. Smith Video Disc Molding Process (4,318,877)
L. N. Thibodeau, D. W. Luz, and J. E. Hicks Commutated SCR Regulator for a Horizontal Deflection Circuit (4,321,514)
C. C. Turner Carrier for Rotatably Holding Kinescope Faceplate During Processing (4,317,427)
J. W. Tuska Three-Condition Display System (4,321,543)
P. V. Valembois, C. A. Deckert, and E. J. Holub Optical Inspection Method for Determining Machinability (4,320,567)
F. S. Wendt High Frequency Ferroresonant Power Supply for a Deflection and High Voltage Circuit (4,319,167)
L. K. White and C. P. Wu Method of Forming Polycrystalline Silicon Lines and Vias on a Silicon Substrate (4,319,954)
D. H. Willis Linearity Corrected Deflection Circuit (4,321,511)
R. E. Wilson Switch Closure Sensing Circuit (4,318,087)
W. R. Witte Power Transformer With High Coupling Coefficient (4,320,373)
R. E. Wolf Radio Transmitter Energy Recovery System (4,319,359)
D. H. Ziegel Levelable Lapping Machine (4,321,772)